



UPPSALA
UNIVERSITET

*Digital Comprehensive Summaries of Uppsala Dissertations
from the Faculty of Science and Technology 1247*

Theory and Modelling of Functional Materials

VANCHO KOCEVSKI



ACTA
UNIVERSITATIS
UPSALIENSIS
UPPSALA
2015

ISSN 1651-6214
ISBN 978-91-554-9231-1
urn:nbn:se:uu:diva-248513

Dissertation presented at Uppsala University to be publicly examined in Å10132 (Häggsalen), Ångström Laboratory, Lägerhyddsvägen 1, Uppsala, Wednesday, 27 May 2015 at 13:30 for the degree of Doctor of Philosophy. The examination will be conducted in English. Faculty examiner: Christophe Delerue (ISEN (Institut Supérieur de l'Électronique et du Numérique)).

Abstract

Kocevski, V. 2015. Theory and Modelling of Functional Materials. *Digital Comprehensive Summaries of Uppsala Dissertations from the Faculty of Science and Technology* 1247. 93 pp. Uppsala: Acta Universitatis Upsaliensis. ISBN 978-91-554-9231-1.

The diverse field of material research has been steadily expanding with a great help from computational physics, especially in the investigation of the fundamental properties of materials. This has driven the computational physics to become one of the main branches of physics, allowing for density functional theory (DFT) to develop as one of the cornerstones of material research. Nowadays, DFT is the method of choice in a great variety of studies, from fundamental properties, to materials modelling and searching for new materials. In this thesis, DFT is employed for the study of a small part of this vast pool of applications. Specifically, the microscopic characteristics of $\text{Zn}_{1-x}\text{Cd}_x\text{S}$ alloys are studied by looking into the evolution of the local structure. In addition, the way to model the growth of graphene on Fe(110) surface is discussed. The structural stability of silicon nanocrystals with various shapes is analysed in detail, as well.

DFT is further used in studying different properties of semiconductor nanocrystals. The size evolution of the character of the band gap in silicon nanocrystals is investigated in terms of changes in the character of the states around the band gap. The influence of various surface impurities on the band gap, as well as on the electronic and optical properties of silicon nanocrystals is further studied. In addition, the future use of silicon nanocrystals in photovoltaic devices is examined by studying the band alignment and the charge densities of silicon nanocrystals embedded in a silicon carbide matrix. Furthermore, the electronic and optical properties of different semiconductor nanocrystals is also investigated. In the case of the CdSe/CdS and CdS/ZnS core-shell nanocrystals the influence of the nanocrystal size and different structural models on their properties is analysed. For silicon nanocrystal capped with organic ligands, the changes in the optical properties and lifetimes is thoroughly examined with changes in the type of organic ligand.

Keywords: nanocrystals, graphene, alloys, density functional theory, optical properties, electronic properties, core-shell structures, semiconductors

Vancho Kocevski, Department of Physics and Astronomy, Materials Theory, Box 516, Uppsala University, SE-751 20 Uppsala, Sweden.

© Vancho Kocevski 2015

ISSN 1651-6214

ISBN 978-91-554-9231-1

urn:nbn:se:uu:diva-248513 (<http://urn.kb.se/resolve?urn=urn:nbn:se:uu:diva-248513>)

Dedicated to my family

List of papers

This thesis is based on the following papers, which are referred to in the text by their Roman numerals.

- I **Transition between direct and indirect band gap in silicon nanocrystals**
V. Kocovski, O. Eriksson, J. Ruzs
Physical Review B 87, 245401 (2013).
- II **Size dependence of the stability, electronic structure, and optical properties of silicon nanocrystals with various surface impurities**
V. Kocovski, O. Eriksson, J. Ruzs
Physical Review B **91**, 125402 (2015).
- III **Band alignment switching and the interaction between neighbouring silicon nanocrystals embedded in a SiC matrix**
V. Kocovski, O. Eriksson, J. Ruzs
Physical Review B, *accepted*.
- IV **First-principles study of the influence of different interfaces and core types on the properties of CdSe/CdS core-shell nanocrystal**
V. Kocovski, J. Ruzs, O. Eriksson, D. D. Sarma
submitted.
- V **Influence of dimensionality and interface type on optical and electronic properties of CdS/ZnS core-shell nanocrystals: A first-principles study**
V. Kocovski, O. Eriksson, C. Gerard, D. D. Sarma, J. Ruzs
submitted.
- VI **Electronic and optical properties of silicon nanocrystals capped with organic ligands studied using first-principles theory**
V. Kocovski
manuscript.
- VII **Formation and structure of graphene waves on Fe(110)**
N. A. Vinogradov, A. A. Zakharov, V. Kocovski, J. Ruzs, K. A. Simonov, O. Eriksson, A. Mikkelsen, E. Lundgren, A. S. Vinogradov, N. Mårtensson, A. B. Preobrajenski
Physical Review Letters **109**, 026101 (2012).

VIII Microscopic description of the evolution of the local structure and an evaluation of the chemical pressure concept in a solid solution

S. Mukherjee, A. Nag, V. Kocevski, P. K. Santra, M. Balasubramanian, S. Chattopadhyay, T. Shibata, F. Schaefer, J. Ruz, C. Gerard, O. Eriksson, C. U. Segre, D. D. Sarma
Physical Review B **89**, 224105 (2014).

Reprints were made with permission from the publishers.

The following papers are co-authored by me, but not included in the thesis

- **Quantitative characterization of nanoscale polycrystalline magnets with electron magnetic circular dichroism**

S. Muto, J. Ruz, K. Tatsumi, R. Adam, S. Arai, V. Kocevski, P. M. Oppeneer, D. E. Bürgler, C. M. Schneider
Nature Communication **5**, 3138 (2014).

Comments on my participation

My participation in Papers I, II, III, IV, V, VI and VIII is in all three parts, planning the research, calculations and writing the manuscript. The experimental part in Paper VIII is performed by the group of D.D. S. The projects in Papers II, III and VI were designed by me. The experimental part in Paper VII is performed by the group of N. A. V.

Contents

1	Introduction	13
2	Theoretical background	19
2.1	Many body problem	19
2.2	Thomas-Fermi-Dirac approximation	20
2.3	Density functional theory	21
2.3.1	Hohenberg-Kohn theorems	21
2.3.2	Kohn-Sham equation	22
2.4	Approximations to the exchange-correlation functional	23
2.4.1	Local Density Approximation	23
2.4.2	Generalised-Gradient Approximation	24
2.5	Computations on solids	24
2.6	Pseudopotentials	25
2.7	Basis set	27
3	SIESTA – our choice of DFT implementation	28
3.1	Norm-conserving pseudopotentials	28
3.2	LCAO basis set	30
3.2.1	Single and multiple zeta basis sets	31
3.2.2	Polarized basis sets	31
3.3	Matrix elements	32
3.4	Total energy	33
4	Quantum confinement regime in silicon nanocrystals	37
4.1	Hydrogenated silicon nanocrystals	38
4.2	Influence of the surface impurities	41
4.3	Embedded silicon nanocrystals	45
5	Semiconductor nanocrystals – significance of the interface and the capping of the surface	49
5.1	Recombination processes in semiconductor nanocrystals	51
5.1.1	Radiative recombination	51
5.1.2	Non-radiative recombination	53
5.1.3	Auger recombination	54
5.2	CdSe/CdS core-shell NCs	54
5.3	CdS/ZnS core-shell NCs	58
5.4	Comparison between CdSe/CdS and CdS/ZnS core-shell NCs ..	61
5.5	Si nanocrystals capped with organic ligands	65

6	Modelling of nanocrystals, surfaces and bulk materials	70
6.1	Ripples of graphene on Fe(110) surface	70
6.2	Silicon nanocrystals with various shapes	71
6.3	Evolution of the local structure in solid solutions	74
7	Summary and outlook	81
8	Sammanfattning	84
	Acknowledgments	87
	References	89

Preface

Greetings dear reader.

The quest for the paramount knowledge, referred to as a doctoral degree, started approximately four and a half years ago, when Dr. Ján Rusz decided to give a chance to the particular candidate to pursue this knowledge. Both of them began the journey not knowing what difficulties and challenges might emerge on the path to the ultimate goal. Any obstacle that the science presented them with was tackled head on, disagreements were overcome, and the laziness (from the student side) was from time to time suppressed. This thesis is the outcome of their mutual productive work, with tremendous help from the second supervisor Prof. Olle Eriksson.

As the title of this thesis suggests, the employment of theoretical methods in studying fundamental properties and modelling of various materials is going to be presented. For smoother following of the main ideas, the content is divided in two parts, and an additional part for the papers.

The first part provides a general introduction to the research field, the topic of the thesis, and the methods employed in studying the particular systems. This could be used as a guidance for easier understanding of the second part and the included papers.

The overview of the most significant results are discussed in the second part. This part is divided in three chapters, in which studies with similar objectives and of related systems are systematised.

I sincerely hope that you are going to enjoy reading this thesis.

Uppsala, April 2015

Vancho Kocovski

FUNDAMENTALS



1. Introduction

The interest in the properties of materials dates back to the dawn of humanity. Our early ancestors realised that using particular stones for a given purpose provided them with an advantage over the other species. This enabled the humans to begin their mastery over the land and resources. Later came the production of more durable tools, with the discovery of iron and bronze, which further cemented the importance of striving to find better materials. At the same time started the search of producing better pottery, finer colours and glazes. Furthermore, the jewellery was becoming a lucrative trade, which relied on the jewellery makers' extensive knowledge of the various precious materials used in the production. Primitive as they are, these can be regarded as the earliest examples of research in materials.

The research started gathering momentum during the Middle Ages, especially in the work of the alchemists. Although their goals were far reaching, their methods of experimenting and the findings that they provided laid the foundation of many sciences, including the basic principles of material research. Things evolved even further in the New Age, when the understanding of the natural world started to progress. The Industrial Revolution brought with it the manufacturing of abundance of other useful products and the requirement for new and better materials. This in turn conceived the importance for investment in materials advances and the research in this field. The newly formed scientist were intrigued by the various features of the materials, which could not be explained using the common knowledge of that time. Particularly valuable was the research in electrical currents and magnetism done by H. A. Lorentz [1] and P. Zeeman [2], respectively. Furthermore, the invention of the cathode-ray tube by K. F. Braun [3] and J. J. Thomson's discovery of the electron [4] marked the start of a new scientific era.

With the discovery of the atomic nucleus by E. Rutherford, which came from the interpretation of the H. Geiger and E. Marsden experiment [5], the need of modelling the atomic inner structure was realised. The most ground-breaking atomic model was proposed by N. Bohr [6–8], who introduced the idea of stationary orbits defined by quantised angular momentum, and the possibility of transitions between these orbits. The idea of quantisation was actually first presented by M. Planck in his *ad hoc* hypothesis [9] that the electronic oscillations are quantised in multiples of h – the Planck's constant. This hypothesis was later extended to the quantisation of the electromagnetic radiation by A. Einstein [10]. In addition to these hypotheses, O. Stern and W. Gerlach provided the first evidence of the quantisation of the spin [11–13].

The introduction of quantisation of energy, angular momentum and the spin, set the stepping-stone for the new physical theory explaining the fundamental behaviour of microscopic particles – the quantum mechanics.

Following these new and exiting findings, the development of formulation of quantum mechanics was steadily moving forward. Almost simultaneously, M. Born, P. Jordan and W. Heisenberg [14–16], on one hand, and E. Schrödinger [17–20] on the other, developed the so-called matrix mechanics and the wave mechanics, respectively. In Schrödinger’s formulation, the quantum system’s dynamics can be represented as a function of the kinetic and the potential energy, given by the equation:

$$i\hbar \frac{\partial}{\partial t} \psi(\mathbf{r}, t) = \left(-\frac{\hbar^2}{2m} \Delta + V(\mathbf{r}) \right) \psi(\mathbf{r}, t). \quad (1.1)$$

where $\psi(\mathbf{r}, t)$ is a many-particle wavefunction, $(-\frac{\hbar^2}{2m} \Delta)$ is the kinetic and $V(\mathbf{r})$ is the potential energy. However, in these formulations of quantum mechanics the spin is not included. To integrate the electron spin in the Schrödinger’s equation, W. Pauli considered the many-particle wavefunction to be antisymmetric [21]. Subsequently, Dirac formulated the relativistic quantum mechanics [22, 23], which in principle can be employed to calculate almost any phenomena dependent on the electronic structure of matter.

Immediately after the foundation of quantum mechanics was established by the wave mechanics formulation, it was evident that properties of atoms, molecules and solids could be obtained by solving the Schrödinger’s equation. However, except for few limited cases, solving the Schrödinger’s equation analytically is almost impossible, which prompt the implementation of approximative ways of solving it. Among the first approximations, now considered as the basic method, and introduced in order to deal with chemically bonded systems, was the Hartree-Fock (HF) theory [24–26]. Although it works sufficiently well for simple systems, the HF theory has a major drawback arising from the employment of single-determinant form of the wavefunction, thus neglecting the electron correlations. This problem was dealt with by treating the electron correlations as perturbation of the HF wavefunction, providing the basics of the many-body perturbation theory (MBPT) [27–29].

A decade after the MBPT was proposed, two distinct methods for solving the many-electron problem were developed almost simultaneously. The first one, Quantum Monte Carlo (QMC), which comprises several different techniques, is based on numerical Monte Carlo integration for solving the many-electron problem. The most widely used QMC techniques are the variational Monte Carlo [30] and the diffusion Monte Carlo [31–33]. The QMC is very accurate, but the calculations are time-consuming and therefore currently it is used only for studying small systems. The second method is density functional theory (DFT) [34, 35], which postulates that the properties of a system are dependent on the electron density, via an exchange-correlation functional,

and the many-body problem is reduced to finding this electron density. Knowing the exact form of the exchange-correlation functional can yield accurate results. However, the exact form of the exchange-correlation functional is beyond current knowledge and many approximations have been instead introduced. In spite of its approximative nature, to date DFT is the most widely used computational method for studying materials. This seeming contradiction will be explained in the rest of this chapter by detailing the significance of DFT in material research. The basics of DFT are summarised in Sec. 2.3.

It is difficult to imagine the modern material research without the input provided from DFT. It not only gives fundamental understanding of the processes on atomistic level, it is also essential in investigating and predicting the properties of materials. There are various aspects of DFT that contribute to this increased importance in material research, compared to other approximative methods. One of the main advantages is the applicability of DFT in describing various distinct classes of materials. More specifically, the experience gained from studying one material can be easily employed for the study of any other. Simple and intuitive, DFT also provides reliable results for different experimentally accessible properties. The increased computational power and the improved implementation of DFT in computational codes further expanded its usability, especially for larger systems. In addition, the popularity of DFT has increased with the introduction of standardised codes and open-source software.

There are though number of shortcomings that should at this point be mentioned. First of all, as a ground-state theory DFT fails to predict excited states, giving unreliable results when it comes to representing emission properties of materials. In addition, the description of van der Waals interactions is incomplete, introducing errors when studying weakly bonded system. Electrons in strongly correlated system are not correctly described by local density approximation (LDA) of the exchange-correlation functional, which wrongly predicts a metallic character of these materials. To solve this problem the LDA+ U approach has been developed, which is based on combining the Coulomb repulsion U of narrow d - and f -bands with DFT description of extended states. Moreover, despite the weaknesses, DFT serves as the foundation for further more sophisticated calculations, termed 'post-DFT' corrections. These methods are employed in order to improve the predictive power of DFT. For example, using many-body perturbation theory, e.g. GW or BSE as an extension to the ground-state DFT, gives more accurate description of the emission properties of materials and their band structures.

Interestingly, the applicability of DFT is wide spread, ranging from studies in nanoscience and nanoengineering, magnetics, elastic and catalytic properties, to biomaterials, geoscience and new emerging materials. Nowadays, a great deal of attention has also been given to the computational spectroscopy and to the study of transport properties in molecular electronics. The possible implementation of the exceptional properties of graphene in everyday devices

has been heavily investigated by relying on the predictive power of DFT. The DFT is also largely utilised in the investigation of electronic and optical properties of nanocrystals, providing explanations for various experimentally observed phenomena. Moreover, when researching for materials with particular physical properties, DFT can give reliable data on elastic properties, defect formation and dislocation behaviour. In the search for new and improved rare-earth free permanent magnets, DFT is not only important in supporting the experimental results, but also in predicting favourable magnetic properties of novel materials.

DFT has proven invaluable also in the study of solid catalysts, especially because it provides an information which is difficult to obtain by experiments. It gives an atomic-scale picture of the way catalysts work by describing the transition states at the surface, which constitute the base for reactivity models. The predictive power of DFT can be also harnessed in areas where experimental results do not exist or are difficult to obtain. It is of great importance in simulating the structural changes in the Earth's core and mantle with changes in pressure and temperature, which is otherwise close to impossible to reproduce in a laboratory. In addition, DFT is the main tool of the emerging research area known as the high-throughput computational materials design used in screening for new materials. The method is based on gathering thermodynamic and electronic properties data for a large number of systems, and combining it with data mining to find materials with desired properties. Have in mind that beside these examples, there are many other instances where DFT helps in explaining and predicting fundamental properties of matter, but have been left out from this list.

One of the main reason for the widespread use of DFT in material research comes from the implementation of efficient algorithms for solving the quantum mechanical equations. The variety of codes in which DFT is implemented employ different ways of solving the Kohn-Sham equations, and have various choices of basis sets, potentials and exchange-correlation functionals. Choosing a particular code mainly depends on the size of the studied system and the required level of accuracy of the obtained results. Currently, the most accurate codes are based on all-electron approaches, including relativistic effects, and a combination of plane waves with localised orbitals as basis set. However, the calculations performed using these codes are highly time consuming, even with the considerable advancements in computational power. Therefore, for large systems one resorts to using codes based on pseudopotentials and localised basis sets, for which lower computational cost is required, but still provide rather accurate results. This thesis centers around the usability of DFT in modelling nanocrystals, surfaces and bulk material. Considering the large size of the systems, a few thousands of atoms, we used the DFT code SIESTA [36, 37], based on pseudopotentials and localised basis sets. Details regarding the basic implementation of SIESTA are given in Chapter 3.

The research in nanostructured materials relies greatly on the capabilities of DFT to provide explanations for the experimentally observed phenomena. In various occasions DFT has managed to give deeper insight into the surface reconstruction of nanomaterials, the effect of doping on their properties and into the possibility of designing new and improved nanomaterials. Of great importance is also the study of electronic and optical properties of nanocrystals for future use in microelectronics. The usability of DFT in studying large nanocrystals, with sizes closer to the experimentally analysed ones, however was limited due to the efficiency of the existing DFT codes. A significant boost to the large scale calculations came with the implementation of localised basis sets and pseudopotentials, coupled with the ever-growing power of the supercomputers. These improvements in computations enabled us to study the optical and electronic properties of various nanocrystals with sizes comparable to the experimental ones.

The great significance of producing nanocrystals for light emitting applications comes from exploiting the quantum confinement effect that they exhibit. By confining the size of the nanocrystals, both the energy and the intensity of the emitted light increase. Moreover, even nanocrystals made from indirect band gap semiconductors, e.g. Si and Ge, in which the emission of light must be coupled with a phonon, exhibit increased photoluminescence. The abundance of silicon and the easy way of producing silicon nanocrystals, together with the high photoluminescence, has sparked considerable interest in studying the usability of silicon nanocrystals. The wide spread of experimental results and the unexpected photoluminescence of an indirect band gap semiconductor, has drawn the attention of theoreticians aimed to provide a detailed explanation for these surprising results with the help of DFT. The realisation that surface oxidation can significantly influence the photoluminescence of silicon nanocrystals, has risen even further the interest for using DFT in obtaining fundamental understanding of the processes taking place in silicon nanocrystals.

Although there exists studies that give an explanation of the experimentally observed phenomena in hydrogenated [38] and oxygenated silicon nanocrystals [39], they are based on the tight-binding model. To provide a more accurate theoretical description of the processes occurring in these nanocrystals, parameter-free DFT is preferably used. This was the main aim in our study of silicon nanocrystals. We investigated the size evolution of the fundamental and optical band gap in hydrogenated silicon nanocrystals, and nanocrystals with various surface impurities. This was further extended to studying the changes in the wavefunctions of the highest occupied (HOMO) and lowest unoccupied (LUMO) eigenstate, with changes in the nanocrystal size and type of surface impurity.

To suppress the oxidation of the silicon nanocrystals' surface, the nanocrystals are capped with organic ligands, which improves their photoluminescence properties. Moreover, different organic ligands can have distinct influence on

the photoluminescence of the silicon nanocrystals. Understanding the changes in the optical and electronic properties of silicon nanocrystals capped with different organic ligands, was also one of the objective of this thesis. Capping the surface of the nanocrystals, to reduce the influence of surface effects and improve their photoluminescence, is not specific only for silicon nanocrystals. II-VI semiconductor nanocrystals, for example, are frequently capped with other semiconductor (forming core-shell nanocrystals) in order to suppress the surface effects and enable manipulation of their properties for a specific purpose. In addition, the photoluminescence properties can be influenced by changes in the structure of the core or the core-shell interface.

Of significant interest are the core-shell structures where both the electron and hole are confined within the core of the nanocrystals, especially because of their enhanced light emitting properties. Important representatives of this type of systems are the CdSe/CdS and CdS/ZnS core-shell nanocrystals, which despite the large number of experimental studies, has not been previously studied using more accurate first-principles theory. Therefore, we set our objective in demonstrating the size dependence and the influence of the different structural models on the electronic and optical properties of these core-shell nanocrystals. Furthermore, we relate the calculated radiative lifetimes and electron-hole Coulomb interaction energies with experimentally observed quantities, in order to show the differences in the properties of the two types of core-shell nanocrystals and the properties related to the distinct structural models.

The improved properties of the semiconductors upon nanocrystal formation, can be also utilised in photovoltaic applications, but this is only applicable if the nanocrystals are embedded in a host matrix. Among many semiconductor nanocrystals, the silicon nanocrystals have triggered the highest interest for producing new-generation solar cells. It is important, therefore, to find a suitable host matrix, which gives high light conversion efficiency, by reducing the recombination rates of the charge carrier and increasing their mobility. We focused on the study on SiC as a host matrix, investigating the band alignment between the silicon nanocrystal and the SiC matrix, which can provide valuable information regarding the recombination rates between the charge carriers. In addition, we looked into the possibility of increasing charge transport by having leakage between states.

In other parts of the thesis, collaborative studies with experiments are given, showing the capability of DFT to reliably model the structure of bulk materials, surfaces and nanocrystals. The investigation the $\text{Zn}_{1-x}\text{Cd}_x\text{S}$ ternary alloys, aimed in providing more fundamental, microscopic understanding of the structural characteristics is presented. Modelling of the formation of graphene on Fe(110) surface, with focus on the buckling effect, is also given. Considerable attention in this thesis has been given to DFT study of silicon nanocrystals. Hence, before performing detailed calculations of the electronic and optical properties, we studied the stability of nanocrystals with various shapes.

2. Theoretical background

2.1 Many body problem

From the basics of quantum mechanics follows that the properties of a system can be obtained by solving a many body equation, which for non-relativistic time-independent calculations is the Schrödinger equation:

$$H\psi(\mathbf{r}_1, \mathbf{r}_2, \dots, \mathbf{R}_1, \mathbf{R}_2, \dots) = E\psi(\mathbf{r}_1, \mathbf{r}_2, \dots, \mathbf{R}_1, \mathbf{R}_2, \dots), \quad (2.1)$$

where $\psi(\mathbf{r}_1, \mathbf{r}_2, \dots, \mathbf{R}_1, \mathbf{R}_2, \dots)$ is the all electron wavefunction, which depends on the position of the electrons, \mathbf{r} , and the nuclei, \mathbf{R} . H represents the Hamiltonian of the interacting system, which can be expressed as:

$$\begin{aligned} H = & -\frac{\hbar^2}{2m_e} \sum_i \nabla_i^2 - \sum_I \frac{\hbar^2}{2m_I} \nabla_I^2 - \sum_{i,I} \frac{Z_I e^2}{|\mathbf{r}_i - \mathbf{R}_I|} + \\ & + \frac{1}{2} \sum_{i \neq j} \frac{e^2}{|\mathbf{r}_i - \mathbf{r}_j|} + \frac{1}{2} \sum_{I \neq J} \frac{Z_I Z_J e^2}{|\mathbf{R}_I - \mathbf{R}_J|}, \end{aligned} \quad (2.2)$$

where m_e and m_I are the mass of the i^{th} electron and I^{th} nucleus, respectively, and Z_I is the atomic number of the I^{th} atom. The first and the second term are respectively the kinetic energy of the electrons and the nuclei. The remaining three terms are the potential energy from Coulomb interaction between electron and nucleus, electron and electron, and nucleus and nucleus, respectively.

However, as mentioned in the introduction, obtaining analytical solution of the Schrödinger equation in this form is limited to a small number of systems, and to broaden its applicability to every system, approximations need to be implemented. The first approximation utilises the large mass difference between the nuclei and the electrons (nuclei are 3-5 orders of magnitude more massive than electrons), which causes almost instantaneous adaptation of the dynamics of electrons to the position of the nuclei. Hence, the dynamics of the nuclei could be neglected, considering them as “frozen” (static), which is the basis of the Born-Oppenheimer (BO) approximation [40]. By fixing the position of the nuclei the Hamiltonian takes the present form, in atomic units¹

$$H = -\frac{1}{2} \sum_i \nabla_i^2 - \sum_{i,I} \frac{Z_I}{|\mathbf{r}_i - \mathbf{R}_I|} + \frac{1}{2} \sum_{i \neq j} \frac{1}{|\mathbf{r}_i - \mathbf{r}_j|}. \quad (2.3)$$

Although using this approximation does not give simplified solution of the many body Schrödinger equation, it is the first step towards obtaining a solution. The persisting problem comes with the necessity to solve the many body equation for a system of N interacting electrons.

¹This notation is going to be used throughout the thesis for consistency.

2.2 Thomas-Fermi-Dirac approximation

Significant advance in solving the many body problem was achieved with the development of a semi-classical model by L. Thomas and E. Fermi [41, 42], in which the all electron wavefunction, ψ , is substituted by the electron density, $n(\mathbf{r})$

$$n(\mathbf{r}) = \int d\mathbf{r} |\psi_i(\mathbf{r})|^2. \quad (2.4)$$

In doing so, the issue of dealing with N interacting electrons is scale down to regarding only the density, which is actual physical observable. Thomas and Fermi also postulated that the total energy of a system can be defined as a functional of the density, $E[n]$, and solving this functional can yield the ground state energy. In this sense the Thomas-Fermi model is considered to be a precursor to the Density Functional Theory (DFT). The energy functional in Thomas-Fermi (TF) model is given by:

$$E_{\text{TF}}[n] = \frac{3}{10} (3\pi^2)^{2/3} \int d\mathbf{r} n^{5/3}(\mathbf{r}) - Z_I \int d\mathbf{r} \frac{n(\mathbf{r})}{r} + \frac{1}{2} \int \int d\mathbf{r} d\mathbf{r}' \frac{n(\mathbf{r})n(\mathbf{r}')}{|\mathbf{r} - \mathbf{r}'|}, \quad (2.5)$$

where the first term is the kinetic energy, the second term is the Coulomb interaction between the electron and the nucleus, and the third term is the electron-electron Coulomb repulsion. In this form of the Thomas-Fermi model the exchange and correlation of electrons are not included. The model was extended by Dirac by introducing exchange interaction term, based on uniform electron gas [43], providing the equation:

$$E_{\text{TFD}}[n] = E_{\text{TF}}[n] - \frac{3}{4} \left(\frac{3}{\pi} \right)^{1/3} \int d\mathbf{r} n^{4/3}(\mathbf{r}). \quad (2.6)$$

The Lagrange multiplier method can be used to minimise the energy functional, considering the normalisation constant $\int d\mathbf{r} n(\mathbf{r}) = N$, obtaining the ground state energy by solving

$$\frac{1}{2} (3\pi^2)^{(2/3)} n(\mathbf{r})^{(2/3)} + V(\mathbf{r}) - \mu = 0, \quad (2.7)$$

where μ is the Lagrange multiplier, and $V(\mathbf{r}) = V_{\text{ext}}(\mathbf{r}) + V_H(\mathbf{r}) + V_x(\mathbf{r})$ is the total potential, where $V_{\text{ext}}(\mathbf{r})$ is the external potential

$$V_{\text{ext}}(\mathbf{r}) = -\frac{Z_I}{r}, \quad (2.8)$$

$V_H(\mathbf{r})$ is the Hartree potential, defined as

$$V_H(\mathbf{r}) = \int d\mathbf{r}' \frac{n(\mathbf{r}')}{|\mathbf{r} - \mathbf{r}'|}. \quad (2.9)$$

and the last term, $V_x(\mathbf{r})$, is the Dirac-Slater exchange potential

$$V_x(\mathbf{r}) = -\frac{3}{\pi}n^{1/3}(\mathbf{r}). \quad (2.10)$$

2.3 Density functional theory

Going beyond the Thomas-Fermi approximation, which states that electronic properties can be calculated using the electron density, Hohenberg and Kohn in their two theorems showed that indeed any property of an interacting system can be obtained from the ground state electron density, $n_0(\mathbf{r})$. This is the foundation of the DFT. The DFT was further developed in a practical numerical method with the introduction of the Kohn-Sham formalism, which substitutes the many body problem with an independent particle problem.

2.3.1 Hohenberg-Kohn theorems

The Hohenberg-Kohn formalism [34] of DFT is based on two theorems:

Theorem I

For any system of interacting particles in an external potential $V_{\text{ext}}(\mathbf{r})$, the potential $V_{\text{ext}}(\mathbf{r})$ is determined uniquely, up to a constant, by the ground state particle density, $n_0(\mathbf{r})$.

Corollary I

Considering that the Hamiltonian is fully determined from $n_0(\mathbf{r})$, except for a constant shift of the energy, it follows that the many body wavefunctions for all states (ground and excited) and the properties of the system are also completely determined.

Theorem II

A universal functional for the energy $E[n]$ in terms of density $n(\mathbf{r})$ can be defined for any external potential V_{ext} . For any particular V_{ext} , the ground state energy of the system is the global minimum of the energy functional, and the density $n(\mathbf{r})$ which minimises the functional is the exact ground state density $n_0(\mathbf{r})$.

Following the two theorems of Hohenberg and Kohn, the energy functional defined in the Thomas-Fermi-Dirac approximation, can be rewritten as:

$$E[n] = \int d\mathbf{r} V_{\text{ext}}(\mathbf{r})n(\mathbf{r}) + F[n], \quad (2.11)$$

where the functional $F[n]$ incorporates the kinetic and the potential energy, coming from the all electron-electron interactions. Since this functional does

not depend on the external potential, the kinetic and potential energies depend only on the density; hence the functional must be the same for any system. $F[n]$ can be further split into

$$F[n] = T_S[n] + E_{int}[n], \quad (2.12)$$

where $T_S[n]$ is the kinetic energy, and $E_{int}[n]$ is the interaction energy, which is defined as

$$E_{int}[n] = \frac{1}{2} \int d\mathbf{r} d\mathbf{r}' \frac{n(\mathbf{r})n(\mathbf{r}')}{|\mathbf{r} - \mathbf{r}'|} + E_{xc}[n], \quad (2.13)$$

where the first term is the Hartree energy, and the second term is the exchange-correlation energy, in which all the many particle interactions are gathered.

The exact ground state properties could be obtained using variational methods to minimise the functional $E[n]$ with respect to the density. This is valid only when the exact form of the exchange-correlation potentials is known. However, for a system of interacting electrons this is not the case. In addition, the effective potential on which the density depends can be influenced by changes in the density. Introducing self-consistent cycle can solve this problem.

2.3.2 Kohn-Sham equation

The essential change introduced in the Hohenberg and Kohn theory by the Kohn-Sham formalism is the replacement of the many body equation with a single particle equation, while keeping constant the total number of interacting particles. According to the formalism, the total energy functional can be written as

$$E[n] = T_S[n] + \int d\mathbf{r} \left[V_{ext}(\mathbf{r}) + \frac{1}{2} V_H(\mathbf{r}) \right] n(\mathbf{r}) + E_{xc}[n]. \quad (2.14)$$

$T_S[n]$ is the kinetic energy of the electrons, $E_{xc}[n]$ is the exchange-correlation functional, V_H is the Hartree potential, as in Eq. 2.9, and V_{ext} is the external potential, defined as

$$V_{ext} = - \sum_I \frac{Z_I}{|\mathbf{R} - \mathbf{r}|}. \quad (2.15)$$

Minimizing the Eq. 2.14 with respect to the density yields a Schrödinger-like equation, known as the Kohn-Sham (KS) equation, which is expressed as

$$H_{eff}(\mathbf{r})\psi_i(\mathbf{r}) = \left[-\frac{1}{2}\nabla^2 + V_{eff}(\mathbf{r}) \right] \psi_i(\mathbf{r}) = \varepsilon_i \psi_i(\mathbf{r}), \quad (2.16)$$

showing that the independent particles are moving in an effective potential, V_{eff} . In the V_{eff} the external potential, the Hartree potential and the exchange-correlation potential, $V_{xc} = \frac{\delta E_{xc}[n]}{\delta n(\mathbf{r})}$ are included. Using an initial guess of electron density to solve the KS equation, gives the KS wavefunctions, ψ_i , which

are then used to calculate the electron density

$$n(\mathbf{r}) = \sum_{i=1}^N |\psi_i(\mathbf{r})|^2, \quad (2.17)$$

N being the number of occupied states. This newly calculated electron density is later used to calculate new effective potential. This is repeated until self-consistency is achieved.

From Eq. 2.16 the kinetic energy can be expressed by:

$$T_S[n] = \sum_{i=1}^N \epsilon_i - \int d\mathbf{r} V_{eff}(r) n(\mathbf{r}). \quad (2.18)$$

Ultimately, the total energy of the system is given by

$$E = \sum_{i=1}^N \epsilon_i - \frac{1}{2} \int d\mathbf{r} d\mathbf{r}' \frac{n(\mathbf{r})n(\mathbf{r}')}{|\mathbf{r} - \mathbf{r}'|} - \int d\mathbf{r} V_{xc}(\mathbf{r}) n(\mathbf{r}) + E_{xc}[n]. \quad (2.19)$$

The most appealing property of this formalism is that the kinetic energy and the Hartree terms are explicitly separated and can be calculated accurately. Therefore, the limiting factor in providing accurate results is the exchange-correlation term, the form of which, if it would be exactly known, would make this formalism an exact one. This seemingly trivial simplification has pushed the Kohn-Sham formalism to become the most widely used method for solving the many-electron problems.

2.4 Approximations to the exchange-correlation functional

The total energy expression, Eq. 2.19, can yield exact solution only when the exact form of the E_{xc} is known. However, obtaining an exact expression for this functional has proven to be a very complex and still unsolved problem. Therefore, approximations of the E_{xc} functional need to be implemented and tested with respect to the energy of the exact ground state. In the following section an overview of the two most widely used approximations of the exchange-correlation functional is going to be presented.

2.4.1 Local Density Approximation

When Kohn and Sham first introduced their formalism, they also proposed the first approximation of the exchange-correlation functional, the local density approximation (LDA) [35]. The electron density is treated locally as an uniform electron gas, and the exchange-correlation energy is considered to be the

same as the energy of the uniform electron gas at any local point in space. In LDA the exchange-correlation functional can be written as

$$E_{xc}^{LDA}[n] = \int d\mathbf{r} n(\mathbf{r}) \epsilon_{xc}(n), \quad (2.20)$$

where ϵ_{xc} is the exchange-correlation energy per particle. The ϵ_{xc} can be further divided into exchange, ϵ_x , and correlation, ϵ_c , terms

$$\epsilon_{xc}(n) = \epsilon_x(n) + \epsilon_c(n). \quad (2.21)$$

The ϵ_x term can be explicitly evaluated from the Hartree-Fock method. On the other hand, the analytical form of the ϵ_c is not known. Thus numerical forms of ϵ_c are used, which have been obtained by fitting on accurate data from Quantum Monte Carlo calculations [44]. Despite the simplicity, LDA is one of the most widely used functionals in various studies.

2.4.2 Generalised-Gradient Approximation

To overcome some of the limitations of LDA, a method was developed that not only uses the locality of the density, but also takes into account the derivative of the density at the same coordinate. This method is known as Generalised-Gradient approximation (GGA) [45, 46], in which the exchange-correlation functional is given by

$$E_{xc}^{GGA}[n] = \int d\mathbf{r} n(\mathbf{r}) \epsilon_{xc}(n, |\nabla n|), \quad (2.22)$$

where ϵ_{xc} can be expressed as the homogeneous ϵ_x enhanced by a factor F_{xc} . Then the exchange-correlation functional can be written as

$$E_{xc}^{GGA}[n] = \int d\mathbf{r} n(\mathbf{r}) \epsilon_x^{LDA} F_{xc}(n, |\nabla n|), \quad (2.23)$$

where F_{xc} is a functional of the electron density and its gradient. Compared to LDA, GGA gives often better results when calculating structural properties cohesive energies, phase transitions, and various other properties.

2.5 Computations on solids

The methods discussed so far are only applicable for systems with finite number of electrons, like atoms and molecules. However, due to the infinite number of electrons in crystals, the DFT approximation cannot be used directly and further development is needed. In a crystal, due to the periodicity the potential also must be periodic and therefore the effective potential V_{eff} in the KS equation can be considered to follow the crystal periodicity

$$V_{eff}(\mathbf{r} + \mathbf{R}) = V_{eff}(\mathbf{r}), \quad (2.24)$$

where \mathbf{R} is the translation vector. Using the Bloch theorem [47], the single particle wavefunctions can be written as

$$\psi_{i,\mathbf{k}}(\mathbf{r}) = e^{i\mathbf{k}\cdot\mathbf{r}} u_{i,\mathbf{k}}(\mathbf{r}), \quad (2.25)$$

where $u_{i,\mathbf{k}}(\mathbf{r})$ is a periodic function of the lattice, i.e. $u_{i,\mathbf{k}}(\mathbf{r}) = u_{i,\mathbf{k}}(\mathbf{r} + \mathbf{R})$, and \mathbf{k} is the wave vector. Expressing the periodic function, $u_{i,\mathbf{k}}(\mathbf{r})$, in a Fourier series

$$u_{i,\mathbf{k}}(\mathbf{r}) = \sum_{\mathbf{G}} c_{i,\mathbf{G}} e^{i\mathbf{G}\cdot\mathbf{r}}, \quad (2.26)$$

where \mathbf{G} is the reciprocal lattice vector, the $c_{i,\mathbf{G}}$ are the plane-wave expansion coefficients. To fulfil the periodicity of the system $\mathbf{G} \cdot \mathbf{R} = 2\pi m$, m being an integer. Consequently, the single particle wavefunction can be expressed in a linear combination of plane waves

$$\psi_{i,\mathbf{k}}(\mathbf{r}) = \sum_{\mathbf{G}} c_{i,\mathbf{k}+\mathbf{G}} e^{i(\mathbf{k}+\mathbf{G})\cdot\mathbf{r}}. \quad (2.27)$$

In this way, in an infinite solid the problem of having infinite number of electrons is reduced to having infinite number of \mathbf{k} -points, which might seem somewhat contradicting. However, it allows a great simplification because the $\psi_{i,\mathbf{k}}(\mathbf{r})$ changes smoothly along the close \mathbf{k} -points; thus by taking only one \mathbf{k} -point, a small region can be sampled. Therefore, it is sufficient to consider discrete number of \mathbf{k} -points in order to calculate the electronic structure of a solid. Further simplifications of the calculations are done by taking advantage of the possibility to confine any \mathbf{k} -vector to the first Brillouin zone and considering only the \mathbf{k} -points inside it.

2.6 Pseudopotentials

Since they were originally introduced to simplify the electronic structure calculations, the pseudopotentials enjoy a great popularity in variety of studies. Their transferability to electronic structure calculations of different systems has even further appealed to their users. Because the valence electrons determine the atomic properties, the main interest is in their properties. In addition, due to the screening of the nucleus charge from the core electrons, the valence electrons are more weakly bound than the core electrons. Therefore, it is suitable to introduce an effective pseudopotential, which is weaker than the strong Coulomb potential in the core region, and a pseudo wavefunction, which will be nodeless and vary smoothly in the core region, to replace the rapidly oscillating valence electron wavefunction. This is schematically shown in Fig. 2.1.

To demonstrate the construction of a pseudopotential, let's first consider exact core and valence states, $|\psi_c\rangle$ and $|\psi_v\rangle$, for which the Schrödinger equation can be written as

$$H |\psi_i\rangle = E_i |\psi_i\rangle, \quad (2.28)$$

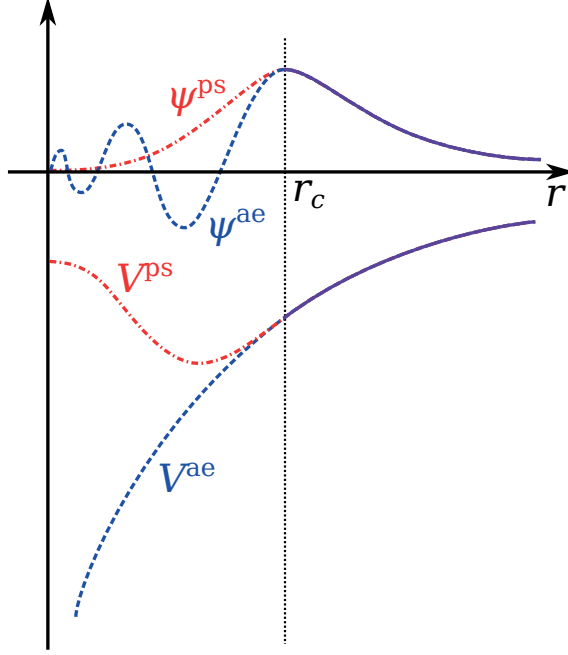


Figure 2.1. Schematic representation of the pseudopotential concept. The nodeless pseudopotential pseudo wavefunction ψ^{ps} (red line) matches the all electron ψ^{ae} (blue line), beyond the cutoff radius, r_c , inducing softer pseudo potential V^{ps} , compared to the all electron potential $V^{\text{ae}} \sim \frac{-Z}{r}$.

where i stands for both core and valence states. The interest is to smoothen the valence states in the core region; thus, the core orthogonality wiggles can be subtracted from the valence states, leading to pseudostates, $|\phi_v\rangle$, given by

$$|\phi_v\rangle = |\psi_v\rangle + \sum_c |\psi_c\rangle \alpha_{cv}, \quad (2.29)$$

where the summation is over the states in the core region, and $\alpha_{cv} = \langle \psi_c | \phi_v \rangle$.

Inserting Eq. 2.29 into Eq. 2.28 yields

$$\begin{aligned} H |\phi_v\rangle &= E_v |\psi_v\rangle + \sum_c E_c |\psi_c\rangle \alpha_{cv} = \\ &= E_v |\phi_v\rangle + \sum_c (E_c - E_v) |\psi_c\rangle \alpha_{cv} = E_v |\phi_v\rangle. \end{aligned} \quad (2.30)$$

Hence,

$$\left[H + \sum_c (E_v - E_c) |\psi_c\rangle \langle \psi_c| \right] |\phi_v\rangle = E_v |\phi_v\rangle, \quad (2.31)$$

from which follows that the pseudostates $|\phi_v\rangle$ satisfy the Schrödinger equation with a pseudo-Hamiltonian

$$H^{\text{ps}} = H + \sum_c (E_v - E_c) |\psi_c\rangle \langle \psi_c|, \quad (2.32)$$

and pseudopotential

$$V^{\text{ps}} = V + \sum_c (E_v - E_c) |\psi_c\rangle \langle \psi_c|. \quad (2.33)$$

The first term in the pseudopotential is the true potential, and the second is the repulsive potential, which softens the core potential, by cancelling the strong Coulomb potential, and the resulting pseudo wavefunction is nodeless.

2.7 Basis set

Before going into details regarding the basic concept of basis sets, let us have a short reminder of the KS formalism. In KS DFT the electrons are moving in an effective potential V_{eff} , and satisfy the Kohn-Sham eigenvalue equation (see also Eq. 2.16):

$$H_{\text{eff}}(\mathbf{r})\psi_i(\mathbf{r}) = \left[-\frac{\hbar^2}{2m_e} \nabla^2 + V_{\text{eff}}(\mathbf{r}) \right] \psi_i(\mathbf{r}) = \varepsilon_i \psi_i(\mathbf{r}). \quad (2.34)$$

From the Bloch theorem, and the periodicity of the effective potential V_{eff} , the single particle wavefunction can be written as (see also Eq. 2.25)

$$\psi_{\mathbf{k}}(\mathbf{r}) = e^{i\mathbf{k}\cdot\mathbf{r}} u_{\mathbf{k}}(\mathbf{r}). \quad (2.35)$$

In order to solve the the KS equation, the single particle wavefunction can be expanded in a complete basis set of functions $\{\phi_i(\mathbf{r})\}$:

$$\psi_{n\mathbf{k}}(\mathbf{r}) = \sum_i c_{i,n} \phi_{i,\mathbf{k}}(\mathbf{r}). \quad (2.36)$$

The coefficients $c_{i,n}$ can be obtained by solving

$$\sum_j [\langle \phi_{i,\mathbf{k}} | H | \phi_{j,\mathbf{k}} \rangle - \varepsilon_{n\mathbf{k}} \langle \phi_{i,\mathbf{k}} | \phi_{j,\mathbf{k}} \rangle] c_{j,n\mathbf{k}} = 0. \quad (2.37)$$

The first and the second term in Eq. 2.37 are the effective Hamiltonian and the overlap matrix element, respectively. The eigenvalues then can be obtained by solving the secular equation

$$\det[\langle \phi_{i,\mathbf{k}} | H | \phi_{j,\mathbf{k}} \rangle - \varepsilon_{n\mathbf{k}} \langle \phi_{i,\mathbf{k}} | \phi_{j,\mathbf{k}} \rangle] = 0. \quad (2.38)$$

The basis sets can be formed in different ways depending on the studied systems and the required accuracy. Linear muffin-tin orbitals (LMTO), linear combination of atomic orbitals (LCAO), planes wave (PW), and linearised augmented plane waves (LAPW) are examples of the most widely used basis sets.

3. SIESTA – our choice of DFT implementation

The method SIESTA, short for Spanish Initiative for Electronic Simulations with Thousands of Atoms, which is also implemented in the computational code SIESTA, was developed with primary goal to perform fast DFT calculations. Since its development, the computational power has risen substantially, allowing for calculations of various properties of considerably large systems, with > 1000 atoms. Provided that the systems in our study fall in this category, naturally SIESTA was the code of our choice. In this chapter a brief introduction in the method's cornerstones that significantly increases the efficiency of solving the DFT Kohn-Sham equation are presented. The concept of non-local pseudopotentials, basis sets based on atomic orbitals, and the basic method for calculating matrix elements and total energies implemented in SIESTA are discussed. One should keep in mind that only few aspects of otherwise vast implementation of the SIESTA method are summarised here. More details can be found in the Soler *et al.* review of the method [37].

3.1 Norm-conserving pseudopotentials

In pseudopotential methods, the first step in gaining efficiency in solid-state calculations is to generate a pseudopotential from a simple environment, e.g. spherical atom, which further can be used for more complex systems. This type of pseudopotential is termed “good” *ab initio* pseudopotential, and it is required to reproduce the logarithmic derivatives of the all electron wavefunction outside a given cutoff radius, r_c . In addition, beyond r_c there should be also an agreement between the first energy derivative of the all electron wavefunction and the pseudo wavefunction. Pseudopotentials which satisfy this criteria were first proposed by Hammann, Schlüter and Chiang [48]. Interestingly, they were named norm-conserving pseudopotentials, due to the requirement of conservation of the norm below the r_c , i.e. the charge densities of the pseudo, ψ^{ps} , and all electron, ψ , wavefunctions agree below the r_c :

$$\int_0^{r_c} d\mathbf{r} |\psi^{\text{ps}}(\mathbf{r})|^2 = \int_0^{r_c} d\mathbf{r} |\psi(\mathbf{r})|^2. \quad (3.1)$$

This condition ensures that above r_c the normalised pseudo wavefunction and the all electron wavefunction agree.

The construction of a pseudopotential, from given all electron information, starts with generating a screened pseudopotential, V^{sc} . As previously shown, imposing the norm-conservation ensures that this screened pseudopotential and the all electron potential agree in the valence region, $r > r_c$. However, this condition does not provide the form of the pseudopotential in the core region. One of the most widely used methods for determining the form of a pseudopotential in the core region is the Troullier-Martins (TM) approach [49]. In the TM approach, the pseudo wavefunction is made to satisfy: (i) norm-conservation of the charge density in the core region; (ii) continuity of the pseudo wavefunction and its logarithmic derivative and first energy derivative at r_c ; and (iii) smooth pseudopotential form, which comes from the zero curvature at the origin.

This screened pseudopotential contains the interaction between the atomic valence states, which is different from valence states interactions in molecules or solids. Therefore, to make the screened pseudopotential transferable to various environments, it is very useful to remove the screening, i.e. “unscreen” the valence states and derive an ion pseudopotential. This new ion pseudopotential is termed unscreened pseudopotential, V^{usc} , and can be obtained by subtracting the calculated Hartree, V_H , and exchange-correlation, V_{xc} potentials for the valence electrons from the screened pseudopotential, i.e.

$$V^{\text{usc}}(\mathbf{r}) = V^{\text{sc}}(\mathbf{r}) - V_H(n_v(\mathbf{r})) - V_{xc}(n_v(\mathbf{r})), \quad (3.2)$$

where the electron density, n_v , is defined as

$$n_v(\mathbf{r}) = \sum_{l=0}^{l_{\text{max}}} \sum_{m=-l}^l |\psi_{lm}^{\text{ps}}|^2, \quad (3.3)$$

where l_{max} is the highest angular momentum in the isolated atom.

The newly introduced pseudopotential has a spherically symmetric form, which comes from the symmetry of the core states. Therefore, it is possible to treat each angular momentum (l) separately, which leads to l -dependent pseudopotential, $V_l(\mathbf{r})$. A further improvement of the $V_l(\mathbf{r})$ can be made by introducing separable potentials $\delta V^{\text{KB}}(\mathbf{r})$ that are fully non-local in the angles θ , ϕ , and the radius, r , which was proposed by Kleinman and Bylander (KB) [50]. This new, non-local pseudopotential can be written as

$$V^{\text{KB}} = V^{\text{local}} + \sum_{lm} \frac{|\delta V_l \phi_{lm}\rangle \langle \phi_{lm} \delta V_l|}{\langle \phi_{lm} | \delta V_l | \phi_{lm} \rangle}, \quad (3.4)$$

where $V^{\text{local}}(\mathbf{r})$ is the local potential, ϕ_{lm} is the eigenstate of the atomic pseudo Hamiltonian and $|\delta V_l \phi_{lm}\rangle$ are projectors that operate on the wavefunction

$$\langle \psi | \delta V_l \phi_{lm} \rangle = \int d\mathbf{r} \psi(\mathbf{r}) \delta V_l(\mathbf{r}) \phi_{lm}(\mathbf{r}). \quad (3.5)$$

The $\delta V^{\text{KB}}(\mathbf{r})$ and $\delta V_l(\mathbf{r})$ operate on the ϕ_{lm} in the same manner, which shows that non-local pseudopotential is a good approximation. Moreover, the separable form makes any calculations faster, because the matrix elements require only products of projection operators, and they scale linearly with the number of basis functions.

3.2 LCAO basis set

The linear combination of atomic orbitals (LCAO) basis sets were first introduced in quantum chemistry for describing molecular orbitals. Eventually they found their way in solid-state calculations, especially in the Order- N DFT methods (methods that scale linearly with system size). As the name implies, the LCAO basis sets are essentially a superposition of atomic orbitals (AO), which can be written as

$$\phi_{nlm} = \sum_i c_{i,nlm} \chi_{i,nlm} \quad (3.6)$$

where ϕ_{nlm} is the basis orbital, $c_{i,nlm}$ are the AO coefficients and the summation is over the number of AO, $\chi_{i,nlm}$. Mostly used AO basis functions are the Slater Type Orbitals (STO) [51] and the Gaussian Type Orbitals (GTO) [52]. Both of these types of AO have the same form

$$\chi_{nlm}(r, \theta, \varphi) = R_{nl}(r) Y_{lm}(\theta, \varphi) \quad (3.7)$$

where $Y_{l,m}(\theta, \varphi)$ are the spherical harmonic functions, with the main difference in the radial part $R_{nl}(r)$. The radial parts of the STO and GTO are

$$\text{STO: } R_{nl}(r) = N_{nl}(\zeta) r^{n-1} e^{-\zeta r}, \quad (3.8)$$

$$\text{GTO: } R_{nl}(r) = N_{nl}(\alpha) r^{n-1} e^{-\alpha r^2}, \quad (3.9)$$

where n is a natural number, having similar role as the principal quantum number, and N_{nl} is a normalisation constant. In STO ζ is a constant related to the nucleus effective charge, and in GTO α is the orbital exponent. Although the STO give more accurate description of the AO, the GTO can be numerically solved more efficiently, which makes the GTO the primary choice in most of the computational codes based on LCAO.

To increase the efficiency, basis orbitals that are confined within a given cutoff radius are used in SIESTA. For an atom i , located at \mathbf{R}_i , these basis orbitals have the following form

$$\phi_{i,nlm}(\mathbf{r}) = R_{i,nl}(\mathbf{r}_i) Y_{lm} \quad (3.10)$$

where $\mathbf{r}_i = \mathbf{r} - \mathbf{R}_i$, and $R_{i,nl}(\mathbf{r}_i)$ is a numerical radial function. The index n indicates the number of orbitals which have different radial dependence, but the

same angular dependence, referred to as multiple- ζ (zeta). Considering that Y_{lm} have a known form, the only requirement left to define the basis function is to specify the form of the radial functions. The form of the radial functions and the cutoff radius can be assigned automatically or they can be defined by the user, allowing for further influence on the accuracy of the calculations.

3.2.1 Single and multiple zeta basis sets

The most basic description of a free atom can be obtained by considering only one basis function for each atomic orbital. Because of the use of the minimum number of basis orbitals, this type of basis set is termed minimal basis set, also known as single-zeta (single- ζ , SZ) basis set. The term zeta comes from the Greek letter ζ (zeta), which is used to denote the exponent of the STO basis function (see the previous section). Having the minimality in mind, the SZ basis set for hydrogen and helium is composed of just one s -function ($1s$). Going further down in the periodic table, the different shells in the atoms from the same row, are considered together, e.g. $2sp$ ($2s$ and $2p$), $3sp$, $4sp$, $3d$ shells, etc. In the case of lithium and beryllium, including only the s orbitals in the minimal basis set yields very poor results, thus p -functions are also added. The minimal basis set is very small and cannot produce quantitatively accurate results, but many useful qualitative observations are obtainable.

The next step beyond the minimal basis set is to include two basis functions for every atomic orbital, producing the Double Zeta (DZ) basis set. Consequently, the DZ basis set has two s -functions for hydrogen and helium ($1s$ and $1s'$), four s -functions ($1s$, $1s'$, $2s$ and $2s'$) and two p -functions ($2p$ and $2p'$) for the second row elements, and six s -functions and four p -functions for third row elements. In cases when the pseudopotential is constructed to include semi-core states (states which are not actual valence states), split-valence basis sets can be used. The name comes from the splitting of the basis function, so the valence states are represented by DZ basis set, and the semi-core states with minimal basis set.

Increasing the number of basis function by one will yield the Triple Zeta (TZ) basis set. As in DZ, the core and valence orbitals in TZ can be split, giving a triple split valence basis set, referred to as TZ. The basis sets next in size are Quadruple Zeta (QZ) and Quintuple Zeta (5Z). Although the basis sets are improving when going to higher zeta (TZ, QZ, 5Z), for better description of the distortion (polarisation) of the atomic orbitals when bonds are formed, basis functions of higher angular momentum should be introduced.

3.2.2 Polarized basis sets

The LCAO basis sets can be further improved by adding polarisation functions, i.e. functions with higher angular momentum, e.g. p -functions for

hydrogen and helium, d -functions for the second row elements etc. To understand why they are called polarisation functions, consider a hydrogen atom placed in an effective electric field. Due to the influence of the field on the electron charge distribution, the previously spherical $1s$ function will become asymmetric, i.e. polarised. When bonded, hydrogen experiences a similar nonuniform electric field, which influence can be described by adding a p -function to the basis set of hydrogen. In general, single or multiple polarisation functions can be added to the multiple zeta basis sets. Adding a single polarisation function to a DZ basis set gives Double Zeta Polarised (DZP) basis set.

3.3 Matrix elements

For practical reasons the pseudopotential approximations and the LCAO basis set, which were discussed in the previous sections, were implemented in the SIESTA DFT method. Thus, the standard Kohn-Sham (KS) Hamiltonian, Eq. 2.16, considering the non-local pseudopotential approximation, can be written as

$$H = T + \sum_i \left[V_i^{\text{local}}(\mathbf{r}) + V_i^{\text{nl}} \right] + V_H(\mathbf{r}) + V_{xc}(\mathbf{r}), \quad (3.11)$$

where i is an atom index, T is the kinetic operator, $V_H(\mathbf{r})$ and $V_{xc}(\mathbf{r})$ are the Hartree and exchange-correlation potentials. The part in the summation, $V_i^{\text{local}}(\mathbf{r}) + V_i^{\text{nl}}$, is the non-local pseudopotential in KB form, V_i^{KB} , see Eq. 3.4, where

$$V_i^{\text{nl}} = \sum_{ilm} \frac{|\delta V_{il} \phi_{ilm}\rangle \langle \phi_{ilm} \delta V_{il}|}{\langle \phi_{ilm} | \delta V_{il} | \phi_{ilm} \rangle}, \quad (3.12)$$

is the non-local (nl) part of the KB pseudopotential, and lm are angular momentum quantum numbers.

In order to eliminate the long-range of V_i^{local} , the V_i^{local} is screened using the potential V_i^{atom} , which is obtained from the atomic electron density ρ_i^{atom} via the Poisson's equation. The resulting potential is called screened neutral-atom (na) potential

$$V_i^{\text{na}} = V_i^{\text{local}} + V_i^{\text{atom}}. \quad (3.13)$$

By using the difference of charge densities, $\delta\rho(\mathbf{r})$

$$\delta\rho(\mathbf{r}) = \rho(\mathbf{r}) - \rho_0(\mathbf{r}), \text{ with } \rho_0(\mathbf{r}) = \sum_i \rho_i^{\text{atom}}(\mathbf{r}), \quad (3.14)$$

where $\rho(\mathbf{r})$ is the self-consistent electron density and $\rho_0(\mathbf{r})$ is the sum over all atomic densities, $\rho_i^{\text{atom}}(\mathbf{r})$, an electrostatic potential $\delta V_H(\mathbf{r})$ is generated, and the Hamiltonian can be written as

$$H = T + \sum_i V_i^{\text{nl}} + \sum_i V_i^{\text{na}}(\mathbf{r}) + \delta V_H(\mathbf{r}) + V_{xc}(\mathbf{r}). \quad (3.15)$$

The matrix elements of the first two terms are expressed as two-center integrals, then calculated in reciprocal space and tabulated as functions of the relative position of the centers. The overlap matrix elements have similar form as the matrix elements of the first two terms, and are calculated in analogous way.

The remaining terms are calculated using real-space grid. The sum of neutral atom potentials are calculated and tabulated as a function of distance to atoms, which further are interpolated at any desired grid point. The last two terms depend on the self-consistent electron density, $\rho(\mathbf{r})$, given by

$$\rho(\mathbf{r}) = \sum_{\mu\nu} \rho_{\mu\nu} \phi_{\mu}(\mathbf{r}) \phi_{\nu}(\mathbf{r}), \quad (3.16)$$

where μ, ν denote the basis orbitals $\phi_{\mu/\nu}$, and $\rho_{\mu\nu}$ is the one-electron density matrix, defined as

$$\rho_{\mu\nu} = \sum_i c_{\mu i} n_i c_{i\nu}, \quad (3.17)$$

where n_i is the occupation of state of the Hamiltonian eigenstate ψ_i , and $c_{i\mu} = \langle \psi_i | \tilde{\phi}_{\mu} \rangle$, with $\tilde{\phi}_{\mu}$ being the dual orbital of ϕ_{μ} , considering $\langle \tilde{\phi}_{\mu} | \phi_{\nu} \rangle = \delta_{\mu,\nu}$. To obtain the last two terms in Eq. 3.15, first the $\rho(\mathbf{r})$ needs to be calculated at a given grid point, by calculating each of the atomic basis orbital at that point. Then $\delta\rho(\mathbf{r})$ is calculated from Eq. 3.14, where ρ_i^{atom} are interpolated from the radial grid. Once $\delta\rho(\mathbf{r})$ is known at every grid point, the $\delta V_H(\mathbf{r})$ can be obtained, by solving the Poisson's equation, and is added to the total grid potential, $V(\mathbf{r}) = V^{\text{na}}(\mathbf{r}) + \delta V_H(\mathbf{r}) + V_{xc}(\mathbf{r})$. Finally, the matrix elements of the total grid potential are calculated at every grid point, and added to the Hamiltonian matrix element.

3.4 Total energy

The electron eigenfunctions, in the LCAO basis, can be obtained by solving the eigenvalue problem for the previously defined KS Hamiltonian. The KS total energy, based on the electron density obtained from Eq. 3.16, can be written as

$$E_{\text{tot}} = \sum_{\mu\nu} \rho_{\mu\nu} H_{\mu\nu} - \frac{1}{2} \int d\mathbf{r} V_H(\mathbf{r}) \rho(\mathbf{r}) + \int d\mathbf{r} (\epsilon_{xc}(\mathbf{r}) - V_{xc}(\mathbf{r})) \rho(\mathbf{r}) + \frac{1}{2} \sum_{ij} \frac{e^2 Z_i Z_j}{|\mathbf{r}_i - \mathbf{r}_j|}, \quad (3.18)$$

where $\epsilon_{xc}(\mathbf{r})\rho(\mathbf{r})$ is the exchange-correlation energy density and $Z_{i/j}$ are the valence pseudoatom charges. The calculations can be made more efficient by avoiding the long-distance interactions of the last term. To do this, a dif-

fuse ion charge ρ_i^{local} , having the same electrostatic potential as V_i^{local} , is constructed as follows

$$\rho_i^{\text{local}}(\mathbf{r}) = -\frac{1}{4\pi e} \nabla^2 V_i^{\text{local}}(\mathbf{r}). \quad (3.19)$$

Then, the last term in Eq. 3.18 may be rewritten as

$$\frac{1}{2} \sum_{ij} \frac{e^2 Z_i Z_j}{|\mathbf{r}_i - \mathbf{r}_j|} = \frac{1}{2} \sum_{ij} \int d\mathbf{r} V_i^{\text{local}}(\mathbf{r}) \rho_j^{\text{local}}(\mathbf{r}) - \sum_i U_i^{\text{local}}, \quad (3.20)$$

where

$$U_i^{\text{local}} = \int d\mathbf{r} V_i^{\text{local}}(r) \rho_i^{\text{local}}(r) 4\pi r^2. \quad (3.21)$$

From V_i^{na} , as defined in Eq. 3.13, ρ_i^{na} can be also defined as $\rho^{\text{na}} = \rho^{\text{local}} + \rho^{\text{atom}}$, and Eq.3.18 can be transformed into

$$\begin{aligned} E_{\text{tot}} = & \sum_{\mu\nu} \rho_{\mu\nu} \left(T_{\mu\nu} + V_{\mu\nu}^{\text{nl}} \right) + \frac{1}{2} \sum_{ij} \int d\mathbf{r} V_i^{\text{na}}(\mathbf{r}) \rho_j^{\text{na}}(\mathbf{r}) - \sum_i U_i^{\text{local}} + \\ & + \int d\mathbf{r} V^{\text{na}}(\mathbf{r}) \delta\rho(\mathbf{r}) + \frac{1}{2} \int d\mathbf{r} \delta V_H(\mathbf{r}) \delta\rho(\mathbf{r}) + \int d\mathbf{r} \varepsilon_{xc}(\mathbf{r}) \rho(\mathbf{r}), \end{aligned} \quad (3.22)$$

where $V^{\text{na}} = \sum_i V_i^{\text{na}}$. The first two terms are calculated by interpolation from initially calculated tables, as in the case of the matrix elements of the Hamiltonian. The third term is calculated from the Eq. 3.21, and the last three terms are calculated using a real space grid, with the grid integrals contain $\delta\rho(\mathbf{r})$, except for the exchange-correlation energy term. Introducing $\delta\rho(\mathbf{r})$ is advantageous because typically it is much smaller than $\rho(\mathbf{r})$, reducing the errors associated with the finite grid spacing.

APPLICATIONS



4. Quantum confinement regime in silicon nanocrystals

For decades silicon has been the main material for variety of photovoltaic and optoelectronic applications. However, the indirect band gap in bulk silicon is a limiting factor in its usability for light-emitting devices, because of the necessity to couple the emission of photon with a phonon. This shortcoming can be overcome by confining the lateral dimensions of silicon, e.g. forming silicon nanocrystals (NCs), which was realised for the first time by Canham [53]. Since then the research of the applicability and the fundamental properties of Si NCs has been rapidly expanding. The improved properties, the biocompatibility, abundance and the easy ways of production, has made the Si NCs one of the leading materials in different applications, from light-emitting diodes (LEDs) [54–57] to lasers [58, 59] and photovoltaics [60–63], as well as biological imaging and labeling [64–68] and biological sensors [69, 70]. The increased number of direct transition in the Si NCs has been argued to be the main reason for the high intensity photoluminescence (PL) of the NCs [38]. The aim of the study detailed in Paper I was to further investigate this claim using parameter free ground-state DFT.

However, the PL properties of the Si NCs are very sensitive to the type of surface capping. The presence of oxygen on the surface can introduce surface traps [39], which significantly decrease the PL intensity and make the energy of the emitted light independent of the NC size [39, 71–74]. Moreover, other impurities, like fluorine, can be present as residues from the specific chemicals used in the synthesis of the NCs. The influence of surface impurities on the optical and electronic properties of Si NCs with various sizes is presented in Paper II. In addition, the easy way of tailoring the Si NCs band gap by changing the NC size, can be utilised in photovoltaic applications by embedding the Si NCs in a host matrix. To increase the efficiency of the light conversion and have faster transport of charge carriers, a host matrix that facilitates spatial separation of the charge carriers [75] and has smaller band gap [76] is desirable. The widely used host matrices for Si NCs, SiO_2 , Al_2O_3 and Si_3N_4 , do not fulfil these requirements, thus the attention has turned to using SiC as a host matrix [77–79]. Having this in mind we studied the band alignment and the leakage of charge densities in Si NCs embedded in SiC (Paper III).

In this chapter, the size-dependence of the HOMO-LUMO and optical absorption gap of hydrogenated Si NCs is going to be shown. In addition, a detailed study of the character of the band gap in these NCs, based on inspecting the changes in the highest occupied (HOMO) and the lowest occupied

(LUMO) state wavefunctions (WFs), is going to be demonstrated. This study is expanded by examining the influence of single impurities on the surface of the hydrogenated Si NCs on their electronic and optical properties. Moreover, to have a better understanding of the effect of the surface impurities, the character of the states around the gap were studied. Finally, the influence of the interface on the band alignment in Si NCs embedded in SiC, and the dependence of the charge densities leakage on the distance between neighbouring Si NCs are going to be discussed.

4.1 Hydrogenated silicon nanocrystals

Despite the numerous experimental and theoretical studies regarding the Si NCs, a fundamental understanding of the origin of the PL is still a subject of a debate. The widely accepted reason for this phenomenon, is the increased direct band gap character of transitions with decreasing NC size (See Sec. 5.1 for more details). Based on tight-binding calculations, Trani et al. [38] argued that the increased localisation of the highest occupied (HOMO) and lowest unoccupied (LUMO) molecular orbital level around the Γ point in \mathbf{k} space with decreasing NC size, is a clear indication of an increased direct band gap character. In addition, Weissker et al. [80] related the tail in the oscillator strength in larger NCs, calculated using DFT-LDA, with the increased bulk-like properties.

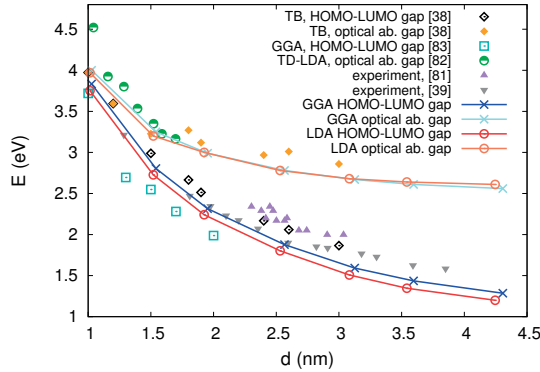


Figure 4.1. Comparison of HOMO-LUMO and optical absorption gap for Si NCs for various diameters, and different exchange correlation potentials, LDA and GGA, compared with data from published literature [38, 39, 81–83]. Results obtained in this work are shown in red (LDA) and blue (GGA), using dark (light) colour for HOMO-LUMO (optical absorption) gaps, respectively.

To investigate the changes in the character of the band gap in Si NC we considered NCs with several different diameters, from 1.0 to 4.2 nm. Ground-state DFT calculations were performed, employing local-density approxima-

tion (LDA) and generalised gradient approximation (GGA). Single- ζ polarised (SZP) and double- ζ (DZ) basis set were used for Si and H, respectively. Each of the studied structures was relaxed until all forces acting on each atom is lower than 0.04 eV/Å. For each of the studied structures, the HOMO-LUMO gaps and the optical absorption gaps were calculated. Shown on Fig. 4.1 are the calculated HOMO-LUMO gaps and the optical absorption gaps, compared with experimental band gaps [39, 81], and band gaps from other theoretical studies [38, 82, 83]. As expected from quantum confinement effect, both gaps, HOMO-LUMO and optical absorption gap, grow with decreasing NC size, eventually becoming very close to each other. This apparent merging of both gaps can be viewed as transition from intrinsic indirect nature of the band gap, to direct band gap in the smallest NC. It is also interesting to notice that the HOMO-LUMO gaps are very similar to the optical gaps observed in experiments. Although the higher-order effects are neglected in the present DFT results, it is shown that the cancellation of quasi-particle and excitonic effects [80, 84] contributes to the similarity of the theoretical and experimental results.

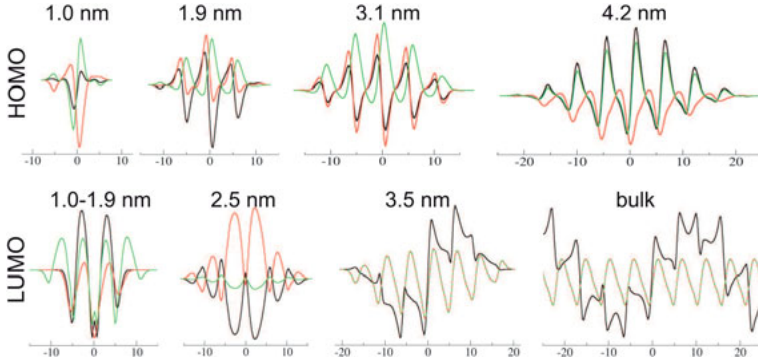


Figure 4.2. HOMO and LUMO WFs of NCs of various sizes. The upper row shows HOMO WFs on a line passing through NC center parallel to lattice axes, for NCs of sizes 1.0, 1.9, 3.1, and 4.2 nm, respectively. The lower row show non-degenerate LUMO WFs of 1.0, 1.5, and 1.9 nm NCs, respectively, then the three perpendicular cuts of LUMO for the 2.5 nm NC, the triple-degenerated LUMO of the 3.5 nm NC, and three perpendicular cuts of the bulk LUMO WF.

To facilitate this change in the HOMO-LUMO and optical absorption gap, some features of the HOMO and LUMO states are most probably changing. The HOMO state, for example, is triply degenerate for the whole range of NC size, as in non-relativistic description of bulk Si. However, the LUMO state changes from non-degenerate in NC smaller than 1.9 nm, to double degenerate in the 2.5 nm NC, and is triply degenerate for the NCs bigger than 3.1 nm. The similarity in the HOMO state and the changes in the LUMO state with changes in the NC size, can be easily observed by inspecting the spatial characteristics of the WFs. One way to examine this is to plot the HOMO and LUMO WFs

on a line passing along the lattice axes, see Fig. 4.2. The HOMO state is triply degenerate, with a predominantly p character, for which the three WFs have similar spatial characteristic, displaying an oscillatory behaviour modulated with Bessel function type [85], decaying at the NC's edges.

The LUMO state of the NC smaller than 1.9 nm is non-degenerate, and the LUMO WF has an elliptical s symmetry. The 2.5 nm NC has a double-degenerate LUMO state, which has a similar spatial distribution of the WFs as the LUMO WF in the smaller NCs, but with an elliptical distorted s symmetry. One of the WFs appear compressed along z direction and the other one elongated along z , with the WFs along the x , y and z are almost identical up to a sign and a scaling factor. On the other hand, the LUMO WFs of the NCs larger than 3.1 nm have p -type symmetry, with a different spatial characteristic than the HOMO WFs. Moreover, the LUMO WF of the 3.5 nm NC shows a clear similarity with the bulk LUMO WF for \mathbf{k} point $\frac{2\pi}{a}(0.83, 0, 0)$.

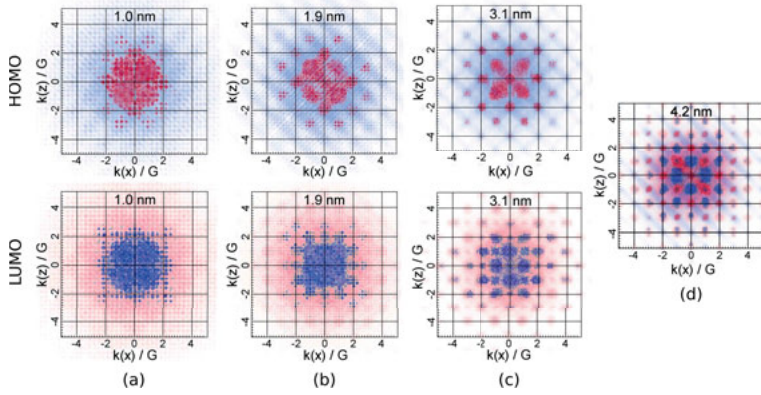


Figure 4.3. Fourier transform (FT) of the HOMO (upper row) and LUMO (lower row) WF of Si NCs of the following sizes: (a) 1.0 nm, (b) 1.9 nm, and (c) 3.1 nm. (d) Overlap between FT of the HOMO and LUMO WFs for the 4.2 nm NC. The 3D FT was projected on the $x-z$ plane. For clarity of the graphical representation, the colour range, blue to red for the HOMO WF and opposite, red to blue, for the LUMO WF, maps positive values of the real part of FT, within a fixed range for all sizes (in arbitrary units). The $\mathbf{k}(x)$ and $\mathbf{k}(z)$ are scaled by a reciprocal vector \mathbf{G} of size $\frac{2\pi}{a}$.

Further understanding of the changes in the HOMO and LUMO WFs, and their influence on the \mathbf{k} selection rule between the WFs, can be better explained in Fourier space. In Fig. 4.3 are shown the size-dependence of the Fourier transform (FT) of the HOMO and LUMO WFs. For the smallest NCs, the maxima of the Fourier components of the HOMO and LUMO WF display an increased overlap, indicating no apparent periodicity of the WF in the NC. With increasing NC size, the maxima of the Fourier components are becoming sharper and isolated, suggesting an increased periodicity, as in periodic solid. Comparing the position of the Fourier components, it is evident that with increasing NC size the overlap between the components coming from the

HOMO and the LUMO WF is decreasing, eventually the components appear at different \mathbf{k} points. The components of the HOMO WF form arrangement similar to the one in bulk Si, with the components appearing at odd or even \mathbf{k} points. However, with increasing NC size, the components of the LUMO WF appear at odd-even combination of \mathbf{k} points, shifted towards the origin. This can be understood as a increasing band-like character of the LUMO WF, corresponding to the \mathbf{k} point $\frac{2\pi}{a}(0.83, 0, 0)$. Moreover, the HOMO and LUMO WF display almost exclusive Fourier components, as in bulk Si, corresponding to different \mathbf{k} points in the Brillouin zone.

4.2 Influence of the surface impurities

Although the Si NCs can emit bright intensity light in narrow spectral range, their PL can be greatly affected by the surface impurities. It has been shown that after leaving hydrogenated Si NCs with different sizes in ambient conditions the PL peak does not exhibit blue shift with decreasing NC size, and their PL intensity is reduced [39, 71, 72]. These observations have been assigned to the surface oxidation, especially to the localisation of mid-gap states, originating from the Si=O species on the surface [39]. In addition, the synthesis of the Si NCs can leave various impurities on the surface of the NCs, which can further influence the PL properties of the NCs. Therefore, it is important to provide understanding of the influence of various surface impurities on the electronic and optical properties of Si NCs with different sizes, based on parameter-free DFT calculations.

The main quantity that can be calculated from DFT, and gives direct unambiguous information about the trends in the position of the PL peak, is the band gap. Thus, obtaining information regarding the changes in the band gap, in NCs with different impurities, gives an initial insight into the effect of the surface impurities. Considering that the surface impurities can form different types of bonds, e.g. single or double-bond, it is also important to examine the influence of bonding types. Therefore, for the purpose of the study we considered single-bonded (SB) impurities: $-\text{CH}_3$, $-\text{F}$, $-\text{Cl}$, $-\text{OH}$ and bridged oxygen ($-\text{O}-$), and double-bonded impurities: $=\text{O}$ and $=\text{S}$. Details of the DFT calculations are presented in the previous Sec. 4.1. Shown on Fig. 4.4 are the calculated HOMO-LUMO and optical absorption gaps for the Si NCs with surface impurities.

Evidently, the SB and DB impurities have rather different influence on the HOMO-LUMO and optical absorption gap. In the NCs with SB impurity, both gaps closely follow the gaps in the hydrogenated Si NCs for the respective NC size. The biggest difference occurs for the smallest NC, 1.0 nm, where the NCs with SB impurity have slightly lower gaps. The gaps in the NCs with $-\text{O}-$ also closely follow the gaps in the NCs with other SB impurity, but the $-\text{O}-$ impurity induces somewhat larger change in the gaps, which can be seen

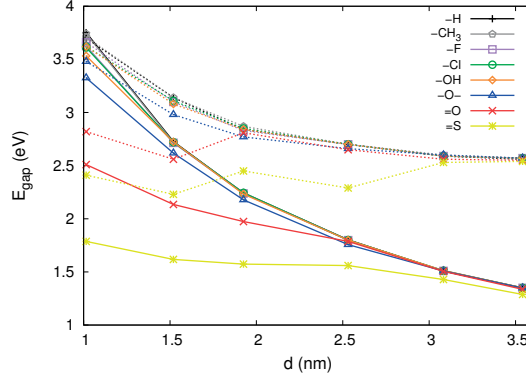


Figure 4.4. HOMO-LUMO gaps (solid lines) and optical absorption gaps (dotted lines) for Si NCs with different impurities. The gaps of NCs with $-\text{CH}_3$, $-\text{F}$, $-\text{Cl}$, $-\text{OH}$, $-\text{O}-$, $=\text{O}$ and $=\text{S}$ impurities are shown in grey, purple, green, orange, blue, red and yellow, respectively. The gaps of the fully hydrogenated NC ($-\text{H}$) are shown in black.

in NCs with size up to 2.5 nm. On the other hand, the DB impurities induce very large change in the HOMO-LUMO gaps, compared to the hydrogenated Si NCs, even for NCs larger than 2.5 nm. The optical absorption gaps in the NCs with DB impurities smaller than 2.5 nm does not follow a similar size-dependent trend as the hydrogenated Si NCs. However, the difference between the HOMO-LUMO and optical absorption gap in the NCs with DB impurities is increasing with growing NC size, as in the hydrogenated Si NCs.

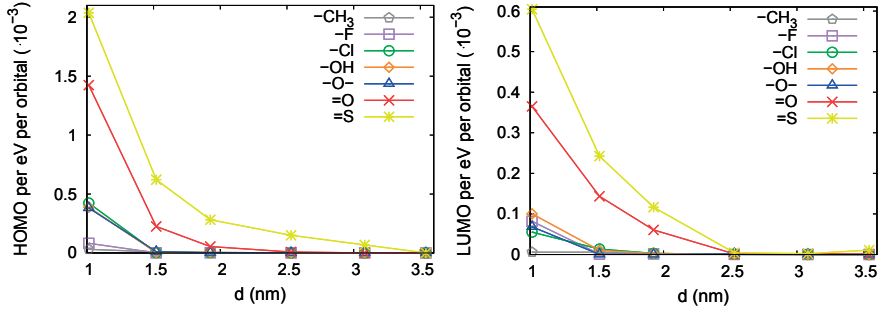


Figure 4.5. Integral over the HOMO and LUMO PDOS of the NCs with surface impurities as a function of the size of the NCs. The PDOS integrals of the NCs with $-\text{CH}_3$, $-\text{F}$, $-\text{Cl}$, $-\text{OH}$, $-\text{O}-$, $=\text{O}$ and $=\text{S}$ impurities are shown in grey, purple, green, orange, blue, red and yellow, respectively.

Further understanding of the influence of the surface impurities on both HOMO-LUMO and optical absorption gaps can be gained by investigating the changes in the HOMO and LUMO states induced by the surface impurities. The most basic information can be obtained from the contribution from the impurity atom to the total density of states (DOS), calculated from the pro-

jected DOS (PDOS), see Fig. 4.5. It is evident that the contribution from the DB impurities to both HOMO and LUMO states is significantly larger than the contribution from the SB impurities. Moreover, compared to the SB impurities, which have significant contribution only for the 1.0 nm NC, the DB impurities contribute to the HOMO and LUMO states of NCs with larger size, up to 2.5 nm.

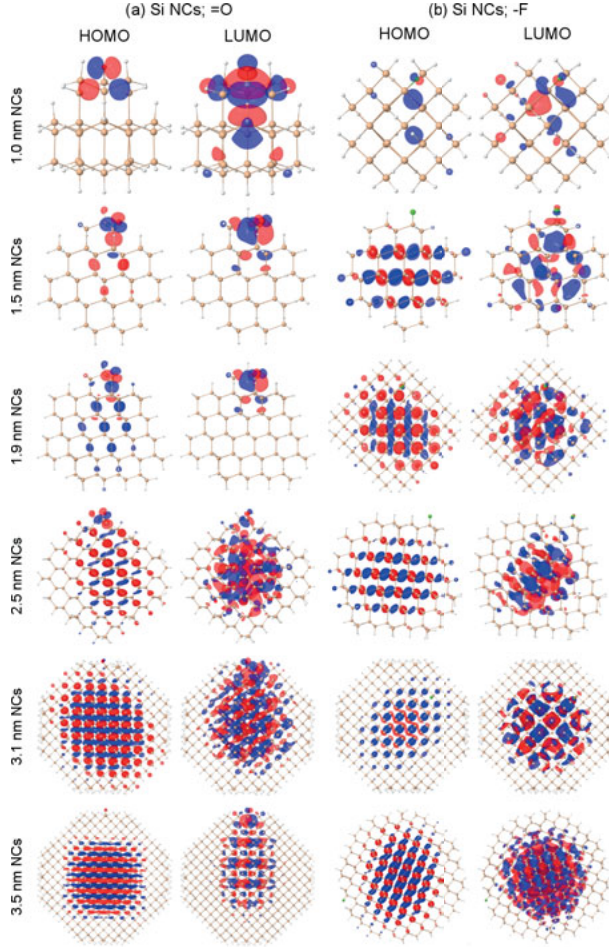


Figure 4.6. Size-dependence of the HOMO and LUMO wavefunctions for Si NCs with: (a) =O; and (b) -F impurity. The O, F, Si and H atoms are shown in red, green, tan and white, respectively.

This difference in the contribution can be illustrated in more details by calculating the HOMO and LUMO WFs, see Fig. 4.6. As indicated by the PDOS, the HOMO and LUMO WFs of the smallest NCs, 1.0 nm, are mainly localised around the impurity atom, regardless of the type of bonding. With increasing NC size, the localisation of the WF around the -F impurity is significantly de-

ceased, and it is negligible even for the 1.5 nm NC. In the case of the =O impurity, there is substantial localisation of the HOMO and LUMO WFs around the O atom for NCs up to 2.5 nm. It is also interesting to notice that the localisation around the =O impurity of the LUMO WF is greater compared to the localisation of the HOMO WF, especially for larger NCs.

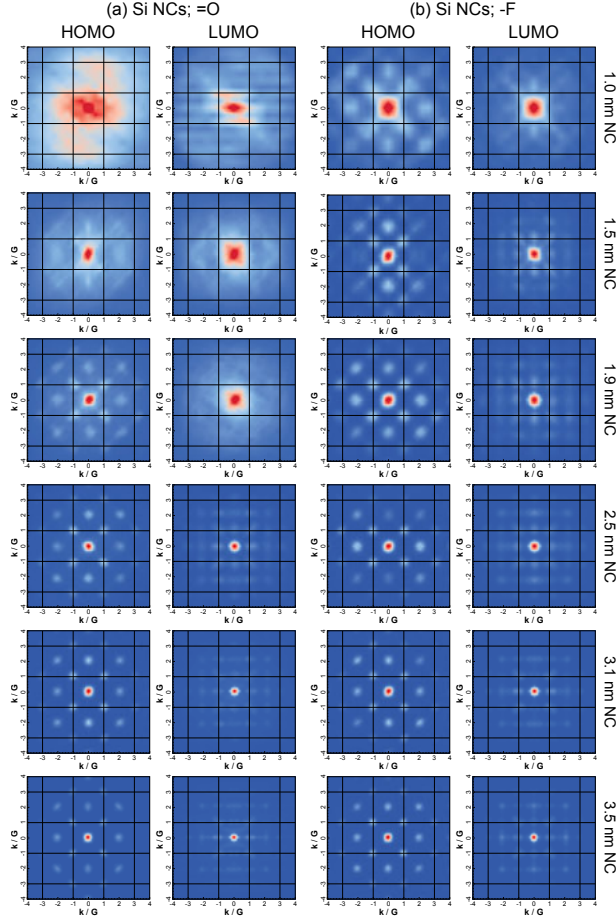


Figure 4.7. Fourier transform (FT) of the HOMO and LUMO charge density of Si NCs with: (a) =O; and (b) -F impurity, as a function of the size of the NCs. The FT is an average of the projections on the $x-y$, $x-z$ and $y-z$ planes. The red colour maps the highest values and the blue colour the lowest value of the charge densities within a fixed range for all sizes (in arbitrary units). The \mathbf{k} is scaled by the reciprocal vector \mathbf{G} of size $\frac{2\pi}{a}$.

An additional insight and a complementary point of view of the localisation and the symmetry of the HOMO and LUMO states can be obtained by calculating the Fourier transform (FT) of the charge densities. Shown on Fig. 4.7 is the average of the projections on $x-y$, $x-z$ and $y-z$ planes of the FT of the

HOMO and LUMO charge densities. The dependence of the FT of the charge densities on the size of the NCs naturally follow similar pattern as the WFs in real space. The FT of both, HOMO and LUMO charge densities of the NC with =O smaller than 1.9 nm, show an increased delocalisation, indicating an increased localisation and no apparent periodicity in real space. With increasing NC size, the spots in the FT of the charge densities become more distinct, suggesting an increased delocalisation in the core of the NC, becoming similar to the one in hydrogenated Si NCs (see Fig. 4.3). For the NCs with –F impurity, the FT of the HOMO and LUMO charge densities of the smallest NC show increased delocalisation, with the periodicity becoming apparent as the size of the NC increases.

4.3 Embedded silicon nanocrystals

The improved properties of silicon upon formation of NCs are also applicable in photovoltaic devices, as part of the third generation solar cells. However, to utilise these properties, the Si NCs should be embedded in a host matrix that serves as a charge carrier. In addition, it is preferable the Si NCs and the host matrix to form type-II band alignment, where the valence band maximum (VBM) and conduction band minimum (CBM) of the whole system are in the different materials. This type of band alignment will provide spatial separation of the electron and hole, thus reducing the probability of exciton recombination. Moreover, in this way the charge carrier can be easily transported in the host matrix, increasing the efficiency of light conversion [75]. It is also preferable the host matrix to have a smaller band gap, which can facilitate faster transport of the charge carriers [76]. One host matrix which is expected to possess significantly better properties than the usually used SiO_2 and Si_3N_4 , is amorphous SiC [77–79].

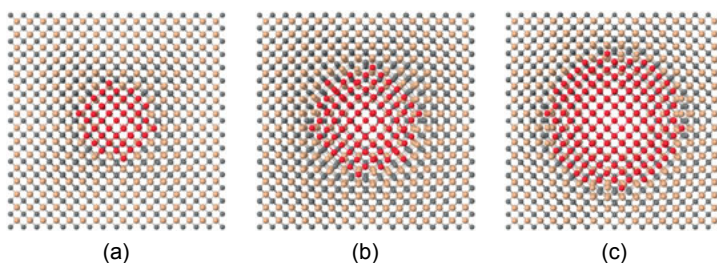


Figure 4.8. Balls-and-sticks model of: (a) 1.5 nm; (b) 2.0 nm; and (c) 2.5 nm Si NCs, embedded in $8 \times 8 \times 8$ SiC. The Si atoms from the NC are shown in red, and the Si and C atoms from the matrix are shown in tan and grey, respectively.

To have an insight into the electronic properties of a closely related system, we focused the study on Si NCs embedded in crystalline SiC. SiC with zinc-blende structure was used as a host matrix, made of $6 \times 6 \times 6$, $7 \times 7 \times 7$ and $8 \times 8 \times 8$

unit cells, and Si NC with 1.5, 2.0 and 2.5 nm in diameter (see Fig. 4.8). We made four distinct models, termed model A, B, C and D (see Paper III for more details), where we vary the interface between the Si NC and the matrix. However, in this section the focus will be on the models A, C and D. The former being the representatives of a perfect bonding between Si NC and the matrix, and latter two a case when hydrogenated Si NC or NC with surface impurities, oxygen in this case, is inserted in the matrix. The electronic properties of both models were calculated using DFT, with LDA and SZP basis set for Si, O and C, and DZ for H. In the DOS of model C and D there is a clearly defined band gap was observed. However, in the same interval around the Fermi level in model A and B impurity states were noticeable.

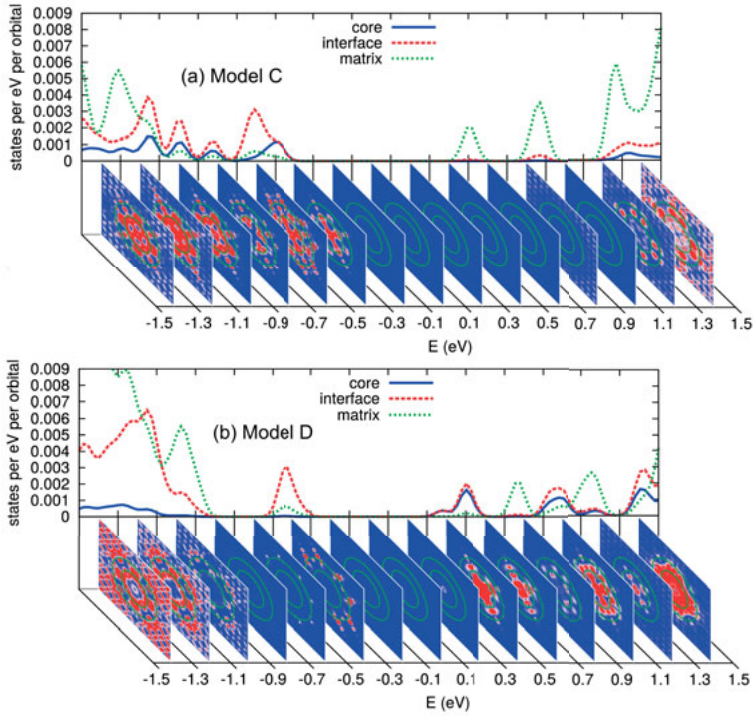


Figure 4.9. PDOS of: (a) model C; and (b) model D, and the corresponding projections of the charge densities on the $x-y$ plane. The PDOS of the core, interface and matrix region are shown in blue, red and green, respectively.

To have an understanding where do these impurity states come from, and to have an insight into the band alignment in this complex system, we calculated the projected DOS (PDOS). Closer inspection of the PDOS of model A and B revealed that the impurity states are mainly localised at the interface between the NC and the matrix. Also noticeable from the PDOS was that the band alignment in models A, B and C is of type-II, with the VBM being in the NC and the CBM in the host matrix (see Fig. 4.9(a)). Interestingly, there is

an interchange in the type-II band alignment in model D, where the VBM is now in the matrix, and the CBM in the NC (see Fig. 4.9(b)). Having in mind that model D was made from model C by replacing some H atoms with O, this switching of the band alignment shows that the band alignment can be modified depending on the desired properties of the material, just by introducing particular impurities at the interface of the NC and the matrix.

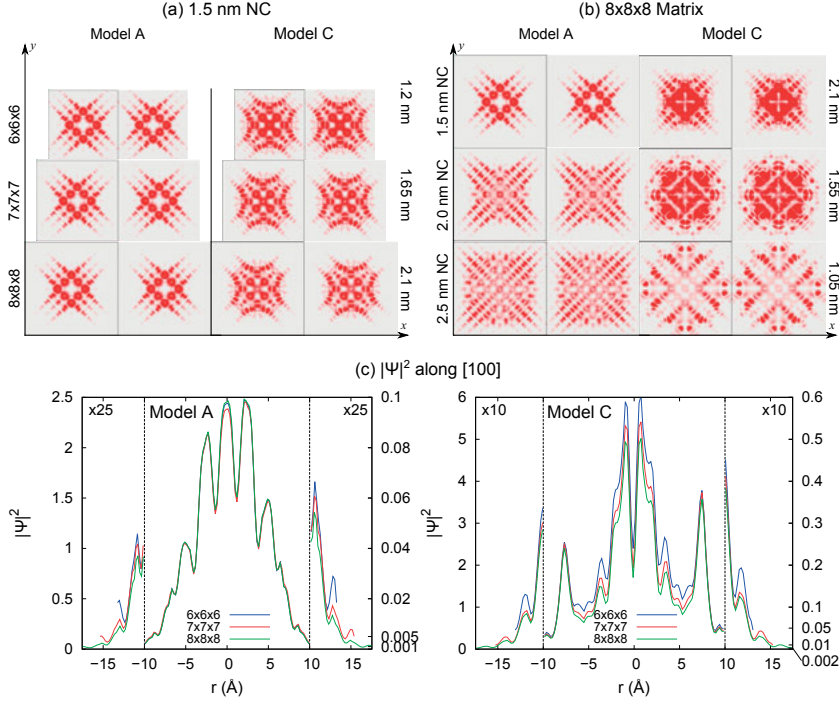


Figure 4.10. Projections of the charge densities on the $x - y$ plane, for two adjacent cells of models with: (a) 1.5 nm NC in different size matrix; and (b) 8x8x8 matrix with NCs with different size. The surface-to-surface distances between NCs in neighbouring cells are given on the right side of the each panel. The energy intervals, for which states the charge densities are calculated, of model A and model C are -0.5 – -0.3 eV and -0.9 – -0.7 eV, respectively. (c) Average charge densities in a series of {100} planes along [100] direction, of models A (left part) and C (right part) with 1.5 nm NC, corresponding to the same charge densities shown in (a).

Furthermore, of great interest for photovoltaic applications is also the possible leakage of states between the neighbouring NCs. Thus, we focused on the leakage of the charge densities of the states that are mostly localised in the core of the NC. Shown in Fig. 4.10 are the $x - y$ projection of the charge densities of two adjacent cells of model A and C, as a function of the distance between the Si NCs. Two possible instances are considered: (a) changing the NC distance by keeping the NC size fixed while changing the matrix size, and (b) changing the size of the NCs, in a host matrix with fixed size. With increas-

ing matrix size, the spatial distribution of the charge densities of a particular model is rather unchanged. However, the leakage of the charge densities in the neighbouring cells is increasing with narrowing distance between the NCs, being the largest when the NC–NC distance is the shortest, ~ 1.2 nm. This can be clearly seen from Fig. 4.10(c), where the charge density at the border of two cells is ~ 0.8 % from the maximum. The leakage is significantly smaller when the NC–NC distance ~ 1.65 nm, and is almost absent for the largest NC–NC distance, ~ 2.1 nm, being smaller than ~ 0.05 %. Similarly, when the size of the NC is increasing, in host matrix with same size, the leakage of the charge densities is growing with growing NC size, i.e. decreasing NC distance. The leakage of the states is largest for the biggest NC, where significant overlap between the charge densities of the neighbouring cells is observed, with the charge density at the border of two cells being more than 2 % of the maximum. Moreover, in the systems with similar NC–NC distance, ~ 1.65 and ~ 1.55 nm (8x8x8 matrix with 2.0 nm NC and 7x7x7 matrix with 1.5 nm NC), the leakage of the states is very similar, indicating that the size of the NC does not affect the leakage of the charge densities.

5. Semiconductor nanocrystals – significance of the interface and the capping of the surface

The semiconductor nanocrystals (NCs) are mediators between the bulk materials and isolated molecules, having the usefulness of the crystalline materials and displaying quantised electronic states as in isolated molecules. The quantisation of the electronic states arises from the spatial confinement of the bulk delocalised states, which also influences the band gap. With increasing confinement, i.e. reducing nanocrystal size, the band gap exhibits blue shift, allowing for the electronic and optical properties to be tailored according to the specific needs, which makes the semiconductor NCs very desirable materials in various applications. Another important benefit from confining the dimensions is the increase in the photoluminescence (PL) quantum efficiency (QE) of the semiconductor, which even further increases the usability of the semiconductor NCs. The QE can be defined as the ratio between the amount of photons emitted, N_e , and the amount of photons absorbed N_a , i.e.:

$$QE = \frac{N_e}{N_a}, \quad (5.1)$$

In a perfect nanocrystal, where every recombination of an excited electron with hole is coupled with photon emission, the QE would always be 100 %. However, the synthesised NCs might exhibit many defects and dislocations, and together with the increased surface area can facilitate other recombination processes that can decrease the QE. For example, in non-radiative and Auger processes the absorbed energy is not emitted, but it is merely lost in a different form. These processes can also reduce the PL intensity, broaden the PL peak, and facilitate random switching between PL on and off states, i.e. blinking.

Furthermore, the improved methods of producing semiconductor NCs with uniform size and very high quality, together with the NCs' increased PL efficiency in narrow spectral range, has turned the attention to these NCs as one of the essential materials in many aspects of science and technology. Their applicability ranges from devices where high-intensity light is required, e.g. LEDs [86–90] and lasers [91], to using their absorption properties in photovoltaic materials [75, 92, 93], as well as biological sensors and biological labelling [94, 95]. The usefulness of the semiconductor NCs comes mainly from the easiness of influencing the band gap, allowing the PL to be shifted

to particular spectral range just by manipulating the NCs size. This versatility has made the semiconductor NCs especially attractive materials in devices where tunability of the PL is necessary.

As in the case of the Si NCs, the PL in any other semiconductor NC can be significantly influenced by the surface impurities. To suppress the addition of impurities, the surface of the NCs is capped. In the case of compound semiconductor NCs, II-VI semiconductor NCs for example, there are differently charged anionic and cationic sites on the surface. The passivation of their surface with organic molecules has been proven difficult, because of the difficulty to simultaneously passivate both cationic and anionic sites. Therefore, to suppress the dangling bonds that might appear and to fully passivate the surface, the II-VI semiconductor NCs are overgrown with another semiconductor, acting as a capping shell, making core-shell NCs. Of special interest are the NCs with type-I band alignment, where both the electron and hole are confined in the core of the NC, which improves the PL properties of the core material and further increase their PL intensity. Core-shell NCs which are shown to exhibit these properties, increasing their usability in wide variety of applications, are the CdSe/CdS [96–102] and CdS/ZnS [103–105].

The properties of the core-shell NCs can be further adapted to the specific needs by engineering the interface between the core and the shell, or by changing the core type. It has been shown that by introducing alloyed interface between CdSe core and CdS shell, the Auger recombination can be suppressed [99, 101], compared to the same size NCs with sharp interface. Also, in CdSe/CdS core-shell NCs, introducing graded core can increase the quantum efficiency of the NCs [97]. The aim of our research was to understand how the different structural models influence the properties of CdSe/CdS and CdS/ZnS core-shell NCs, and compare the properties of these two different types of core-shell NCs. We also focus on the changes in the properties of these core-shell NCs with changes in the size of the NC and the core/shell ratio. The results are presented in detail in Papers IV and V.

On the other hand, in single element semiconductor NCs, for example Si NCs, the situation is different. Having only one type of atom, makes the surface of the NCs uniformly charged, and thus easier to be passivated. Capping the surface of Si NCs with organic ligands suppresses the oxidation of the surface, and increases the radiative transition rates [106–110], making the radiative rates of these NCs comparable to the ones in direct semiconductor NCs. However, the energy and the intensity of the emitted light can be influenced by the organic ligand used to passivate the surface [107]. The increased PL of the Si NCs upon capping the surface with organic ligands, and comparison between two different types of ligands, was the main topic of the study presented in Paper VI.

Before giving further details regarding the results from the different studies of semiconductor NCs, a short descriptions of the various recombination processes that can occur in semiconductor nanocrystals are presented. Af-

terwards, the influence of the different structural models on the properties of CdSe/CdS and CdS/ZnS core-shell nanocrystals are going to be presented, as well as direct comparison between these two different types of core-shell nanocrystals. In the subsequent section, the effect of the surface capping on the properties of Si nanocrystals is going to be discussed.

5.1 Recombination processes in semiconductor nanocrystals

5.1.1 Radiative recombination

Any recombination process is preceded by an absorption of energy, during which an electron is excited from the valence band to the conduction band, creating an electron hole (e-h) pair. Once the e-h pair is formed, both electron and hole reach their respective conduction and valence band edges in matter of ps, due to the coupling with lattice vibrations. The bound state in which the electron and the hole are attracted by electrostatic Coulomb force, forming a neutral quasi-particle, is called exciton. The process of electron and hole annihilation (recombination) accompanied by a generation of photon is termed radiative recombination. The emitted photon has energy equal to the energy difference between the eigenstates of the electron and the hole. This is schematically represented in Fig. 5.1.

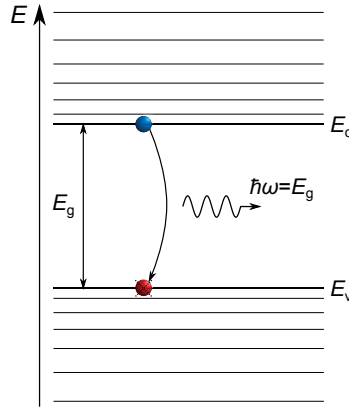


Figure 5.1. Schematic representation of radiative recombination process. The electron and hole are shown in blue and red balls, respectively.

In direct band gap semiconductors, such as CdSe, CdS and ZnS discussed in this Chapter, both conduction band minimum (CBM) and valence band maximum (VBM) are at the Γ point ($\mathbf{k} = 0$). Hence, the transitions between the CBM and VBM are happening at the same \mathbf{k} point, which gives the term direct transitions. In a radiative recombination event, the energy of the emitted photon equals the band gap energy, $\hbar\omega = E_g$. On the other hand, the interband

transition in indirect band gap semiconductors, e.g. Si, occurs between electron with non-zero momentum and a hole having a momentum $\mathbf{k} = 0$. These transition are called indirect transitions. For any recombination to take place the momentum must be conserved, which is done by coupling the electron with a phonon, making this recombination very unlikely process. The direct and indirect transitions are schematically shown in Fig. 5.2(a) and (b), respectively.

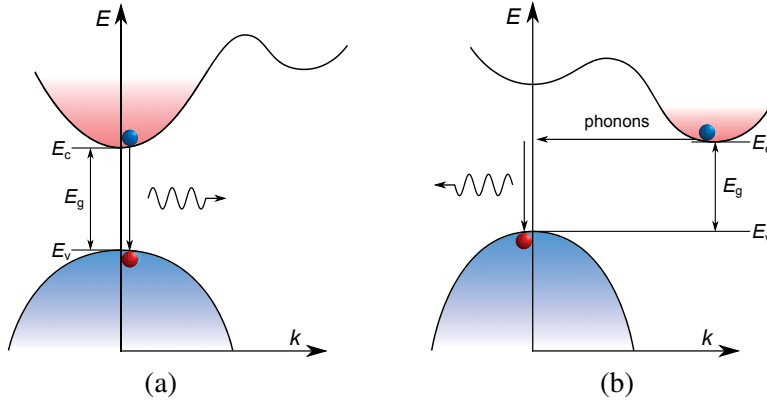


Figure 5.2. Schematic representation of radiative recombination in: (a) direct semiconductors; and (b) indirect semiconductors. The valence band and the conduction band are shown in red and blue, respectively. The electrons and holes are respectively shown in blue and red balls.

As previously said, for any radiative recombination to occur, a given number of electrons must be excited from the valence band to the conduction band. Consider that in the conduction band state i at a given time t the number of excited electrons is $N(t)$, the rate at which the N decays is given by

$$\frac{\partial N}{\partial t} = -\Gamma_{i,j}N(t). \quad (5.2)$$

The solution gives

$$N(t) = N(0) \exp(-\Gamma_{i,j}t), \quad (5.3)$$

where $N(0)$ is the initial number of electron in the excited state, and $\Gamma_{i,j}$ is the radiative transition rate between the initial conduction band state, $|i\rangle$, and the final valence band state, $|j\rangle$. The time after which the number of excited electron is decreased by $1/e$ is specified as radiative lifetime, τ . In the present study, the radiative lifetimes are evaluated using the dipole transition matrix element, $\langle i|\mathbf{r}|j\rangle$, employing the equation derived from the Fermi's golden rule [111]:

$$\frac{1}{\tau} = \frac{4e^2\omega_{i,j}^3}{3\hbar c^3} n |\langle i|\mathbf{r}|j\rangle|^2, \quad (5.4)$$

where $\omega_{i,j}$ is the emission frequency between the initial and final state, \hbar is the reduced Planck constant, and c is the speed of light in vacuum. The refractive index of the system, n , is evaluated from the calculated dielectric tensor. As mentioned previously, the attraction between the electron and hole in the excitonic state is dependent on the Coulomb force. Therefore, valuable information concerning the stability of the exciton can be obtained from the electron-hole (e-h) Coulomb interaction energy (E_b). The e-h E_b was calculated employing the equation proposed by Wang *et al.* [112]:

$$E_b = \int \int \frac{|\psi_e(\mathbf{r}_1)|^2 |\psi_h(\mathbf{r}_2)|^2}{\epsilon(\mathbf{r}_1 - \mathbf{r}_2) |\mathbf{r}_1 - \mathbf{r}_2|} d\mathbf{r}_1 d\mathbf{r}_2, \quad (5.5)$$

where ψ_e and ψ_h are the electron and hole wavefunctions, respectively, and $\epsilon(\mathbf{r}_1 - \mathbf{r}_2)$ is the screening dielectric constant.

5.1.2 Non-radiative recombination

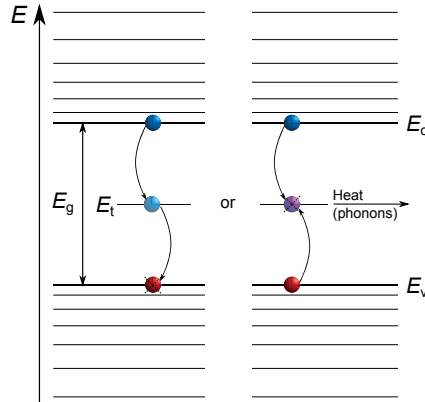


Figure 5.3. Schematic representation of non-radiative (trap assisted) recombination processes. The electrons and holes are shown in blue and red balls, respectively.

As the name suggests, during a non-radiative recombination, also known as trap assisted recombination, no photons are emitted, while the energy is dissipated in the lattice, in form of phonons. The recombination of the electron and hole occurs through localised state (trap state) in the band gap, during which the electron and hole can annihilate at the trap state, or the electron can relax to the valence band in two-step recombination. These two processes are schematically shown in Fig. 5.3. In very few cases when trap states are involved in the annihilation of the electron-hole pair, photon with low energy might be emitted, which significantly broadens the PL peak. The allowed energy levels (E_t) in otherwise forbidden gap can arise due to impurities and defects in the semiconductor. Especially the surface, which can be seen as a serious defect, can introduce great number of allowed states in the band

gap. Because the trap state can account for the difference in the momentum of the electron and the hole, the non-radiative recombination is the primary recombination process in indirect band gap semiconductors.

5.1.3 Auger recombination

Unlike the previous two recombination processes, where only two particles are involved, the Auger recombination is three particle process. In the Auger recombination, the excess energy of the electron-hole recombination is given to a third carrier, an electron or a hole. The excess energy of the third carrier is then lost by exciting phonons. This is schematically shown in Fig. 5.4(a) and (b). The Auger recombination is a very fast process, in the order of few nanoseconds for small nanocrystals, which can dominate over the radiative recombination. In particular, the lowering of the photoluminescence efficiency of nanocrystals, the PL blinking and PL degradation have been credited to the Auger recombination.

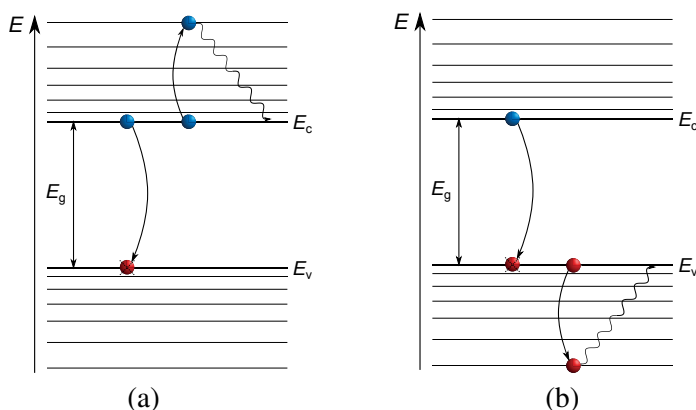


Figure 5.4. Schematic representation of Auger recombination, where the excess energy is given to: (a) electron; or (b) hole. The electrons and hole are shown in blue and red balls.

5.2 CdSe/CdS core-shell NCs

Since it was demonstrated that the PL properties of CdSe NCs can be significantly improved upon capping the surface with shell of CdS, i.e. making CdSe/CdS core-shell NCs, the interest in CdSe/CdS NCs has been rapidly increasing. One of the main reasons for the enhanced PL of the CdSe/CdS NCs is the formation of type-I band alignment between the core and the shell region, with the hole exhibiting increased confinement in the core compared to the electron. The increased confinement of the hole in the core and the differential localisation of the hole and the electron, give the CdSe/CdS NCs distinct

properties, with high QE and photostability. Furthermore, the PL properties can be influenced by changes in the interface between the core and the shell, or changes in the core type. In the study presented in Paper IV, our interest was to understand the changes in the PL properties of the CdSe/CdS NCs with different structural models, by investigating the spatial distribution of the highest occupied (HOMO) and lowest unoccupied (LUMO) eigenstate wavefunction (WF) and the electron-hole Coulomb interaction energies.

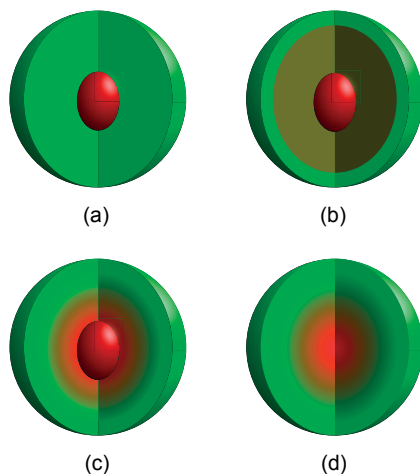


Figure 5.5. Schematic representation of the four structural models: (a) pure core; (b) alloyed interface; (c) graded interface; and (d) graded core.

We considered structures with four different structural models (see Fig. 5.5): pure core, alloyed interface, graded interface, and graded core, and two different sizes, 2.4 nm and 3.1 nm in diameter. Each of the structures with different structural models has the same core size, 0.8 nm, with the 3.1 nm structure having two larger core sizes, 1.55 and 2.2 nm. The surface of the structures was passivated with pseudohydrogen, which has fractional charge of $1.5e$ and $0.5e$, allowing for compensation of the cationic and anionic sites at the surface, respectively. The calculations were performed using LDA, with DZP basis set for each of the atom species, and allowing the forces on each atom to get lower than 0.04 eV/\AA when relaxing the structures. We observed that the density of states (DOS) and the absorption indices depend rather weakly on the interface and core type. Similarly, the band gaps, calculated as energy difference between the LUMO and the HOMO, of the NCs with different structural model are very close to each other, as shown in Fig. 5.6. The most noticeable change is the decrease of the band gaps with increasing NC size, which is a consequence of the quantum confinement effect.

Although the band gap gives an information regarding the energy of the emitted light, to have an insight into the PL properties of the CdSe/CdS NCs one should further study the confinement of the HOMO and LUMO WFs.

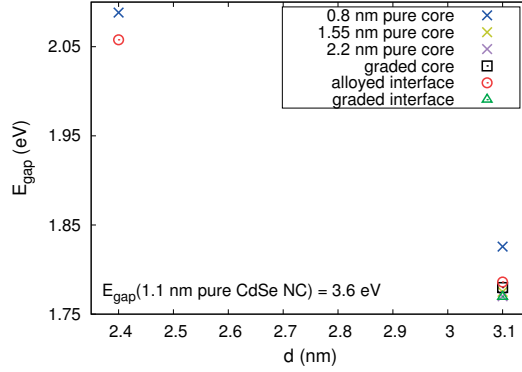


Figure 5.6. Band gaps of CdSe/CdS core-shell NCs with different size, made using different structural models and core sizes.

The increased localisation of the HOMO and LUMO WFs in the core of the CdSe/CdS NCs, decreases the probability of non-radiative recombinations and photo-oxidation of the hole at the surface, increasing the QE. Hence, we calculated the confinement of the HOMO and LUMO WF, $\psi(\mathbf{r})$, as:

$$I_{|\text{WF}|^2} = \int_0^{r_0} |\psi(\mathbf{r})|^2 d\mathbf{r} \quad (5.6)$$

using four different values for the integration radius, r_0 , 2.6 Å, 4.9 Å, 8.7 Å, and 12.1 Å. The resulting confinement of both HOMO and LUMO WFs as a function of r_0 , are shown in Fig. 5.7. Evidently, the confinement of the HOMO WF in the core of the NCs is significantly larger than the confinement of the LUMO WF, and exhibits significant dependence on the core size and the model type. With increasing core/shell ratio, the confinement of the HOMO WF decreases, suggesting that the NCs with smaller core would have higher QE. Moreover, in the NCs with different structural model and same core size, 0.8 nm, the confinement of the HOMO WF is rather similar, except in the NC with pure core, which shows slightly higher confinement. From this difference in the confinement, it is expected the the NCs with different structural model will have similar QE, with the NC with pure core having somewhat higher QE. It is also noticeable that the confinement of the HOMO WF increases with decreasing NC size, indicating that lowering the NC size would increase the QE.

In addition, the spatial distribution of the HOMO WF can influence the Auger recombination (AR) rates, causing the AR rates to decrease with increase spread of the HOMO WF [113], which in turn will increase the QE of the NCs. Therefore, the decreased confinement of the HOMO WF in the NCs with alloyed and graded interface, is likely to induce lowering of the AR rates, compared to the NC with 0.8 nm pure core. In the NCs with different size of the pure core, it is expected that the AR rates to decrease with growing core

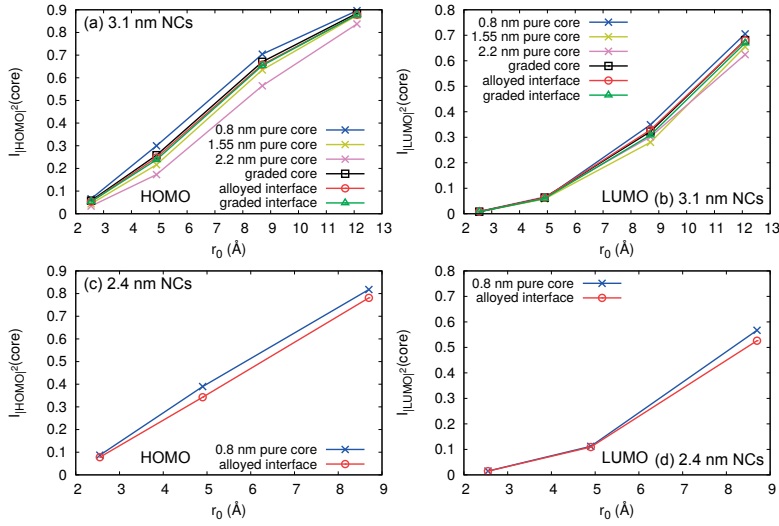


Figure 5.7. Comparison between the confinement of the HOMO and LUMO WFs respectively of: (a) and (b) 2.4 nm NCs; and (c) and (d) 3.1 nm NCs, with different structural models, as a function of the core integration radius, r_0 .

size, following the decreasing confinement of the HOMO WF. Another quantity that can give further information regarding the AR, is the electron-hole (e-h) Coulomb interaction energy (E_b). To evaluate the e-h E_b , Eq. 5.5 was used, and the calculated e-h E_b are shown in Fig. 5.8.

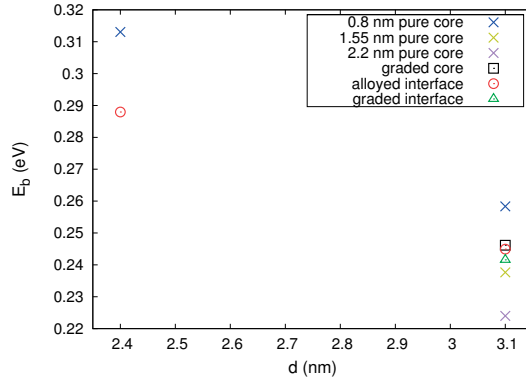


Figure 5.8. Electron-hole Coulomb interaction energies, E_b , of CdSe/CdS core-shell NCs with different size, made using different structural models and core size.

It is evident that the e-h E_b are reduced with increasing core size, in the NC with same size. Considering that the AR rates decrease with increased e-h E_b [113], and the lower AR rates contribute to increase QE, the lowering of the e-h E_b with increasing core size indicates that the NCs with largest core would have higher QE. In the NCs with different structural models, the e-h E_b are

very similar, with the NC with 0.8 nm pure core exhibiting higher e-h E_b . This suggests that introducing alloyed or graded interface between the core and the shell lowers the e-h E_b , and hence can decrease the AR rates, increasing the QE of the CdSe/CdS NCs.

5.3 CdS/ZnS core-shell NCs

Another interesting example where making core-shell NCs can greatly improve the properties, are the CdS/ZnS core-shell NCs. The overcoating of the CdS NCs with ZnS shell suppresses the deep-trap white luminescence otherwise exhibited by the bare CdS NCs, suppressing the non-radiative transitions. The CdS/ZnS NCs produced in this way are very suitable for light-emitting devices, especially because of their high intensity blue light. However, unlike the CdSe/CdS NCs which have been extensively studied experimentally and theoretically, until now for the CdS/ZnS NCs there have not been any reported studies of the dependence of the PL properties on the structural model nor theoretical studies of the size-dependence of the PL properties. Therefore, we focused the study on the understanding how the size of the NCs and the different structural models can influence the PL properties. Similarly to the CdSe/CdS NCs, we investigated the band gaps, the spatial distribution of HOMO and LUMO WFs and the electron-hole Coulomb interaction energies.

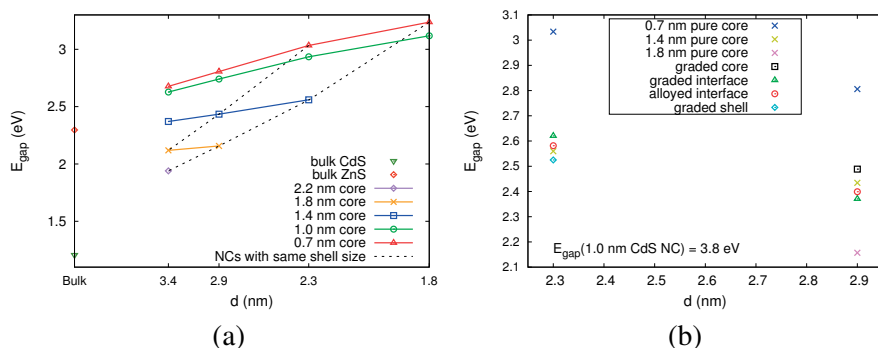


Figure 5.9. Band gaps of CdS/ZnS core-shell NCs as a function of: (a) as a function of the NC size; and (b) different structural model. The dashed line in (a) connects the gaps of NCs with same shell size.

To study the size dependence of the PL properties, NCs with four different sizes were made, and we inserted cores with five different size, depending on the size of the NCs. Moreover, from the 2.3 and 2.9 nm NCs we constructed NCs with the same structural models as in the CdSe/CdS NCs. The surface of each of the studied NCs is completely passivated with pseudohydrogen. The calculations were performed in the same manner as described in the previous section, Sec. 5.2. When comparing the DOS and the absorption indices of

the NCs with different size, and same core size, rather small differences were observed. Also, we observed rather weak dependence of the DOS and the absorption indices on the core/shell ratio and the different structural model.

However, the changes in the band gap with changes in the NC size and core/shell ratio are significantly larger (see Fig. 5.9(a)), which comes mainly from the large difference in the band gap of the bulk CdS and ZnS. Following the quantum confinement effect, the band gaps are increasing with decreasing NC size, as well as with decreasing core size. Moreover, the dependence on the core size is less pronounced than the dependence on the shell size, which can be attributed to the notable increase in the shell material, ZnS, when the shell size is growing, compared to the increase in the core material, CdS. In the NCs with different structural models, the band gaps are very similar, except when the NCs have very small or very large core, where considerable increase or reduction of the band gap are respectively evident (see Fig. 5.9(b)).

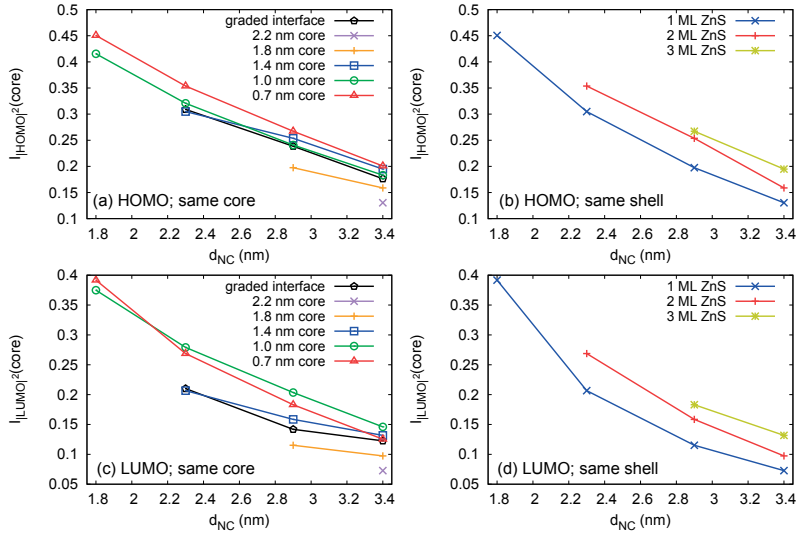


Figure 5.10. Comparison between the confinement of the HOMO and LUMO WFs in NCs with: (a) and (c) same core size, respectively; (b) and (d) same shell size, respectively; as a function of the NCs size. The confinement is calculated using the same core integration radius, $r_0 = 4.7 \text{ \AA}$ (corresponding to the smallest pure core).

As in the CdSe/CdS core-shell NCs, in the CdS/ZnS NCs both the electron and the hole are confined in the core of the NCs. This type of band alignment is exhibited throughout the whole series of studied NCs. Having both electron and hole confined in the core of the NC, lowers the probability of non-radiative transitions at surface traps, increasing the QE of the NCs. Therefore, to understand how much the HOMO and LUMO WFs are localised in the core of the NC, we calculated confinement of the WFs using Eq. 5.6, using $r_0 = 4.7 \text{ \AA}$, and plotted them as a function of the size of the NCs (see Fig. 5.10). Clearly, the confinement of both the HOMO and LUMO WFs decreases with increas-

ing NC size, when NCs with same core size are compared. In the NCs with the same size, but different core size, the confinement of both WFs is reduced with increasing core size. This notable confinement of the HOMO and LUMO WFs in the NCs with small core is expected to increase the QE of these NCs, compared to the NCs with larger cores.

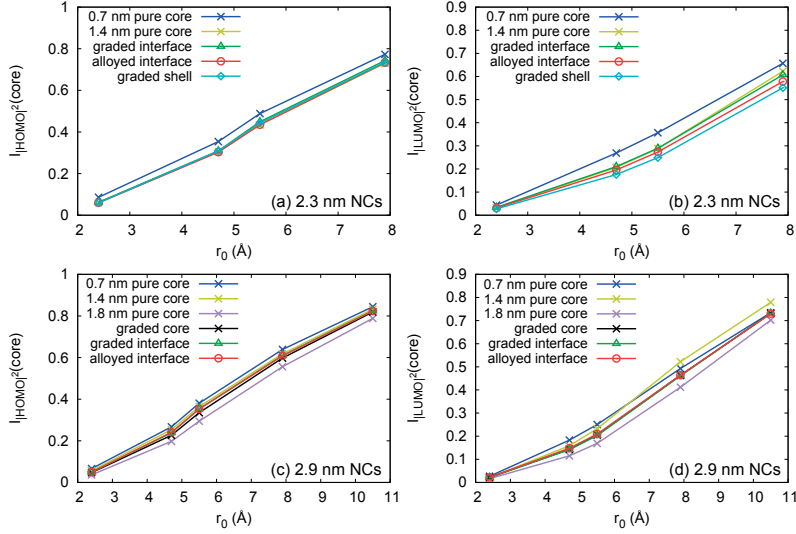


Figure 5.11. Comparison between the confinement of the HOMO and LUMO WFs respectively of: (a) and (b) 2.3 nm NCs; and (c) and (d) 2.9 nm NCs, with different structural models, as a function of the core integration radius, r_0 .

In the NCs with different structural models, as shown in Fig. 5.11, the confinement of the HOMO and LUMO WFs slightly decreases with introducing alloyed or graded interface, when comparing with the NCs with same pure core size, 0.7 nm. However, having a graded core of the same size as a pure core, increases the confinement of both WFs, which can increase the QE of the NCs. Moreover, as discussed in the previous section (Sec. 5.2), the lowered confinement of the HOMO WF can decrease the AR rates, consequently increasing the QE of the NCs. Thus, it is likely that introducing alloyed or graded interface will lower the AR rates, in NCs with same core size.

Further information regarding the non-local characteristic of the excitation, and the attraction between the electron and the hole can be gained from the electron-hole (e-h) Coulomb interaction energies (E_b). Therefore, we calculated the e-h E_b , using the Eq. 5.5, and the resulting e-h E_b for NCs with different size and structural models are shown in Fig. 5.12. Evidently, with growing NC size and core size, the e-h E_b are decreasing. Furthermore, the presence of alloyed or graded interface can lower the e-h E_b , and having in mind that the AR rate depend on the square of the e-h E_b , it is expected to also lower the AR rates. Interestingly, capping the CdS core with alloyed or graded shell can notably decrease the e-h E_b , which can be expected further decrease

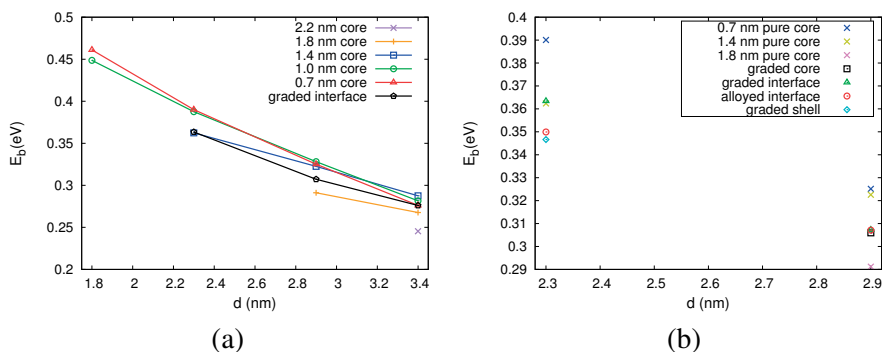


Figure 5.12. Electron-hole Coulomb interaction energies (E_b) of CdS/ZnS core-shell NCs as a function of: (a) as a function of the NC size; and (b) different structural model.

the AR rate and increase the QE, but the defects that appear on the surface can significantly reduce the QE by facilitating non-radiative transitions, which has been shown experimentally [101].

5.4 Comparison between CdSe/CdS and CdS/ZnS core-shell NCs

Although the CdSe/CdS and CdS/ZnS core-shell NCs are composed of very similar elements, they exhibit somewhat different PL properties. One of the reasons might be in the constituent elements in the core and the shell, specifically the CdSe/CdS NCs have common cation, and the CdS/ZnS common anion. Therefore, it is very interesting to investigate the changes in the properties of the NCs, when going from CdSe/CdS to CdS/ZnS NCs. In this section, a direct comparison between the band gaps, localisation of the HOMO and LUMO WFs, radiative lifetimes and the electron-hole Coulomb interaction energies in CdSe/CdS and CdS/ZnS NCs is going to be presented. Details regarding the considered NC sizes, structural models, and the calculations are given in the previous two sections (Sec. 5.2 and Sec. 5.3). Comparison between the properties of the CdSe/CdS and CdS/ZnS 2.4 nm and 2.3 nm NCs, respectively, both of which have 317 atoms, and the 3.1 and 2.9 nm NCs, respectively, with 633 atoms, is going to be given. For the larger NCs, 633 atoms, we are also going to compare the properties of the CdSe/CdS and CdS/ZnS NCs with three different core sizes¹: (i) 0.8 and 0.7 nm (29 atoms), (ii) 1.55 and 1.4 nm (123 atoms), and (iii) 2.2 and 1.8 nm (287 atoms), respectively.

¹The CdSe and CdS cores with similar size, have the same number of cations and anions. The difference in their size comes from the difference in the lattice parameter of the core materials, CdSe and CdS.

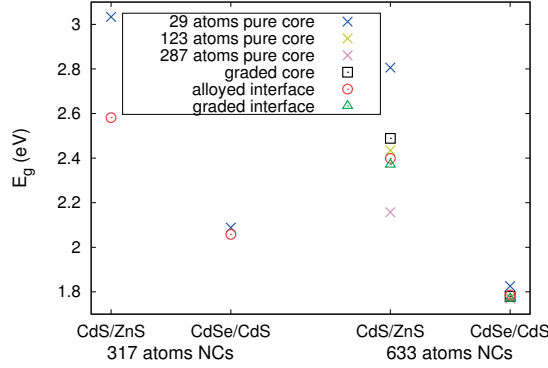


Figure 5.13. Comparison between the band gaps of CdS/ZnS and CdSe/CdS core-shell NCs, with two different sizes of NCs, 317 and 633 atoms (see the text for more details), and different structural models.

The influence of the different structural models on the DOS and the absorption indices in both types of NCs is rather weak, as discussed before. Similar behaviour can be also observed for the band gaps of both types of NCs with different structural models (see Fig. 5.13). However, there is significant difference between the change in the band gaps with changes of the structural model of the CdSe/CdS and of the CdS/ZnS NCs. The band gaps of the CdS/ZnS NCs are influenced more by the different structural models, compared to the CdSe/CdS NCs. This difference in the band gaps of both types of the NCs is a consequence of the larger difference in the band gaps of bulk CdS and ZnS, compared to the difference in CdSe and CdS bulk band gaps.

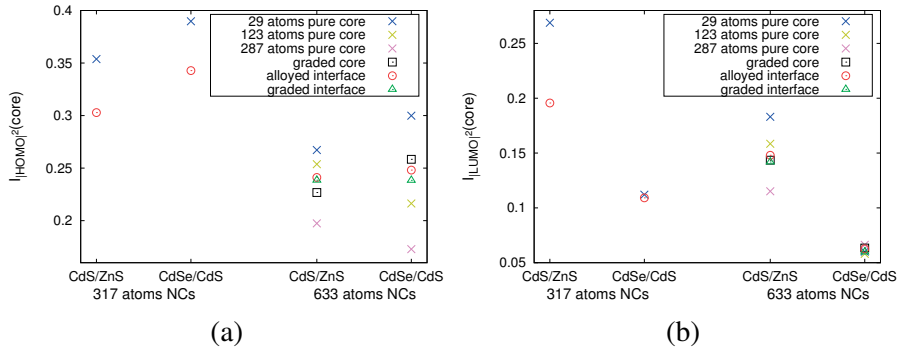


Figure 5.14. Comparison between the confinement of the: (a) HOMO WF; and (b) LUMO WF, in CdS/ZnS and CdSe/CdS core-shell NCs, with two different sizes of NCs, 317 and 633 atoms (see the text for more details), and different structural models. The confinement is calculated within the smallest pure core.

As discussed before, the QE of the core-shell NCs is influenced by the spatial distribution of the HOMO and LUMO WFs. Thus, acquiring information

regarding the spread of both WFs in the CdSe/CdS and CdS/ZnS NCs, can give valuable information for the understanding of the different PL properties of the two types of core-shell NCs. Shown in Fig. 5.14 are the calculated confinement of the HOMO and LUMO WFs of the CdSe/CdS and CdS/ZnS NCs, using Eq. 5.6, with integration radius, r_0 , that corresponds to the distance from the center to the farthest most atom in the smallest core. It is noticeable that in both types of core-shell NCs the confinement of the HOMO WF is fairly similar, and the dependence on the different structural models is also rather comparable. Based on this observation, and keeping in mind the correlation between the confinement of the HOMO WF and the AR rates, it is expected the CdSe/CdS and CdS/ZnS NCs to have similar QE. On the other hand, the extent of the confinement of the LUMO WF is very different in the CdSe/CdS and CdS/ZnS NCs. It is evident that the confinement in the CdSe/CdS NCs is significantly smaller than the confinement in the CdS/ZnS NCs, indicating increased spread of the LUMO WF in the CdSe/CdS NCs.

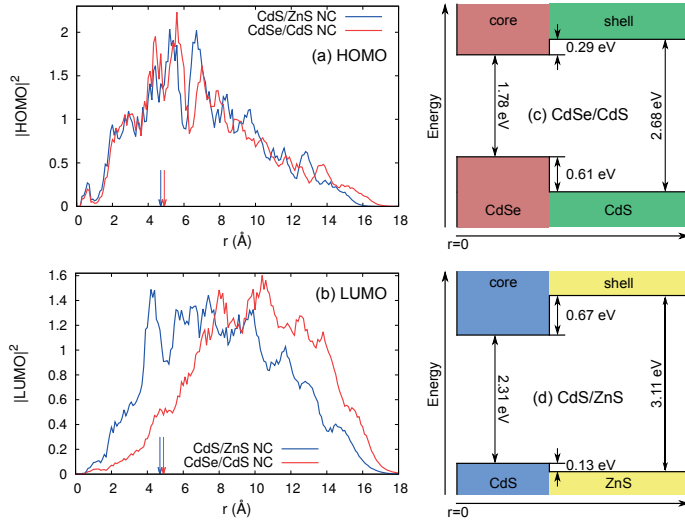


Figure 5.15. (a) Radial distribution of the density of: (a) HOMO WF (b) LUMO WF. The red and blue arrows represent the distance from the NC center to the farthest atom of the core in CdSe/CdS and CdS/ZnS NCs, respectively. Schematic representation of the band alignment in: (c) CdSe/CdS NCs; and (d) CdS/ZnS NCs. The offsets are calculated from the separate PDOS of the CdS (CdSe) core and the ZnS (CdS) shell, considering the energy at which the PDOS around the gap are higher than 0.002 states per eV per orbital.

The difference in spatial distribution of the HOMO and LUMO WFs in both types of core-shell NCs can be clearly seen from Fig. 5.15(a) and (b). To understand where does the difference in the spatial distribution of the HOMO and LUMO WFs comes from, we extracted the band alignment between the core and the shell in both types of NCs from the projected DOS (see Fig. 5.15(c)

and (d)). It is noticeable that the confinement potential of the LUMO WF in both types of core-shell NCs is very different, with the one in the CdSe/CdS NCs being fairly smaller. The lower confinement potential allows for increased spread of the LUMO WF in the CdSe/CdS NCs, compared to the CdS/ZnS NCs. In the case of the HOMO WF the situation is reversed, the confinement potential in the CdS/ZnS NCs is considerably lower than the one in the CdSe/CdS NCs. However, the HOMO WF will extend less in the shell of the NC due to the higher effective mass of the hole [114], leading to similar confinement of the HOMO WF in both types of the core-shell NCs.

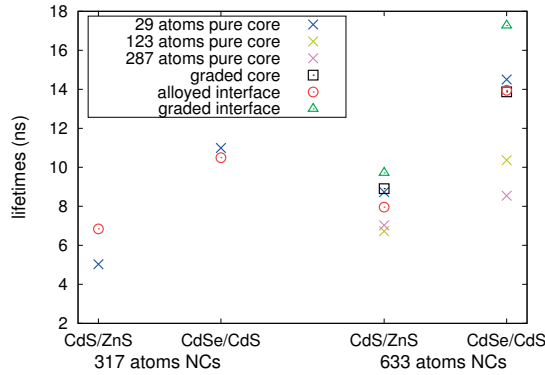


Figure 5.16. Comparison between the radiative lifetimes of CdS/ZnS and CdSe/CdS core-shell NCs, with two different sizes of NCs, 317 and 633 atoms (see the text for more details), and different structural models.

The different spread of the HOMO and LUMO WFs in CdSe/CdS and CdS/ZnS NCs will also influence the radiative lifetimes, keeping in mind that the radiative lifetimes depend inversely on the dipolar overlap integral of the HOMO and LUMO WFs [115]. Shown in Fig. 5.17 is a comparison between the calculated radiative lifetimes, using Eq. 5.4, of the CdSe/CdS and CdS/ZnS NCs. It is noticeable that the radiative lifetimes of the CdSe/CdS NCs are slightly longer compared to the ones in CdS/ZnS, which can be attributed to the decreased overlap between the HOMO and LUMO WFs in the CdSe/CdS NCs. As previously discussed, the HOMO WF in both types of NCs has similar spatial distribution, thus the spatial distribution of the LUMO WF would mainly influence on the radiative lifetimes. In the CdSe/CdS NCs, the LUMO WF is spread significantly in the shell of the NCs, decreasing the overlap with the HOMO WF, thus increasing the lifetimes, which explains the longer lifetimes in the CdSe/CdS NCs. Based on this observation, it is expected the CdS/ZnS NCs to have slightly higher QE compared to the CdSe/CdS NCs.

Moreover, the spatial distribution of the HOMO and LUMO WFs will also influence the electron-hole (e-h) Coulomb interaction energies (E_b) in the CdSe/CdS and CdS/ZnS NCs, as shown in Fig. 5.16. It is evident that the CdSe/CdS NCs have considerably smaller e-h E_b , compared to the CdS/ZnS

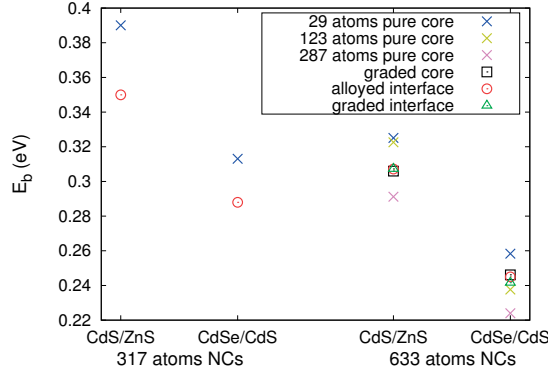


Figure 5.17. Comparison between the electron-hole Coulomb interaction energies (E_b) of CdS/ZnS and CdSe/CdS core-shell NCs, with two different sizes of NCs, 317 and 633 atoms (see the text for more details), and different structural models.

NCs, regardless of the structural model. This lowering of the e-h E_b in the CdSe/CdS NCs will also decrease the AR rates, as discussed before, which in turn will cause increase in the QE. Keeping in mind that in both types of core-shell NCs, the confinement of the HOMO WF suggests similar QE, the decrease in the e-h E_b might be one of the main reasons for the distinct PL properties of the CdSe/CdS and CdS/ZnS core-shell NCs.

5.5 Si nanocrystals capped with organic ligands

Despite the intrinsic indirect nature of the band gap in Si NCs (see Sec. 4.1), the radiative transition rate of the Si NCs capped with organic ligands are comparable with the ones of direct semiconductors. It has been suggested that these fast transitions result from increased direct band gap transitions [116, 117], strong coupling between core and surface states [106], or absorption in the NC core, with recombination at the interface [110]. To have a further understanding of the origin of the fast transitions in capped Si NCs, we studied the character of the states around the band gap with changes in the NC size and the surface capping (see Paper VI). Three different sizes of Si NCs were considered, 1.5, 1.9 and 2.5 nm. The surface of the NCs was capped with two distinct types of organic ligands: methyl ($-\text{CH}_3$) and ethylamine (see Fig. 5.18), representing a non-polar and polar capping ligands, respectively. Details of the DFT calculations are given in Section 4.1.

We show that there is a significant difference in the DOS of the CH_3 -capped and ethylamine-capped Si NC. Similarly to the experiments [107, 118], we observe a shift to lower energies of the absorption indices with increasing NC size and broader absorption indices of the ethylamine-capped NCs, compared to the CH_3 -capped NCs. Moreover, the HOMO-LUMO gap and the optical-

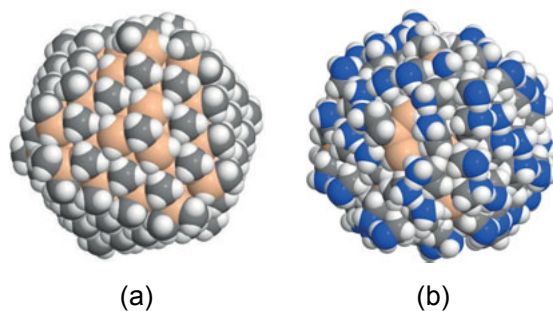


Figure 5.18. Ball models of 1.9 nm Si NCs capped with: (a) $-\text{CH}_3$; and (b) ethylamine.

absorption gap increase with decreasing NC size, regardless of the surface capping. This can be clearly seen from data in Table 5.1. It is also evident that the difference in both gap increases with increasing NC size, indicating a growing intrinsic indirect nature of the band gap in these NCs. In addition, both gaps in the ethylamine-capped NCs are considerably smaller compared to the gaps in the CH_3 -capped and the hydrogenated NCs. To see the cause of this difference in the gaps, and to understand how does the intrinsic indirect nature of the gap influences the transition rates, we examined the character of the states around the gap and the states between which the fastest transitions occur.

Table 5.1. Calculated HOMO-LUMO gaps and optical absorption gaps, in eV, of CH_3 -capped, ethylamine-capped (amine) and hydrogenated ($-\text{H}$) Si NCs, with different NC diameter (d).

particle	d (nm)	HOMO-LUMO			absorption gap		
		$-\text{H}$	CH_3	amine	$-\text{H}$	CH_3	amine
$\text{Si}_{87}\text{H}_{76}$	1.5	2.73	2.70	1.35	3.12	3.05	1.57
$\text{Si}_{175}\text{H}_{116}$	1.9	2.24	2.31	1.14	2.79	2.76	1.54
$\text{Si}_{389}\text{H}_{196}$	2.5	1.80	1.83	0.89	2.63	2.63	1.77

We first calculated the projected DOS (PDOS) (see Fig. 5.19, upper panel) of the Si atoms in the core, the Si atoms at the surface and the ligand. Also shown in Fig. 5.19 (middle panel) are the PDOS for every consecutive layer in the Si NC, going from the center (one Si atom) to the outer groups of the capping ligands. Evidently, the contribution from the CH_3 and ethylamine ligands to the states around the gap is considerably different. In the ethylamine-capped NCs the states at the top of the valence band (VB) are almost entirely dominated by ligand states, which is not the case for the CH_3 -capped NCs, where the contribution from the ligand to the states around the gap is negligible. From the layer-resolved PDOS (middle panel in Fig. 5.19) it is noticeable that the highest contribution to the states at the top of the VB comes from the outer most NH_2 group. This can also be seen from the real space distribu-

tion of the HOMO and LUMO WFs (see bottom panel in Fig. 5.19), where increased localisation of the HOMO WF around the NH_2 is noticeable. These surface states coming from the NH_2 group can trap the hole, causing broadening of the PL peak and lowering of the PL intensity, which has been observed experimentally for amine-capped Si NCs [107].

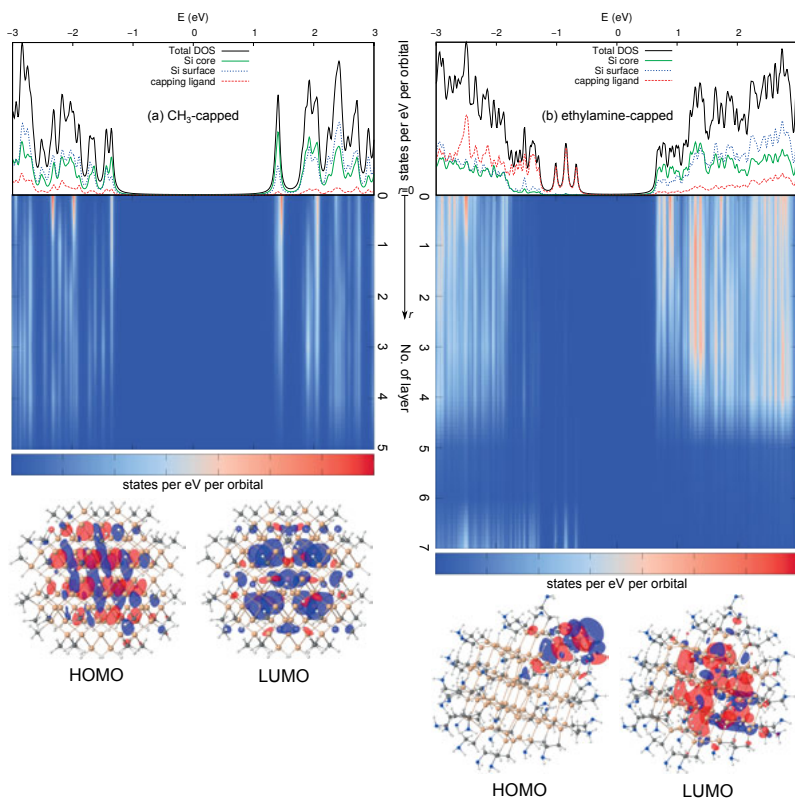


Figure 5.19. Projected DOS (PDOS) of 1.5 nm Si NCs capped with: (a) $-\text{CH}_3$; and (b) ethylamine. The top panels show the PDOS of the NC normalised by the total number of orbitals. The middle panels show the PDOS from a given layer, normalised by the number of orbitals in the layer. The bottom panels show the HOMO and LUMO WFs, where the Si, C, N and H atoms are shown in tan, grey, blue and white, respectively.

To deepen our study, and to see if we could provide more fundamental understanding of the short radiative lifetimes observed in experiments, we calculated the radiative lifetimes in each of the studied NCs, using the Eq. 5.4. The calculated radiative lifetimes are shown in Table 5.2. Although the calculated radiative lifetimes are in a good agreement with previous theoretical calculations [111], they are few orders of magnitude longer compared to the experimentally observed ones. However, it is interesting to notice that capping the surface with organic ligand suppresses the increase in the radiative lifetimes with growing NC size. In addition, the radiative lifetimes of the ethylamine-

capped NCs are shorter compared to the CH_3 -capped NCs. To understand the origin of the two observations, we looked into the changes in the symmetry of the HOMO and LUMO WFs.

Table 5.2. *Calculated radiative lifetimes, in μs , of Si NCs capped with CH_3 and ethylamine (amine), and fully hydrogenated NCs ($-\text{H}$), with different NC diameter (d).*

Particle	d (nm)	$-\text{H}$	CH_3	amine
$\text{Si}_{87}\text{H}_{76}$	1.5	115.39	57.04	29.96
$\text{Si}_{175}\text{H}_{116}$	1.9	56.53	186.02	16.06
$\text{Si}_{389}\text{H}_{196}$	2.5	32666.71	1094.35	189.02

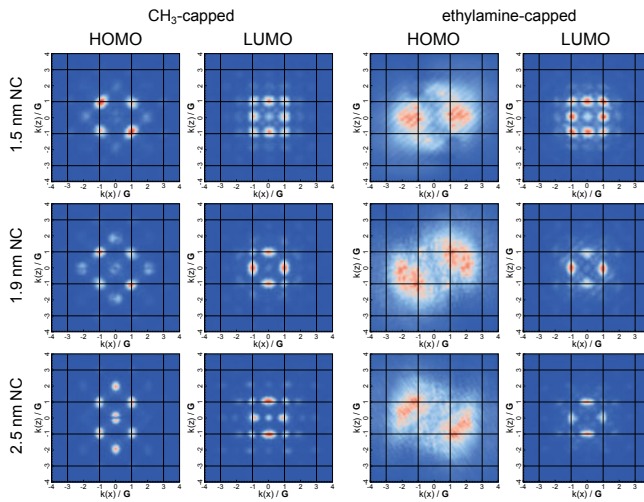


Figure 5.20. (color online) Fourier transform (FT) of the HOMO and LUMO WFs of CH_3 -capped (left column) and ethylamine-capped (right column) Si NCs, as a function of the NC size. The 3D FT was projected on the $x - z$ plane. The colour range, blue to red, maps the positive values of the real part of FT, within a fixed range (in arbitrary units). The $\mathbf{k}(x)$ and $\mathbf{k}(z)$ are scaled by the reciprocal vector \mathbf{G} of size $\frac{2\pi}{a}$.

Shown in Fig. 5.20 are the Fourier transformation (FT) of the HOMO and LUMO WF, projected on $x - z$ plane. The FT of the HOMO and LUMO WF of the CH_3 -capped NCs show similar features with the respective FT of the hydrogenated Si NCs (see Fig 4.3). Moreover, there is also similarity in the size evolution of the FT of both WF, in both types of NCs, where the mutual exclusive components of the FT are becoming more pronounced (see the discussion in Sec 4.1 for more details). This changes in the symmetry of the HOMO and LUMO WFs will increase the radiative lifetimes, by decreasing the dipolar overlap integral between these WFs [115]. Unlike the FT of the HOMO WF in the CH_3 -capped NCs, in the ethylamine-capped NCs, the FT of the HOMO WF is delocalised, and shows rather small changes with growing NC size.

The FT of the LUMO WF, on the other hand, is almost identical to the FT of the LUMO WF in the CH₃-capped NCs, and also there is similarity in their change with increasing NC size. Although the FT of the LUMO WF is changing with changes in the NC size, the relatively constant FT of the HOMO WF suggest that the dipolar integral between the HOMO and LUMO WF would stay rather unchanged. This in turn would cause the radiative lifetimes in the ethylamine-capped NCs to be very similar.

6. Modelling of nanocrystals, surfaces and bulk materials

In the previous chapters, the application of DFT in providing fundamental understanding of various experimentally observed effects was discussed. The present chapter deals with other aspects of DFT, mainly its usage in modelling of bulk materials, surfaces and nanocrystals. An overview of the: (1) modelling of the growth of graphene on Fe(110) surface (Paper VII); (2) stability and electronic properties of silicon nanocrystals with different shapes (Paper I); and (3) evolution of the local structure in $\text{Zn}_{1-x}\text{Cd}_x\text{S}$ solid solution (Paper VIII).

6.1 Ripples of graphene on Fe(110) surface

Since the discovery of graphene [119] and the demonstration that it possesses highly desirable properties [120–124], great deal of attention has turned into producing graphene in a cheaper way and as flat as possible. For large scale production, graphene is grown on metal substrates [125], where practically flat graphene can be epitaxially grown on Ni(111), Co(0001) or Cu(111). The high cost of these substrates has boosted the interested in finding other, more abundant metals to be used as substrates. One of the metals that is of great interest is iron, especially because of its high abundance. In addition, the previous attempts to grow graphene on iron has been met with difficulties due to the formation of thermodynamically more stable iron carbide Fe_3C . In the experimental study described in Paper VII, by enforcing high non-equilibrium growth conditions, a relatively flat monolayered graphene (MG) was grown on Fe(110) surface (MG/Fe(110)). To give a further support to the experimental findings, we performed spin-polarised ground-state DFT calculations.

For the purpose of the calculations, a simulation cell consisting 6 layers of Fe and a C layer on top were considered. The cell was relaxed allowing the C layer and the top most Fe layer to move, until the forces acting on each atom are lower than $0.05 \text{ eV}/\text{\AA}$, using DZP and DZ basis set for Fe and C, respectively. This yielded a corrugated MG/Fe(110), with a corrugation amplitude of $\sim 0.9 \text{ \AA}$, slightly higher than the experimentally observed amplitude, $0.6 \pm 0.2 \text{ \AA}$. The majority of C atoms are at distance lower than 2.7 \AA from the Fe, which is close enough to retain the Fe-C covalent bond, showing that graphene is chemisorb on the Fe(110) surface. Moreover, the simulated STM

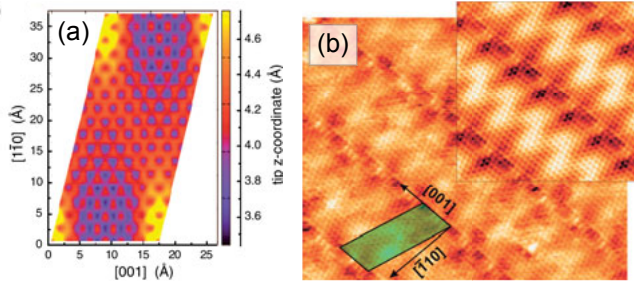


Figure 6.1. (a) Calculated vertical position of the STM tip above the MG/Fe(110) surface supercell obtained from an isosurface of the LDOS with value 10 states/(a.u.). (b) Close-up STM image. Scan size is 15 X 15 nm, $I_t = 1.2$ nA, $V_b = 0.012$ V. The surface supercell is highlighted, while inset in the top-right corner demonstrates the very same part of the image averaged over the supercell.

image of the charge densities of the states ± 0.05 eV around the Fermi level, Fig. 6.1(a), is in a good agreement with the experimentally observed STM image, Fig. 6.1(b).

6.2 Silicon nanocrystals with various shapes

The expanding variety of methods for synthesising Si NCs, provides a possibility for producing small NCs, less than 1.5 nm in size, and NCs with narrow size distribution. The shape of the Si NCs is dependent on the thermodynamic and kinetic effects, linked to the used synthesis method, while the tetrahedral coordination in the NCs is preserved. The NCs with different shapes can have diverse faces, which can interact in specific way with the environment, giving the NCs distinct properties. One way to examine the preferred shapes of the NCs is to calculate the surface and/or interface energies between the different faces [126] using DFT, and identify the combination of faces that gives the lowest surface free energy of the NCs [127].

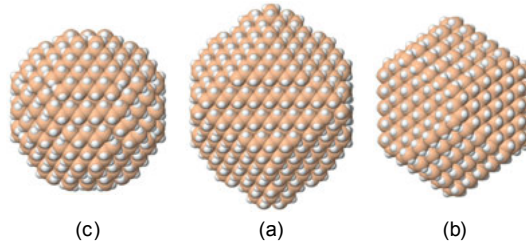


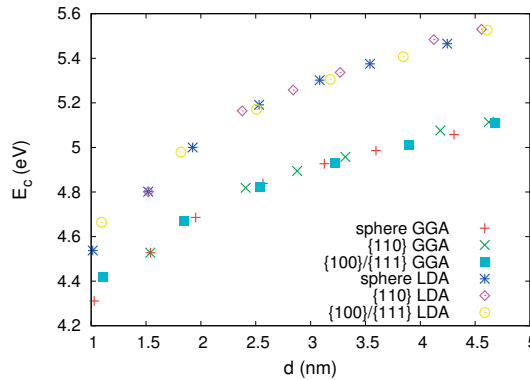
Figure 6.2. Ball models of relaxed Si NCs: (a) spherical; (b) Wulff {110}; and (c) Wulff {100}/{111} structural models.

Other approach, also based on DFT calculations, is to find the energetically most stable structure from relaxed structures with different shapes. For the

Table 6.1. Diameter (in nm), and number of silicon and hydrogen atoms in Si NCs.

Spherical structures			Wulff structures					
			{110}			{100}/{111}		
d (nm)	Si	H	d (nm)	Si	H	d (nm)	Si	H
1.0	29	36						
1.5	87	76	1.5	87	76	1.1	35	36
1.9	175	116	2.4	329	172	1.8	147	100
2.5	389	196	2.8	555	252	2.5	377	196
3.1	705	300	3.3	795	300	3.2	765	324
3.5	1087	412	4.1	1213	412	3.8	1351	484
4.2	1863	604	4.6	2320	660	4.6	2355	676

purpose of our study, we resorted to using the latter approach, which beside giving an information about the stability of the structures, it also allows investigation of the effects of the different shapes on the electronic properties. We considered three different models: spherical and two types of polyhedral Wulff structures [127], as seen from Fig. 6.2. The spherical NCs were made by cutting out a sphere from bulk Si. The NCs with Wulff structure were made by cutting along {110} or {111} and {100} planes in bulk Si, keeping the same distance between the different planes. The Si atoms with only one Si neighbour were replaced by H, and the surface was fully passivated with hydrogen. The resulting diameter, and the number of Si and H atoms in each of the structures are given in Table 6.1. Details regarding the calculations are presented in Sec. 4.1, and in Paper I.

**Figure 6.3.** Comparison between the cohesive energies of Si NCs with different shapes (spherical and Wulff-structures), calculated using LDA and GGA.

Good insight in the stability of the NCs with different shapes can be gained from comparing the cohesive energies of the NCs. Therefore, for all of the considered structures the cohesive energies per atom, E_c , were calculated us-

ing the following equation:

$$E_c = \frac{E(\text{NC}) - \sum_i E_i(\text{free}) \cdot N_i}{N}, \quad (6.1)$$

where the summation is over every atom type i , $E(\text{NC})$ is the total energy of the NC, and $E_i(\text{free})$ is the energy of a free atom of type i . The N and N_i are the total number of atoms and the number of atom of type i , respectively. The calculated E_c , using LDA and GGA, are shown in Fig. 6.3. It is evident that the E_c of the differently shaped structures, when calculated using the same exchange-correlation potential, are very similar. Moreover, they all follow a universal power law function, with an accuracy of $\sim 0.35\%$. These results for the cohesive energies, suggest that any of the structural models can be used as a model of Si NCs.

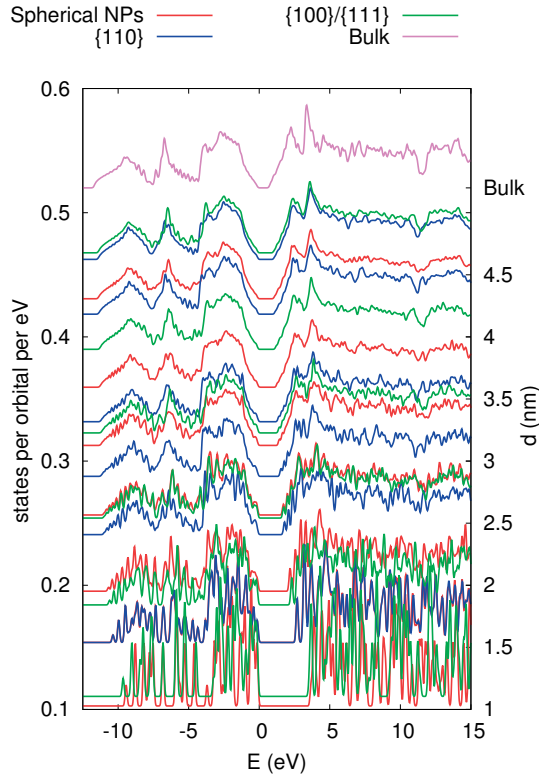


Figure 6.4. DOS of Si NCs with different shapes (spherical and Wulff structures), calculated using GGA. The DOS are shown as a function of diameter of the NC. The spherical, $\{110\}$ Wulff shapes and $\{100\}/\{111\}$ Wulff shapes are shown in blue, red, and green solid lines, respectively. The DOS of bulk silicon is shown in violet, as the top-most curve.

As mentioned before, our interest is not only in the structural characteristics of the Si NCs, but also the effects of the various shapes of the NCs on

the electronic properties, which will further support our previous assessment. Therefore, we calculated the density of states (DOS) of each of the studied structures. Shown in Fig. 6.4 are the DOS, calculated using GGA, plotted as a function of the NC diameter. For a better comparison, the DOS curves are aligned so the valence band maximum is at 0 eV. It is noticeable that the DOS of the NCs with different shapes are very similar. Also, it is evident that the HOMO-LUMO gap in each of the structures increases with decreasing NC size, which is expected from the quantum confinement effect.

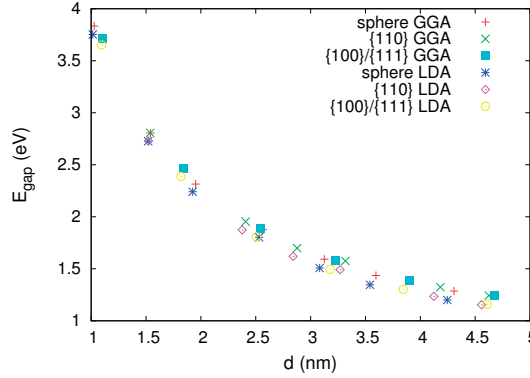


Figure 6.5. Comparison between the HOMO-LUMO gaps of Si NCs with different shapes (spherical and Wulff-structures), calculated using LDA and GGA.

To have a better overview of the different NC shapes can influence the HOMO-LUMO gaps, the HOMO-LUMO gaps we calculated as a energy difference between the highest occupied and lowest unoccupied eigenstate. The resulting HOMO-LUMO gaps are shown in Fig. 6.5. It is interesting to notice that the difference between the HOMO-LUMO gaps calculated using LDA and GGA is almost constant throughout the studied NC sizes, indicating that when it comes to electronic properties, both exchange-correlation potential perform similarly. Moreover, as in the case of the DOS, the HOMO-LUMO gaps of the spherical NCs and the Wulff-shaped NCs are very similar to each other. This observation, together with the similarity in the DOS and the correlation between the cohesive energies, shows that the spherical NCs are suitable model for Si NCs.

6.3 Evolution of the local structure in solid solutions

It has been established that there exists a linear relation between the structural parameters of an alloy and the concentrations of the constituent elements, a relation known as the Vegard's law [128]. This has been shown in many studies of diverse range of alloys using x-ray diffraction (XRD). Although the impurity doping is expected to induce competitive strain in alloys, which would

result in displacement of the constituent ions from their ideal sites, the linear variation of the lattice parameter with composition indicates a conserving of the cell volume, regardless of the distortions. The virtual-crystal approximation (VCA) [129, 130] goes further than the Vegard's law, postulating that all atoms in an alloy, e.g. $A_{1-x}B_xC$, are located on the ideal lattice sites of the average unit cell, and all A–C and B–C bond lengths have the same values. This implies that also every bond length, irrespective if it is A–C or B–C, will change linearly with the change of the lattice parameter.

Following the VCA, and considering that the atom type A is smaller than the atom type B, the increasing concentration of A, would cause decrease in the lattice parameter, hence the B–C bond length will be contracted. This will generate internally a pressure equivalent effects, termed the chemical pressure [131–133], because it originates from the chemical substitution of atoms. However, the use of these microscopic descriptions to correlate lattice parameters obtained from XRD, with changes in bond lengths, seems somewhat naive. Therefore, it is important to employ other method that can provide local structural information of the $A_{1-x}B_xC$ alloys. A method like that, also used in our study, is the extended x-ray absorption fine-structure (EXAFS) spectroscopy, which can give a direct characterization of the atom pair correlations, usable for quantitative description of the local atomic level picture.

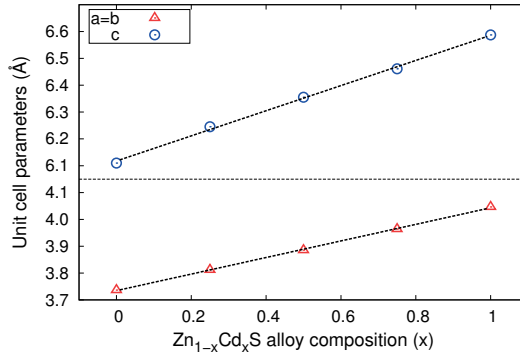


Figure 6.6. Linear variation of the lattice parameters for $Zn_{1-x}Cd_xS$ alloy as a function of the composition of Cd.

To have a better understanding of the microscopical changes, we chose the ternary alloy system $Zn_{1-x}Cd_xS$ with Wurtzite structure, for which we performed DFT study. For this purpose three different alloy compositions, with $x = 25\%$, 50% and 75% , in a supercell that contains 288 atoms were chosen. The different compositions are made by randomly substituting one cation type with the other cation type. The atom positions were relaxed using LDA and DZP basis set for the three types of atoms, until the forces acting on every atom were lower than $0.04 \text{ eV}/\text{\AA}$. During the relaxation, the volume of the cells

was allowed to change. The results from our study were later on confirmed by experiments, and the detailed analysis is given in Paper VIII.

The calculated lattice parameters are shown in Fig. 6.6, showing a notable linear variation of the lattice parameter with alloy composition. Moreover, the cell parameters are decreasing with increasing concentration of the smaller Zn^{+2} ions. This trend in the cell parameters is in agreement with the Vegard's law.

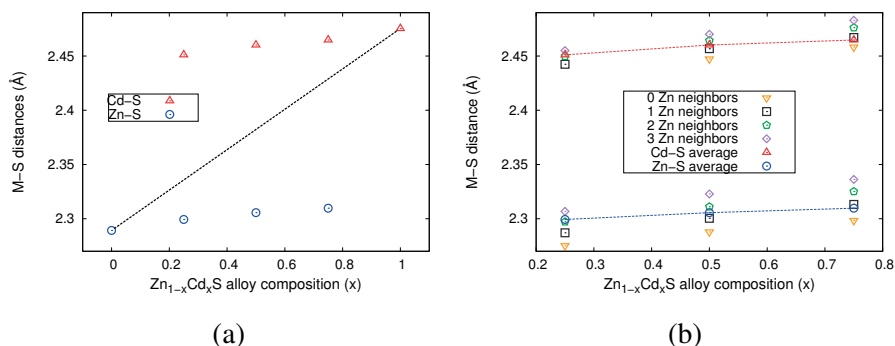


Figure 6.7. First shell bond distances for $\text{Zn}_{1-x}\text{Cd}_x\text{S}$ alloy. The Cd-S and Zn-S bond length are shown in red up-triangles and blue circles, respectively. (a) The black dashed line represents the hypothetical average M-S bond length. (b) Dependence of the M-S bond length on the number of Zn atoms in the second nearest neighbour shell.

The dependence of Cd-S and Zn-S bond distances on the alloy composition is plotted in Fig. 6.7(a). Evidently, the Cd-S and Zn-S in the first shell practically retain their bond lengths as in their pure end members of the series, and deviate considerably from the M-S bond lengths expected from the VCA and from the lattice parameter variation according to the Vegard's law. It is also interesting to notice that the Cd-S distance decreases with increasing Zn concentration, indicating that the CdS_4 tetrahedra shrinks to accommodate the addition of Zn. The ZnS_4 tetrahedra, on the other hand, tends to dilate with increasing Cd concentration, as shown by the increasing Zn-S bond lengths in Fig. 6.7(a).

Furthermore, the first nearest neighbour bond distances also depend on the nature of the cation in the second nearest neighbour shell. This can be clearly seen from Fig. 6.7(b) where the Cd-S and Zn-S bond lengths are shown as a function of the number of Zn atoms as next nearest neighbours. Both Cd-S and Zn-S bond lengths increase with increasing number of Zn atoms as next nearest neighbour, which can be assigned to the smaller ionic radius of the Zn^{+2} compared to Cd^{+2} . The increasing number of the smaller size ion, Zn^{+2} , in the second nearest neighbour shell, leaves more available space for the central atom, hence allowing the first nearest neighbour bond lengths to increase. Similar behaviour of the first nearest neighbour bond lengths are observed in

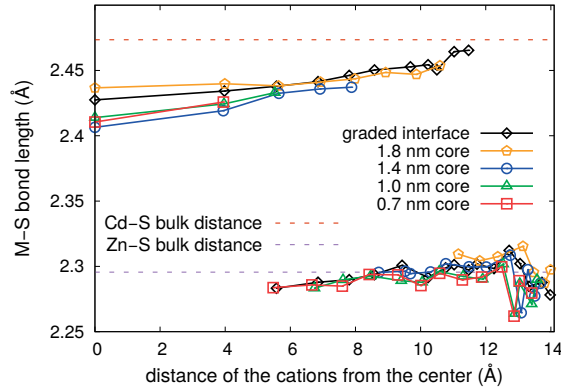


Figure 6.8. M–S bond lengths (M=Cd, Zn), in 2.9 nm CdS/ZnS core-shell NCs, as a function of distance of the cation from the center. The M–S bond lengths in NCs with core size of 0.7, 1.0, 1.4 and 1.8 nm and the ones with graded interface are shown in red, green, blue, orange and black points, respectively. The calculated bulk Cd–S and Zn–S bond lengths are respectively shown in brown and purple dashed lines.

CdS/ZnS core-shell NCs, see Fig. 6.8, where the Cd–S bond lengths increase when going towards the ZnS shell, and the Zn–S bond lengths shrink when being closer to the CdS core (see Sec. 5.3 for more details regarding the calculations).

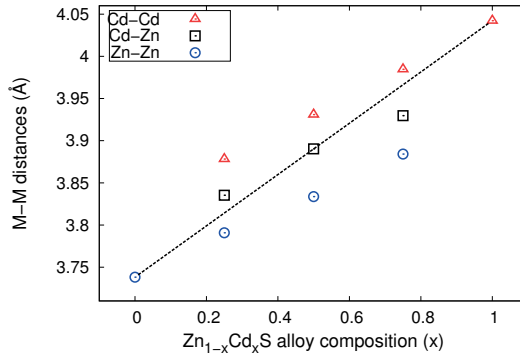


Figure 6.9. Second shell bond distances for $\text{Zn}_{1-x}\text{Cd}_x\text{S}$ alloy. The Cd–Cd, Cd–Zn and Zn–Zn bond length are shown in red up-triangles, black squares and blue circles, respectively. The black dashed line represents the hypothetical average M–M bond length.

In the second shell there is a trimodal distribution of bond distances, coming from Zn–Zn, Zn–Cd and Cd–Cd pairs, shown in Fig. 6.9. Compared to the distances in the first nearest neighbour shell, the second nearest neighbour distances more closely follow the expected distances from the VCA and the variation of the lattice parameter according to the Vegard’s law (dashed line).

However, there is still clear difference between the actual M–M distances in the second shell, and the ones expected from VCA. Having in mind that the individual nearest neighbour bond distances, M–S, were almost independent of the Cd concentration, the increased change in the second nearest neighbour bond distances can be adapted by change in the bond angles.

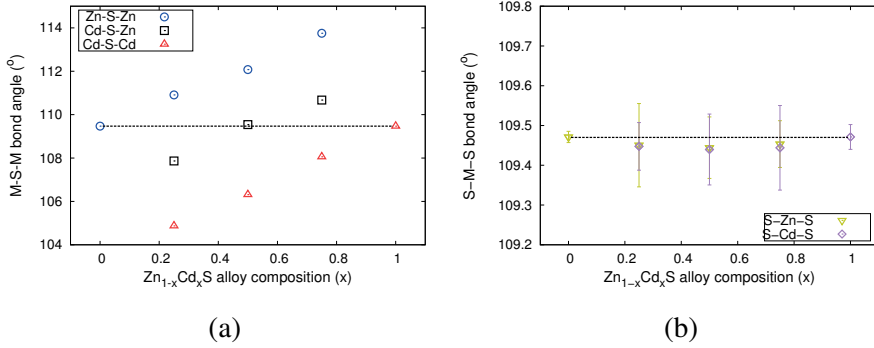


Figure 6.10. Evolution of the (a) M–S–M; and (b) S–M–S angles (M=Cd, Zn) of the second nearest neighbour shell in the $\text{Zn}_{1-x}\text{Cd}_x\text{S}$ alloy. The Zn–S–Zn, Cd–S–Zn and Cd–S–Cd angles are shown in blue circles, black squares and red up-triangles, respectively. The S–Cd–S and S–Zn–S angles are respectively shown in purple diamonds and yellow down-triangles. The dashed black line represents the ideal tetrahedral angle value of 109.47°.

Therefore, we evaluated the bond angles for the $\text{Zn}_{1-x}\text{Cd}_x\text{S}$ alloy, and the averages of the three different M–S–M angles, Zn–S–Zn, Zn–S–Cd and Cd–S–Cd, and the S–Cd–S and S–Zn–S angles are shown in Fig. 6.10. The Cd–S–Cd angles are decreasing with decreasing Cd concentration, which can be understood as a consequence of accommodating the smaller Zn ions in the lattice. The totally opposite situation happens with the Zn–S–Zn, when larger sized Cd is introduced in the lattice. On the other hand, the S–M–S bond angles are almost independent of the Cd concentration and are very close to the ideal tetrahedral angle. Keeping this in mind, and considering the rather constant Cd–S and Zn–S bond lengths (Fig. 6.7(a)), shows that the CdS_4 and ZnS_4 tetrahedra can be regarded as the fundamental building blocks of the solid solution, with their mutual rotation being responsible for the changes in the M–S–M angles. Substituting Cd in Zn rich environment causes two corner-shared adjacent ZnS_4 tetrahedra to tilt towards each other in cooperative manner, resulting in the enlargement of the Zn–S–Zn bond angle. In the opposite case, a substitution of Zn in Cd rich environment, the pair of larger CdS_4 tetrahedra would cooperatively tilt away from each other, causing a reduction in the Cd–S–Cd bond angle.

Similar to the first shell, in the third shell a bimodal distribution of Zn–S and Cd–S bond distances is expected, with two sets per each of the M–S distances: (i) short one, with degeneracy = 1, and (ii) long one, with degeneracy = 9.

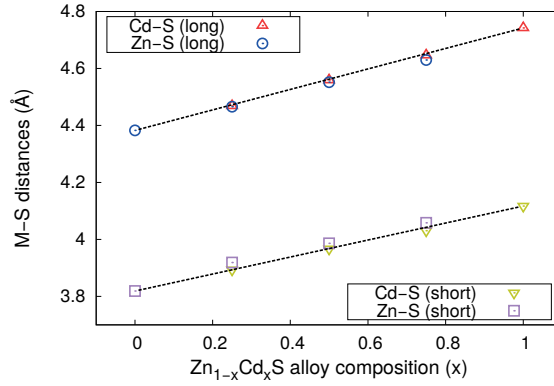


Figure 6.11. Third shell bond distances for $\text{Zn}_{1-x}\text{Cd}_x\text{S}$ alloy. The Cd-S long and short distances are shown in red up-triangles and yellow down-triangles, respectively. The Zn-S long and short distances are respectively shown in blue circles and purple squares. The black dashed lines represents the hypothetical average M-S long and short bond length.

Unlike the first shell, dilation of the lattice in the third shell is very large, and the difference between the distribution of the M-S both lengths, for the two sets, is very small, almost coinciding with the average crystal line expected from VCA, see Fig. 6.11. This shows that most probably a limiting situation is reached, beyond which the local picture would coincide with the global structural information, obtained from XRD studies.

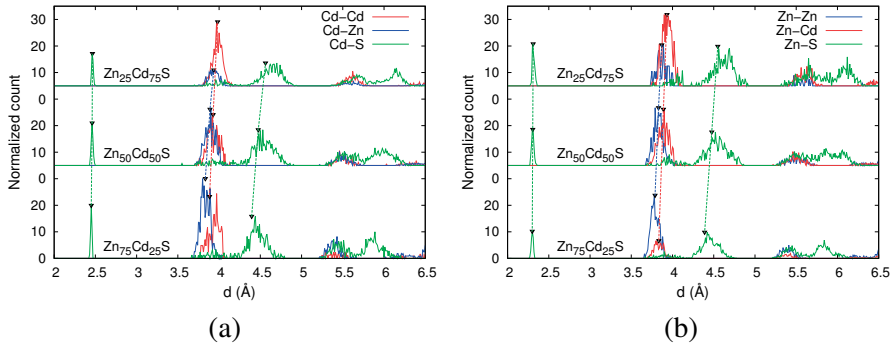


Figure 6.12. Radial distribution of the distances from (a) Cd atoms; and (b) Zn atoms, to Cd (blue), Zn (red) and S (green) atoms. The black triangles show the average distances of the 1st, 2nd and 3rd nearest neighbour distances, respectively. The first peak's intensity is lowered by factor of 10.

Complementary to our previous analyses, giving a more detailed insight, we calculated the radial distribution (RD) of distances from a Cd (or Zn) atom to Cd, Zn and S atoms, as shown in Fig. 6.12. The first peaks depict the first nearest neighbour shell. Clearly, the distribution of distances is very small, and the

dependence of the peak position on the alloy composition is very weak. Moving towards the second and the third nearest neighbour shell, the dependence on the alloy composition is becoming more pronounced. It is also evident that the Cd–S and Zn–S bond distances are becoming longer, with respective increase in the concentration of Cd and Zn atoms.

In the second nearest neighbour shell, it is noticeable that the peak intensity is changing depending on the alloy composition. In Cd rich environment, the peaks coming from M–Cd bond distances have larger intensity, compare to the M–Zn. Similarly, in Zn rich environment, the peaks coming from M–Zn distances have increased intensity. This behavior is expected, considering that as the number of given atom types is growing, the number of distances to that atom will also grow. In $\text{Zn}_{0.5}\text{Cd}_{0.5}\text{S}$ alloy the peaks from M–Cd and M–Zn have similar intensity. Therefore, the change of the peaks' intensity can be used as method for determining an alloy composition. The third nearest neighbour shell is represented by two peaks, coming from the two sets of M–S bond distances. The first peak at shorter M–S bond distances, $\sim 4 \text{ \AA}$, has a rather weaker intensity, compared to the second peak at longer M–S bond distances, $\sim 4.5 \text{ \AA}$. The ratio between these two peaks is approximately 1:9, reflecting the degeneracy in the M–S bond distances in the third nearest neighbour shell.

7. Summary and outlook

The material research is becoming a dominant part in many aspects of science and technology, providing valuable new and innovative ideas and applications. In many occasions the experimental findings are supported by density functional theory (DFT) calculations. Sometimes the DFT provides a more fundamental understanding of the various experimentally observed phenomena, and in a number of cases, manages to predict certain behaviour of a material under given conditions. The DFT is proven to be an essential tool in understanding and describing materials and physical processes. Interestingly, in variety of circumstances, even the most basic DFT approximations can give a good estimate of the experimentally observed characteristics. However, the standard exchange correlation potentials (LDA and GGA), as the ones employed in the present calculations, have many shortcoming when it comes to predicting band gaps, as well as optical and transport properties. Therefore, for more complete and accurate studies, the use of more accurate theoretical methods is crucial. Hence, naturally the next step would be to extend the studies presented in this thesis by employing methods based on many-body perturbation theory (GW, BSE) or using an exact description of the Hartree-Fock exchange.

Central part in this thesis occupies the study of silicon nanocrystals (Si NCs). Therefore, understanding the morphology of the Si NCs, before performing any calculations is crucial. Based on the comparison of the cohesive energies and the electronic properties of Si NCs with various shapes, spherical and NCs with Wulff shape, the spherical NCs were chosen as suitable model for further calculations. For the spherical Si NCs, we observed gradual merging of the HOMO-LUMO gap and the optical absorption gap with decreasing NC size, indicating a transition from indirect to direct band gap. This transition in the band gap character was correlated with the changes in the highest occupied (HOMO) and lowest unoccupied (LUMO) eigenstates wavefunctions (WFs), where gradual emergence of bulk-like \mathbf{k} selection rule with increasing NCs size is evident. This shows that there is an increased probability of direct transitions in smaller Si NCs, highlighting the importance of confining the size of Si for light-emitting applications. It was furthermore shown that the electronic and optical properties of the Si NCs are influenced significantly more by double-bonded impurities on the surface, compared to single-bonded impurities. The modification in the properties comes from the increased localisation of the HOMO and LUMO WF around the surface impurity, which localisation decreases with growing NC size. This change in the localisation causes transformation of the symmetry of the states, making the

optical transitions between the states more probable, compared to the ones in fully hydrogenated Si NCs. In this study, the effect of a single impurity on the surface was investigated, however in experiments higher number of impurities are present. Therefore, it is necessary to study the influence of multiple impurities on the surface of Si NCs on the electronic and the optical properties. This is especially important for NCs larger than 2 nm, for which the effect of the double-bonded impurities dissipates, as we have shown in our study.

Furthermore, the different capping ligands have distinct influence on the electronic and optical properties of the Si NCs, which comes from the difference in the functional group of the ligand. The difference in the ligands also reflects in the radiative lifetimes, where the radiative lifetimes of ethylamine-capped NCs depend more weakly on the NC size compared to the CH_3 -capped NCs. The similarity in the radiative lifetimes of ethylamine-capped NCs was assigned to the rather constant symmetry of the HOMO WF in the capped NCs with changes in the NC size. However, the contribution to the states around the gap from the two considered ligands, methyl and ethylamine, is different. Thus, it would be instructive to investigate the influence of ligands with various functional groups (e.g. $-\text{OH}$, $-\text{SH}$, $-\text{Cl}$, $-\text{COOH}$ etc.) on the radiative lifetimes. Considering that the spatial separation between the functional group and the active Si NC core can affect the radiative lifetimes, it is also worth studying the effect of the ligands with different lengths of the carbon chain. The Si NCs are also considered to be an important component of the new generation of solar cells, because once embedded in a host matrix, the possibility of charge separation is increased, giving rise to higher efficiency. We demonstrated that in a system composed of Si NC in a SiC host matrix, type-II band alignment is formed, allowing for spatial separation of the charge carriers, with the top of the valence band being in the NC and the bottom of the conduction band in the host matrix. The positions of the band maxima can be interchanged by introducing oxygen, which explains the lowering of the dark conductivity in Si NCs embedded in amorphous SiC upon insertion of oxygen. Moreover, a leakage of valence band states between neighbouring NCs is observed, when the NC-NC distance is less than 1.7 nm. In a continuation of this study, an amorphous SiC can be considered as a more realistic model of the SiC host matrix. In addition, other host matrices with smaller band gap compared to the widely used matrices, for example ZnO or ITO, can be examined to see if they can also provide similar charge separation, as in the studied system, giving the possibility of producing more efficient solar cells. For all of these complex systems the transport properties can be calculated, yielding a deeper insight into their applicability as photovoltaics.

Great deal of attention has also been devoted to the understanding of the influence of the size and different structural models on the electronic and optical properties of CdSe/CdS and CdS/ZnS core-shell NCs. We show a similar behaviour of the band gaps in both CdSe/CdS and CdS/ZnS core-shell NCs, with variation in the size and the structural model, where the band gaps of the

CdS/ZnS NCs are influenced more by the structural changes. In both types of core-shell NCs, the confinement of the HOMO WF in the core of the NC with same size is similar, regardless of the structural model, indicating a similar Auger rates in both types of NCs, hence similar quantum efficiency (QE). However, the LUMO WF in the CdSe/CdS NCs spreads more in the shell of the NC, compared to the LUMO WF of the CdS/ZnS NC. This different spatial distribution of the HOMO and LUMO WF influences both the radiative lifetimes and the electron-hole Coulomb interaction energies (e-h E_b). The relative difference in the radiative lifetimes in both types of NCs is significantly smaller compared to the relative difference in the e-h E_b . Furthermore, the e-h E_b in the CdSe/CdS NCs are considerably smaller than in the CdS/ZnS. The decrease in the e-h E_b can lower the Auger rates, increasing the QE, which can be one of the reasons for the distinct photoluminescence properties of the CdSe/CdS and CdS/ZnS NCs. Keeping this in mind, to increase the QE of the CdS/ZnS NCs, the structure should be designed to allow the LUMO WF to spread more in the ZnS shell. This can be achieved by introducing alloyed interface, i.e. forming CdS/Zn_{1-x}Cd_xS/ZnS NCs, with the spatial distribution of the LUMO WF being naturally dependent on the concentration of the Cd atoms. The changes in the spread of the LUMO WF would induce changes in the properties of the CdS/Zn_{1-x}Cd_xS/ZnS NCs, which can be an interesting topic for further study.

Beside being the most useful tool in estimating and predicting the fundamental electronic structure properties, DFT can be used in modelling of various materials. We show that the ripples in graphene, grown on Fe(110) surface, can be well reproduced by DFT calculations. The experience gained from this study can be applied in modelling the growth of graphene on other surfaces, which can be further used in calculating various properties, or simulating epitaxial growth. Moreover, the local order in Zn_{1-x}Cd_xS alloys can be also well estimated, showing that the Cd-S and Zn-S bond distances in the first nearest neighbour shell of the alloy are very close to the ones in pure CdS and ZnS. This local picture changes when going towards higher neighbouring shells, with the Cd-S and Zn-S bond distances in third nearest neighbour shell becoming almost identical to the distances expected from XRD. In that study, random position of the cations were considered in the models. However, it is worth investigating if there are any preferential orientations in which the atoms in the Zn_{1-x}Cd_xS alloy would arrange, and compare this to different alloys. In addition, the study can be extended to investigating the interface between ZnS and CdS or other similar materials, along different crystallographic planes.

8. Sammanfattning

En grundläggande förståelse för processer och egenskaper hos material på en atomnivå är avgörande för att utveckla den moderna materialforskningen. Detta kan realiseras genom en kvantmekanisk beskrivning av växelverkan mellan atomer och elektroner i materialen. Den huvudsakliga vägen till energier och krafter mellan atomer samt en beskrivning av bindningen mellan dem är att lösa den grundläggande kvantmekaniska ekvationen, Schrödingerekvationen. För ett flerelektronsystem är en analytisk lösning av Schrödingerekvationen dock otillgänglig, varför ett flertal numeriska tillvägagångssätt för att noggrant och effektivt lösa ekvationen utvecklats. Ett genombrott i detta arbete var utvecklingen av en teori som erhåller flerelektronsystemets grundtillstånd via elektrontätheten, nämligen täthetsfunktionalteori (DFT). Inom DFT behandlas de mer svårtillgängliga delarna av elektron-elektronväxelverkan inom en effektiv utbytesväxelverkan-korrelationsfunktional, vilket ger en noggrann lösning till Schrödingerekvationen om dess exakta form är känd. Tyvärr är den exakta utbytesväxelverkan-korrelationsfunktionalen ej känd och approximationer måste tillämpas. Trots dessa approximationer har DFT varit framgångsrikt i att beskriva många material. Denna avhandling fokuserar på aspekter av tillämpbarhet hos DFT i att beskriva diverse materialegenskaper samt modellering av olika material. Innan en översikt av erhållna resultat presenteras ges en kort introduktion av betydelsen hos de studerade systemen.

Områdena nanovetenskap och nanoteknologi har blivit ledande inom design av nya och innovativa material vilka kan användas inom en bredd av tekniska användningsområden. De enklare och billigare metoderna att producera nanokristaller som kan avge högintensivt ljus i ett smalt spektralomfång har resulterat i växande användning av nanokristaller i fotovoltaiska samt optoelektroniska tillämpningsområden. Nanokristaller kan numera hittas i LEDs, lasrar, solceller, enfotonkällor och även i biomedicinska tillämpningar för avbildning och märkning. De utmärka ljusavgivningsegenskaperna hos nanokristaller är ett resultat av Kvantbundenhet vilket uppstår på grund av materialets storlek. När nanokristaller bildas blir excitonerna (elektron-hålparen vilka leder till ljusemissionen) instängda vilket leder till högre rekombinationshastigheter och ökad fotoluminescensintensitet. Minskad storlek hos nanokristaller leder också till högre energi hos emitterat ljus vilket tillåter fotoluminescensegenskaperna att ändras enligt specifika krav genom att ändra nanokristaller storlek.

Den exceptionella fotoluminescensen hos nanokristaller kan ändras avsevärt beroende på omgivning och i synnerhet nanokristallernas ytmaterial. Ytorenheter kan introducera medelgapstillstånd vilka stänger in elektroner eller hål och underlättar andra ickeradiativa rekombinationsprocesser. Dessa processer minskar fotoluminescensintensiteten och i leder i vissa fall till ett skift i energin hos det avgivna ljuset. För att undvika den bristen kapslas nanokristallernas yta så att full passivitet hos ensamt electronpar försäkras. Detta kan uppnås genom att täcka nanokristallerna med andra halvledare vilket leder till så kallade kärna-skal nanokristaller¹. Denna typ av ytpassivation är i synnerhet viktig för II-IV halvledare där excitoner också kan stängas in i nanokristallernas kärna och på så sätt minska yteffekter. I andra typer av halvledarnanokristaller av t.ex. Si kan ytan passiveras med organiska molekyler vilka dämpar oxideringen på ytan och ökar fotoluminescensintensiteten. Utöver ljusemissionstillämpningar så kan kvanteffekter relaterade till nanokristallernas storlek användas i solcellssyfte. I det fallet måste nanokristallerna inneslutas i en värdmatris vilken agerar som laddningsbärare. I denna typ av komplext system ökar ljusomvandlingseffektiviteten med spatial separation och ökad mobilitet hos laddningsbärarna. För produktion av effektiva solceller måste kraven på dessa egenskaper därför uppfyllas.

Med allt detta i åtanke avser vi att studera elektroniska samt optiska egenskaper hos kärna-skal och Si-nanokristaller genom användning av DFT. Vi betraktar CdSe/CdS och CdS/ZnS kärna-skal nanokristaller med olika storlek samt olika strukturmodeller, som väntat från kvantbundenhetseffekter observeras en breddning av bandgapet med minskad storlek hos nanokristallerna. Olika strukturmodeller finnes dock endast leda till små skillnader i bandgap såväl som tillståndstäthet och absorptionsindex. I en fördjupning av våra insikter inser vi att strålningstiderna och interaktionsenergierna mellan elektroner och hål påvisar något större skillnader för olika strukturmodeller. Detta stämmer väl med experimentella resultat vilka visar att legerade eller graderade gränsskikt kan minska Augertakten och att CdSe/CdS nanokristaller bör ha högre kvanteffektivitet.

Vidare fokuserade vi på förståelse för fotoluminescensen hos hydrogenerade Si-nanokristaller genom att studera storleksutvecklingen hos HOMO-LUMO och det optiska absorptionsgapet. Vi observerar sammanfogning av gapen i de minsta studerade nanokristallerna vilket indikerar en möjlig ökning av antalet direkta övergångar med minskande storlek hos nanokristallerna. Detta förklarades i mer detalj genom studier av \mathbf{k} rymdsprojektioner av HOMO och LUMO-vågfunktionerna. Studien av Si-nanokristaller utökades genom en undersökning av inflytandet hos enstaka orenheter på ytan av de hydrogenerade Si-nanokristallerna på deras elektroniska och optiska egenskaper. Vi visar att dubbelbundna orenheter inducerar avsevärt större ändringar i dessa egenskaper jämfört med enkelbundna orenheter för nanokristaller upp till 2.5 nm.

¹The translation into English would be core-shell nanocrystals.

Dessa skillnader mellan enkel och dubbelbundna orenheter påvisades också i karaktären hos tillstånden runt gapet och hos HOMO och LUMO-vågfunktionerna. Utöver detta kapslade vi också Si-nanokristallernas ytor med två olika typer av organiska liggandes i syfte att studera deras fotoluminescensegenskaper. Vi visar att ökad storlek hos nanokristallerna leder till mindre bandgap och lägre övergångstakt. Vidare visar vi att hål kan fångas in vid NH_2 -gruppen hos aminliganden, vilket förklarar den lägre fotoluminescensintensiteten i aminkapslade Si-nanokristaller. Slutligen har vi studerat inflytandet hos gränsskikt på banduppriktningen i Si-nanokristaller inbäddade i SiC och beroendet hos vågfunktionens läckage på avstånd mellan närliggande Si-nanokristaller diskuteras. När avståndet mellan närliggande nanokristaller är mindre än 1.7 nm observeras läckage av laddningstäthet mellan närliggande Si-nanokristaller. Dessutom visar vi att tillsatt syre vid gränsskiktet mellan Si-nanokristaller och SiC-matrisen orsakar att bandkanten vänder sin position i systemet. Vi relaterar detta utbyte i banduppriktningen med experimentellt lägre observerad mörk ledningsförmåga när syre introduceras i ett system av Si-nanokristaller samt SiC.

En annan del av avhandlingen behandlar förmågan hos DFT att modellera olika material. Sedan upptäckten av grafen och efter att det påvisats att materialet uppvisar högst önskvärda egenskaper, har stor ansträngning riktats åt att producera plan grafen till lägre pris. Sen det visades att plan grafen Kan tillverkas på en yta Fe(110) har vårt mål varit att stödja denna experimentella upptäckt genom modellering av tillväxt av grafen på Fe(110) med fokus på krusningar hos grafenet. Vi visar att grafen kemisorberas på Fe(110) och vi reproducerar den experimentellt observerade krusningsamplituden. Förmågan hos DFT att pålitligt modellera strukturella egenskaper hos bulkmaterial påvisades också hos $\text{Zn}_{1-x}\text{Cd}_x\text{S}$ -legeringar. Konceptet kemiskt tryck och den så kallade virtuella kristallapproximationen, båda härledda från makroskopiska observationer, utforskades för $\text{Zn}_{1-x}\text{Cd}_x\text{S}$ -legeringar med hjälp av experimentella metoder för att undersöka den lokala mikroskopiska strukturen. Innan erhållande av experimentella resultat, förutsade vi avstånd mellan närmaste grannar samt bindningsvinklar baserat på DFT i $\text{Zn}_{1-x}\text{Cd}_x\text{S}$ -legeringar.

Acknowledgements

I would like to express my deepest appreciation to my main supervisor, Ján Rusz, for his excellent guidance, patience, and continuous conveyed spirit of adventure in regard to research and scholarship. His motivation, enthusiasm and immense knowledge were constantly pushing me to strive for excellence, and without his endless help this thesis would not be possible. I owe my deepest gratitude to my second supervisor, Olle Eriksson, for sharing his wisdom, the insightful comments and suggestions, the encouragement to always look for new and innovative ideas, and to continually deepen the understanding of the problem in hand.

I cannot find words to express my gratitude to my family for their boundless love and support. The encouragement and motivation that I continuously received from them is the perpetual fuel that makes me always move forward.

My most sincere thanks to my office mates, Sumanta and Soumyajyoti, for their spontaneous jokes, lovely discussions, perceptive comments and putting up with me for all this time. My gratitude is extended to Pablo, Ana, Marco, Jonathan, Sara, Iulia, Sumanta, and Naum, for the great game nights, the wonderful get-togethers, the support in any crazy idea and the willingness to have a drink in the evenings.

To my colleagues, Barbara, Beatriz, Yaroslav, Ritwik, Marcio, Ralph, Li Wen, Manuel, Pablo, Jonathan, Marco, Heike, Raghuvier, Igor, Johan, Inka, Attila, Corina, Mirek, Adam, Karel, Kostas, Anna, Rodrigo, Marco(2), Sara, Alex, Iulia, Debora, Leyla, Sumanta, Soumyajyoti, Carmine, and many others, I want to express my gratitude for all spontaneous coffee breaks, discussions during lunch, evenings out and various activities; the time spent with you was time well spent. I have also been fortunate to be part of the small, but dynamic Macedonian group. Aleksandra, Naum, Jordan, Jane, Elena, Dushko and Sanja with Jan, though the dynamics of research life has allowed us to be compact for relatively short time, every moment together was enjoyable, always reminding me of the roots, and I am thankful for that.

I am greatly indebted to my previous advisor Ljupčo Pejov for providing me with the basic knowledge in the field of DFT studies and showing me the true value of fundamental science. I am grateful to Alex for his extensive help in translating the thesis summary in Swedish. It is definitely, without any doubt worth mentioning my proof-reading buddies, Pablo, Mirek, Iulia, Soumyajyoti and Jordan to whom I am truly thankful for their help in improving this thesis.

Special thanks to my traveling companions, Biljana, Sumanta and Soumyajyoti for joining me in various adventures, letting me organise the trips and

silently endure the bustling schedules. I also should not forget to thank my flatmate/landlord Thomas for giving a wonderful place to live and who was peacefully struggling with the mess called Vancho for more than four years. I would like to thank my dance partner, Daniela, for the great time spent together practicing and competing, and to my dance teacher, Galina, who showed me the beauty of ballroom dances and kept my passion for dancing alive.

References

- [1] H. A. Lorentz, *The theory of electrons and its applications to the phenomena of light and radiant*, 2nd ed. (Leipzig: B.G. Teubner; New York: G.E. Stechert, 1916).
- [2] P. Zeeman, *Nature* **55**, 347 (1897).
- [3] F. Braun, *Ann. Phys. (Berlin)* **296**, 552 (1897).
- [4] J. J. Thomson, *Philos. Mag. Series 5* **44**, 293 (1897).
- [5] H. Geiger and E. Marsden, *Proc. Math. Phys. Eng. Sci.* **82**, 495 (1909).
- [6] N. Bohr, *Philos. Mag. Series 6* **26**, 1 (1913).
- [7] N. Bohr, *Philos. Mag. Series 6* **26**, 476 (1913).
- [8] N. Bohr, *Philos. Mag. Series 6* **26**, 857 (1913).
- [9] M. Planck, *Ann. Phys. (Berlin)* **309**, 553 (1901).
- [10] A. Einstein, *Ann. Phys. (Berlin)* **322**, 132 (1905).
- [11] O. Stern, *Z. Phys.* **7**, 249 (1921).
- [12] W. Gerlach and O. Stern, *Z. Phys.* **8**, 110 (1922).
- [13] W. Gerlach and O. Stern, *Z. Phys.* **9**, 349 (1922).
- [14] M. Born and P. Jordan, *Z. Phys.* **34**, 858 (1925).
- [15] W. Heisenberg, *Z. Phys.* **33**, 879 (1925).
- [16] M. Born, W. Heisenberg, and P. Jordan, *Z. Phys.* **35**, 557 (1926).
- [17] E. Schrödinger, *Ann. Phys. (Berlin)* **384**, 361 (1926).
- [18] E. Schrödinger, *Ann. Phys. (Berlin)* **384**, 489 (1926).
- [19] E. Schrödinger, *Ann. Phys. (Berlin)* **385**, 437 (1926).
- [20] E. Schrödinger, *Ann. Phys. (Berlin)* **386**, 109 (1926).
- [21] J. Pauli, W., *Z. Phys.* **43**, 601 (1927).
- [22] P. A. M. Dirac, *Proc. Math. Phys. Eng. Sci.* **118**, 351 (1928).
- [23] P. A. M. Dirac, *Proc. Math. Phys. Eng. Sci.* **117**, 610 (1928).
- [24] D. R. Hartree, *Math. Proc. Cambridge* **24**, 89 (1928).
- [25] V. Fock, *Z. Phys.* **61**, 126 (1930).
- [26] J. C. Slater, *Phys. Rev.* **35**, 210 (1930).
- [27] K. A. Brueckner, *Phys. Rev.* **97**, 1353 (1955).
- [28] K. A. Brueckner, *Phys. Rev.* **100**, 36 (1955).
- [29] J. Goldstone, *Proc. Math. Phys. Eng. Sci.* **239**, 267 (1957).
- [30] W. L. McMillan, *Phys. Rev.* **138**, A442 (1965).
- [31] R. C. Grimm and R. G. Storer, *J. Comput. Phys.* **7**, 134 (1971).
- [32] J. B. Anderson, *J. Chem. Phys.* **63**, 1499 (1975).
- [33] J. B. Anderson, *J. Chem. Phys.* **65**, 4121 (1976).
- [34] P. Hohenberg and W. Kohn, *Phys. Rev.* **136**, B864 (1964).
- [35] W. Kohn and L. J. Sham, *Phys. Rev.* **140**, A1133 (1965).
- [36] P. Ordejón, E. Artacho, and J. M. Soler, *Phys. Rev. B* **53**, R10441 (1996).
- [37] J. M. Soler, E. Artacho, J. D. Gale, A. García, J. Junquera, P. Ordejón, and D. Sánchez-Portal, *J. Phys. Condens. Matter* **14**, 2745 (2002).

- [38] F. Trani, G. Cantele, D. Ninno, and G. Iadonisi, *Phys. Rev. B* **72**, 075423 (2005).
- [39] M. V. Wolkin, J. Jorne, P. M. Fauchet, G. Allan, and C. Delerue, *Phys. Rev. Lett.* **82**, 197 (1999).
- [40] M. Born and R. Oppenheimer, *Ann. Phys. (Berlin)* **389**, 457 (1927).
- [41] L. H. Thomas, *Math. Proc. Cambridge* **23**, 542 (1927).
- [42] E. Fermi, *Math. Proc. Cambridge* **6**, 602 (1927).
- [43] P. A. M. Dirac, *Math. Proc. Cambridge* **26**, 376 (1930).
- [44] D. M. Ceperley and B. J. Alder, *Phys. Rev. Lett.* **45**, 566 (1980).
- [45] J. P. Perdew, J. A. Chevary, S. H. Vosko, K. A. Jackson, M. R. Pederson, D. J. Singh, and C. Fiolhais, *Phys. Rev. B* **46**, 6671 (1992).
- [46] J. P. Perdew and W. Yue, *Phys. Rev. B* **33**, 8800 (1986).
- [47] F. Bloch, *Z. Phys.* **52**, 555 (1929).
- [48] D. R. Hamann, M. Schlüter, and C. Chiang, *Phys. Rev. Lett.* **43**, 1494 (1979).
- [49] N. Troullier and J. L. Martins, *Phys. Rev. B* **43**, 1993 (1991).
- [50] L. Kleinman and D. M. Bylander, *Phys. Rev. Lett.* **48**, 1425 (1982).
- [51] J. C. Slater, *Phys. Rev.* **36**, 57 (1930).
- [52] S. F. Boys, *Proc. Math. Phys. Eng. Sci.* **200**, 542 (1950).
- [53] L. T. Canham, *Appl. Phys. Lett.* **57**, 1046 (1990).
- [54] R. J. Walters, G. I. Bourianoff, and H. A. Atwater, *Nat. Mater.* **4**, 143 (2005).
- [55] K. D. Hirschman, L. Tsybeskov, S. P. Duttagupta, and P. M. Fauchet, *Nature* **384**, 338 (1996).
- [56] K.-Y. Cheng, R. Anthony, U. R. Kortshagen, and R. J. Holmes, *Nano Lett.* **11**, 1952 (2011).
- [57] F. Maier-Flaig, J. Rinck, M. Stephan, T. Bocksrocker, M. Bruns, C. Kübel, A. K. Powell, G. A. Ozin, and U. Lemmer, *Nano Lett.* **13**, 475 (2013).
- [58] M. Ghulinyan, D. Navarro-Urrios, A. Pitanti, A. Lui, G. Pucker, and L. Pavesi, *Opt. Express* **16**, 13218 (2008).
- [59] J. R. Rodríguez, J. G. C. Veinot, P. Bianucci, and A. Meldrum, *Appl. Phys. Lett.* **92**, 131119 (2008).
- [60] V. Švrček, A. Slaoui, and J.-C. Muller, *Thin Solid Films* **451-452**, 384 (2004).
- [61] G. Conibeer, M. Green, R. Corkish, Y. Cho, E.-C. Cho, C.-W. Jiang, T. Fangsuwannarak, E. Pink, Y. Huang, T. Puzzer, T. Trupke, B. Richards, A. Shalav, and K. lung Lin, *Thin Solid Films* **511-512**, 654 (2006).
- [62] D. Song, E.-C. Cho, G. Conibeer, C. Flynn, Y. Huang, and M. A. Green, *Sol. Energ. Mat. Sol.* **92**, 474 (2008).
- [63] M. Govoni, I. Marri, and S. Ossicini, *Nat. Photon.* **6**, 672 (2012).
- [64] Z. F. Li and E. Ruckenstein, *Nano Lett.* **4**, 1463 (2004).
- [65] F. Erogbogbo, K.-T. Yong, I. Roy, G. Xu, P. N. Prasad, and M. T. Swihart, *ACS Nano* **2**, 873 (2008).
- [66] J.-H. Park, L. Gu, G. von Maltzahn, E. Ruoslahti, S. N. Bhatia, and M. J. Sailor, *Nat. Mater.* **8**, 331 (2009).
- [67] Y. Zhong, F. Peng, F. Bao, S. Wang, X. Ji, L. Yang, Y. Su, S.-T. Lee, and Y. He, *J. Am. Chem. Soc.* **135**, 8350 (2013).
- [68] E. Borsella, R. D'Amato, M. Falconieri, E. Trave, A. Panariti, and I. Rivolta, *J. Mater. Res.* **28**, 193 (2013).

- [69] S. Chan, Y. Li, L. J. Rothberg, B. L. Miller, and P. M. Fauchet, *Mater. Sci. Eng. C* **15**, 277 (2001).
- [70] L. Rebohle, T. Gebel, R. Yankov, T. Trautmann, W. Skorupa, J. Sun, G. Gauglitz, and R. Frank, *Opt. Matter.* **27**, 1055 (2005).
- [71] M. Brandt, H. Fuchs, M. Stutzmann, J. Weber, and M. Cardona, *Solid State Commun.* **81**, 307 (1992).
- [72] S. Schuppler, S. L. Friedman, M. A. Marcus, D. L. Adler, Y.-H. Xie, F. M. Ross, T. D. Harris, W. L. Brown, Y. J. Chabal, L. E. Brus, and P. H. Citrin, *Phys. Rev. Lett.* **72**, 2648 (1994).
- [73] J. von Behren, T. van Buuren, M. Zacharias, E. Chimowitz, and P. Fauchet, *Solid State Commun.* **105**, 317 (1998).
- [74] T. van Buuren, L. N. Dinh, L. L. Chase, W. J. Siekhaus, and L. J. Terminello, *Phys. Rev. Lett.* **80**, 3803 (1998).
- [75] A. Nozik, *Physica E* **14**, 115 (2002).
- [76] G. J. Conibeer, C.-W. Jiang, D. König, S. Shrestha, T. Walsh, and M. A. Green, *Thin Solid Films* **516**, 6968 (2008).
- [77] Y. Kurokawa, S. Yamada, S. Miyajima, A. Yamada, and M. Konagai, *Current Applied Physics* **10**, S435 (2010).
- [78] J. Barbé, L. Xie, K. Leifer, P. Faucherand, C. Morin, D. Rapisarda, E. D. Vito, K. Makasheva, B. Despax, and S. Perraud, *Thin Solid Films* **522**, 136 (2012).
- [79] S. Perraud, E. Quesnel, S. Parola, J. Barbé, V. Muffato, P. Faucherand, C. Morin, K. Jarolimek, R. A. C. M. M. Van Swaaij, M. Zeman, S. Richards, A. Kingsley, H. Doyle, K. Linehan, S. O'Brien, I. M. Povey, M. E. Pemble, L. Xie, K. Leifer, K. Makasheva, and B. Despax, *Phys. Status Solidi A* **210**, 649 (2013).
- [80] H.-C. Weissker, J. Furthmüller, and F. Bechstedt, *Phys. Rev. B* **65**, 155328 (2002).
- [81] S. Furukawa and T. Miyasato, *Phys. Rev. B* **38**, 5726 (1988).
- [82] I. Vasiliev, S. Ögüt, and J. R. Chelikowsky, *Phys. Rev. Lett.* **86**, 1813 (2001).
- [83] Y. Wang, C. Chen, Z. Wu, W. Liang, X. Wang, X. Ding, L. Chu, Z. Deng, and G. Chen, *Jinzhong Fu, Micro & Nano Lett.* **6**, 1 (2011).
- [84] C. Delerue, M. Lannoo, and G. Allan, *Phys. Rev. Lett.* **84**, 2457 (2000).
- [85] T. Takagahara and K. Takeda, *Phys. Rev. B* **46**, 15578 (1992).
- [86] V. L. Colvin, M. C. Schlamp, and A. P. Alivisatos, *Nature* **370**, 354 (1994).
- [87] S. Coe, W.-K. Woo, M. Bawendi, and V. Bulović, *Nature* **420**, 800 (2002).
- [88] N. Tessler, V. Medvedev, M. Kazes, S. Kan, and U. Banin, *Science* **295**, 1506 (2002).
- [89] Q. Sun, Y. A. Wang, L. S. Li, D. Wang, T. Zhu, J. Xu, C. Yang, and Y. Li, *Nat. Photon.* **1**, 717 (2007).
- [90] J. M. Caruge, J. E. Halpert, V. Wood, V. Bulović, and M. G. Bawendi, *Nat. Photon.* **2**, 247 (2008).
- [91] V. I. Klimov, A. A. Mikhailovsky, S. Xu, A. Malko, J. A. Hollingsworth, C. A. Leatherdale, H.-J. Eisler, and M. G. Bawendi, *Science* **290**, 314 (2000).
- [92] R. Vogel, P. Hoyer, and H. Weller, *J. Phys. Chem.* **98**, 3183 (1994).
- [93] S. A. McDonald, G. Konstantatos, S. Zhang, P. W. Cyr, E. J. D. Klem, L. Levina, and E. H. Sargent, *Nat. Mater.* **4**, 138 (2005).

- [94] M. Bruchez, M. Moronne, P. Gin, S. Weiss, and A. P. Alivisatos, *Science* **281**, 2013 (1998).
- [95] W. C. W. Chan and S. Nie, *Science* **281**, 2016 (1998).
- [96] J. van Embden, J. Jasieniak, and P. Mulvaney, *J. Am. Chem. Soc.* **131**, 14299 (2009).
- [97] D. D. Sarma, A. Nag, P. K. Santra, A. Kumar, S. Sapra, and P. Mahadevan, *J. Phys. Chem. Lett.* **1**, 2149 (2010).
- [98] Y.-S. Park, A. V. Malko, J. Vela, Y. Chen, Y. Ghosh, F. García-Santamaría, J. A. Hollingsworth, V. I. Klimov, and H. Htoon, *Phys. Rev. Lett.* **106**, 187401 (2011).
- [99] F. García-Santamaría, S. Brovelli, R. Viswanatha, J. A. Hollingsworth, H. Htoon, S. A. Crooker, and V. I. Klimov, *Nano Lett.* **11**, 687 (2011).
- [100] J. Zhao, O. Chen, D. B. Strasfeld, and M. G. Bawendi, *Nano Lett.* **12**, 4477 (2012).
- [101] W. K. Bae, L. A. Padilha, Y.-S. Park, H. McDaniel, I. Robel, J. M. Pietryga, and V. I. Klimov, *ACS Nano* **7**, 3411 (2013).
- [102] O. Chen, J. Zhao, V. P. Chauhan, J. Cui, C. Wong, D. K. Harris, H. Wei, H.-S. Han, D. Fukumura, R. K. Jain, and M. G. Bawendi, *Nat. Mater.* **12**, 445 (2013).
- [103] N. Herron, Y. Wang, and H. Eckert, *J. Am. Chem. Soc.* **112**, 1322 (1990).
- [104] J. S. Steckel, J. P. Zimmer, S. Coe-Sullivan, N. E. Stott, V. Bulović, and M. G. Bawendi, *Angew. Chem. Int. Ed.* **43**, 2154 (2004).
- [105] M. Protière and P. Reiss, *Nanoscale Res. Lett.* **1**, 62 (2006).
- [106] D. S. English, L. E. Pell, Z. Yu, P. F. Barbara, and B. A. Korgel, *Nano Lett.* **2**, 681 (2002).
- [107] J. H. Warner, A. Hoshino, K. Yamamoto, and R. D. Tilley, *Angew. Chem. Int. Ed.* **44**, 4550 (2005).
- [108] M. Rosso-Vasic, E. Spruijt, B. van Lagen, L. De Cola, and H. Zuilhof, *Small* **4**, 1835 (2008).
- [109] K. Kůsová, O. Cibulka, K. Dohnalová, I. Pelant, J. Valenta, A. Fučíková, K. Židek, J. Lang, J. English, P. Matějka, P. Štěpánek, and S. Bakardjjeva, *ACS Nano* **4**, 4495 (2010).
- [110] S. Yang, W. Li, B. Cao, H. Zeng, and W. Cai, *J. Phys. Chem. C* **115**, 21056 (2011).
- [111] C. Delerue, G. Allan, and M. Lannoo, *Phys. Rev. B* **48**, 11024 (1993).
- [112] L.-W. Wang and A. Zunger, *J. Phys. Chem. B* **102**, 6449 (1998).
- [113] G. E. Cragg and A. L. Efros, *Nano Lett.* **10**, 313 (2010).
- [114] J. W. Haus, H. S. Zhou, I. Honma, and H. Komiyama, *Phys. Rev. B* **47**, 1359 (1993).
- [115] A. L. Efros, M. Rosen, M. Kuno, M. Nirmal, D. J. Norris, and M. Bawendi, *Phys. Rev. B* **54**, 4843 (1996).
- [116] J. P. Wilcoxon, G. A. Samara, and P. N. Provencio, *Phys. Rev. B* **60**, 2704 (1999).
- [117] Z. Zhou, L. Brus, and R. Friesner, *Nano Lett.* **3**, 163 (2003).
- [118] K. Linehan and H. Doyle, *Small* **10**, 584 (2014).
- [119] K. S. Novoselov, A. K. Geim, S. V. Morozov, D. Jiang, Y. Zhang, S. V. Dubonos, I. V. Grigorieva, and A. A. Firsov, *Science* **306**, 666 (2004).

- [120] K. S. Novoselov, A. K. Geim, S. V. Morozov, D. Jiang, M. I. Katsnelson, I. V. Grigorieva, S. V. Dubonos, and A. A. Firsov, *Nature* **438**, 197 (2005).
- [121] Y. Zhang, Y.-W. Tan, H. L. Stormer, and P. Kim, *Nature* **438**, 201 (2005).
- [122] M. I. Katsnelson, *Eur. Phys. J. B* **51**, 157 (2006).
- [123] K. S. Novoselov, E. McCann, S. V. Morozov, V. I. Fal'ko, M. I. Katsnelson, U. Zeitler, D. Jiang, F. Schedin, and A. K. Geim, *Nat. Phys.* **2**, 177 (2006).
- [124] M. I. Katsnelson, K. S. Novoselov, and A. K. Geim, *Nat. Phys.* **2**, 620 (2006).
- [125] J. Wintterlin and M.-L. Bocquet, *Surf. Sci.* **603**, 1841 (2009).
- [126] K. Rapcewicz, B. Chen, B. Yakobson, and J. Bernholc, *Phys. Rev. B* **57**, 7281 (1998).
- [127] G. Wulff, *Z. Kristallogr.* **34**, 449 (1901).
- [128] L. Vegard, *Z. Phys.* **5**, 17 (1921).
- [129] L. Nordheim, *Ann. Phys. (Leipz.)* **9**, 607 (1931).
- [130] L. Nordheim, *Ann. Phys. (Leipz.)* **9**, 641 (1931).
- [131] A. A. R. Fernandes, J. Santamaria, S. L. Bud'ko, O. Nakamura, J. Guimpel, and I. K. Schuller, *Phys. Rev. B* **44**, 7601 (1991).
- [132] H. C. Nguyen and J. B. Goodenough, *Phys. Rev. B* **52**, 324 (1995).
- [133] Y. Moritomo, H. Kuwahara, Y. Tomioka, and Y. Tokura, *Phys. Rev. B* **55**, 7549 (1997).

Acta Universitatis Upsaliensis

*Digital Comprehensive Summaries of Uppsala Dissertations
from the Faculty of Science and Technology 1247*

Editor: The Dean of the Faculty of Science and Technology

A doctoral dissertation from the Faculty of Science and Technology, Uppsala University, is usually a summary of a number of papers. A few copies of the complete dissertation are kept at major Swedish research libraries, while the summary alone is distributed internationally through the series Digital Comprehensive Summaries of Uppsala Dissertations from the Faculty of Science and Technology. (Prior to January, 2005, the series was published under the title "Comprehensive Summaries of Uppsala Dissertations from the Faculty of Science and Technology".)



ACTA
UNIVERSITATIS
UPSALIENSIS
UPPSALA
2015

Distribution: publications.uu.se
urn:nbn:se:uu:diva-248513